

10-A135 988

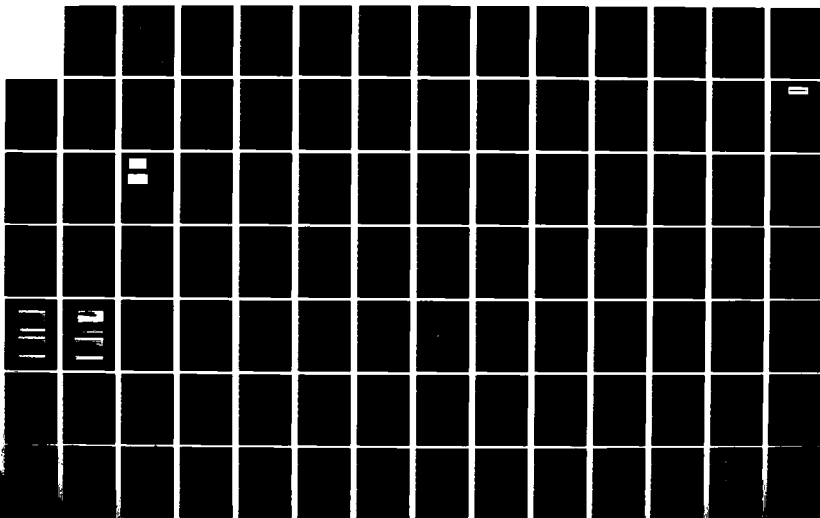
OPTICAL SIGNAL PROCESSING(U) HARRIS CORP MELBOURNE FL
GOVERNMENT SYSTEMS SECTOR A VANDERLUGT 30 NOV 83
ARO-17614.7-PH DAG29-80-C-0149

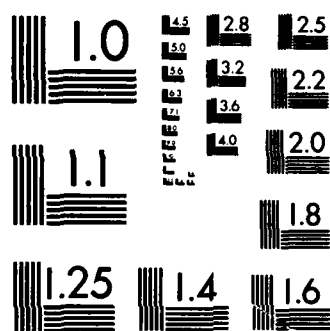
172

UNCLASSIFIED

F/G 20/6

NL





MICROCOPY RESOLUTION TEST CHART
NATIONAL BUREAU OF STANDARDS-1963-A

— . ARD 17614. 7-PH (1)

AD-A135 908

Optical Signal Processing

FINAL REPORT
17614-F

A. Vanderlugt

U.S. ARMY RESEARCH OFFICE

Contract No. DAAG29-80-C-0149

30 November 1983

APPROVED FOR PUBLIC RELEASE; DISTRIBUTION UNLIMITED

DTIC FILE COPY

DTIC
ELECTE
DEC 15 1983
S E

83 12 13 170



HARRIS

HARRIS CORPORATION GOVERNMENT SYSTEMS SECTOR
P.O. BOX 37, MELBOURNE, FLORIDA 32902, (305) 727-4000

UNCLASSIFIED

SECURITY CLASSIFICATION OF THIS PAGE (When Data Entered)

REPORT DOCUMENTATION PAGE		READ INSTRUCTIONS BEFORE COMPLETING FORM
1. REPORT NUMBER 17614-E	2. GOVT ACCESSION NO. 10-A135	3. RECIPIENT'S CATALOG NUMBER 908
4. TITLE (and Subtitle) Optical Signal Processing		5. TYPE OF REPORT & PERIOD COVERED Final Report 1 Oct. 80 - 30 Sept. 83
		6. PERFORMING ORG. REPORT NUMBER
7. AUTHOR(s) A. VanderLugt		8. CONTRACT OR GRANT NUMBER(s) DAAG29-80-C-0149
9. PERFORMING ORGANIZATION NAME AND ADDRESS Harris Corporation Government Systems Sector Melbourne, FL 32902		10. PROGRAM ELEMENT, PROJECT, TASK AREA & WORK UNIT NUMBERS
11. CONTROLLING OFFICE NAME AND ADDRESS U. S. Army Research Office Post Office Box 12211 Research Triangle Park, NC 27709		12. REPORT DATE 30 November 1983
		13. NUMBER OF PAGES
14. MONITORING AGENCY NAME & ADDRESS (if different from Controlling Office)		15. SECURITY CLASS. (of this report) Unclassified
		15a. DECLASSIFICATION/DOWNGRADING SCHEDULE
16. DISTRIBUTION STATEMENT (of this Report) Approved for public release; distribution unlimited.		
17. DISTRIBUTION STATEMENT (of the abstract entered in Block 20, if different from Report)		
18. SUPPLEMENTARY NOTES THE VIEW, OPINIONS, AND/OR FINDINGS CONTAINED IN THIS REPORT ARE THOSE OF THE AUTHOR(S) AND SHOULD NOT BE CONSTRUED AS AN OFFICIAL DEPARTMENT OF THE ARMY POSITION, POLICY, OR DE- CISION, UNLESS SO DESIGNATED BY OTHER DOCUMENTATION.		
19. KEY WORDS (Continue on reverse side if necessary and identify by block number) Optical signal processing, interferometric spectrum analyzers, Bragg cells, adaptive optical processing, transversal filtering, acoustic spreading in Bragg cells.		
20. ABSTRACT (Continue on reverse side if necessary and identify by block number) An interferometric spectrum analyzer technique, using a distributed local oscillator, doubles the dynamic range of a conventional power spectrum analyzer (i.e., 60 dB vs. 30 dB), has an instantaneous analysis bandwidth of 200-1000 MHz, and is immune to scattered noise. An analysis of Bragg cell diffraction patterns shows that acoustic spreading leads to a curvature of the diffraction pattern along an elliptical or parabolic loci. Bounds on the size of integrating photodetector along the curved direction have been established based on frequency resolution criterion. This activity was		

DD FORM 1 JAN 73 1473

EDITION OF 1 NOV 65 IS OBSOLETE

UNCLASSIFIED

SECURITY CLASSIFICATION OF THIS PAGE (When Data Entered)

UNCLASSIFIED

SECURITY CLASSIFICATION OF THIS PAGE(When Data Entered)

extended to correct the acoustic spreading by using a holographic element. For a 12-channel Bragg cell operating over an 80 MHz bandwidth, the usable aperture was increased from 10% to 100%; the number of channels increased by a factor of four. An adaptive optical processing technique has been developed to overcome the bandwidth limitations of digital systems. These Bragg cells, used in an interferometer, provide the signal to be convolved as well as the tap weights. Extensive computer simulations of the performance of the system, given the finite integration times imposed by the Bragg cells, show that notch depths of 30-40 dB can be achieved for a system having at time-bandwidth product of 2000.

UNCLASSIFIED

SECURITY CLASSIFICATION OF THIS PAGE(When Data Entered)

OPTICAL SIGNAL PROCESSING

**FINAL REPORT
17614-F**

A. VANDERLUGT

30 NOVEMBER 1983

U.S. ARMY RESEARCH OFFICE

DAAG29-80-C-0149

**HARRIS CORPORATION
GOVERNMENT SYSTEMS SECTOR
MELBOURNE, FLORIDA, 32902**

Accession For	
NTIS GRA&I	<input checked="checked" type="checkbox"/>
DTIC TAB	<input type="checkbox"/>
Unannounced	<input type="checkbox"/>
Justification	
By _____	
Distribution/ _____	
Availability Codes	
Dist	Avail and/or Special
A-1	



**APPROVED FOR PUBLIC RELEASE;
DISTRIBUTION UNLIMITED**

TABLE OF CONTENTS

	<u>Page</u>
1. INTRODUCTION	1
2. INTERFEROMETRIC SPECTRUM ANALYZERS.....	2
3. ACOUSTIC SPREADING IN BRAGG CELLS.....	3
4. ADAPTIVE OPTICAL PROCESSING.....	4
5. SCIENTIFIC PERSONNEL	7
6. REFERENCES	7

LIST OF APPENDICES

APPENDIX A: INTERFEROMETRIC SPECTRUM ANALYZER

APPENDIX B: BRAGG CELL DIFFRACTION PATTERNS

APPENDIX C: MULTICHANNEL BRAGG CELLS: CORRECTION FOR ACOUSTIC SPREADING

APPENDIX D: ADAPTIVE OPTICAL PROCESSOR

APPENDIX E: OPTICAL TRANSVERSAL PROCESSOR FOR NOTCH FILTERING

OPTICAL SIGNAL PROCESSING

1.0 INTRODUCTION

As the bandwidth of signals increase and as the electromagnetic environment becomes increasingly dense, processing operations such as convolution, spectrum analysis, correlation, ambiguity function generation and filtering become computationally intensive operations. Optical systems have the capability to perform a large number of complex multiplications and additions per unit time. As the bandwidth increases, the number of computations increase as the square of the bandwidth because the degrees of freedom of the signal is linearly proportional to bandwidth and the allowable computational time interval is a inversely proportional to bandwidth. Optical processing provides high-speed, parallel computations so that digital post-processing techniques can be used for lower-speed, serial computation.

The research effort described in this report has resulted in several innovative optical processing techniques for improved performance; it covers the three-year period from 1 October 1980 to 30 September 1983. The major accomplishments can be divided into three areas: (1) interferometric spectrum analyzers, (2) acoustic spreading in both single and multichannel Bragg cells, and (3) adaptive optical processing based on transversal filtering with feedback. In the following paragraphs, we summarize the key results in each area; further details can be found in the referenced journal articles that have been published.

2.0 INTERFEROMETRIC SPECTRUM ANALYZERS

A conventional Bragg cell power spectrum analyzer that measures the instantaneous frequency content of a wideband signal generally has a dynamic range of 25-30 dB. We developed an interferometric spectrum analyzer technique that uses a unique reference wavefront which serves as a distributed local oscillator. As a result, the photodetectors measure the instantaneous amplitude of the frequency content rather than the instantaneous power. The dynamic range is thereby doubled in dB so that, for an equivalent set of system parameters, the dynamic range is 50-60 dB.

In addition to providing a significant increase in the dynamic range, the distributed local oscillator provides a fixed offset temporal frequency at each photodetector position. The post-detection circuitry for each photodetector element is therefore identical; furthermore, both the amplitude and phase of the instantaneous spectrum can be measured if desired. Because the scattered light is not frequency shifted, the system is much less sensitive to scattered light. Another advantage of this technique is that short pulses, such as those from radar systems, can be detected even though their duration is less than the Bragg cell transit time.

Further details are provided in Reference 1 in which the results of the analytical effort was published. Since that time, Harris has completed a feasibility study and prototype development effort for AFAL. The experimental results are in excellent agreement with the theory.

3.0 ACOUSTIC SPREADING IN BRAGG CELLS

An acousto-optic device operated at high RF frequencies is often called a Bragg cell. A piezoelectric transducer is bonded to a suitable interaction medium to convert an electrical into a traveling acoustic pressure wave. This pressure wave, in turn, causes an index of refraction change that modulates the light in space and time. The acoustic wave, as it propagates away from the transducer, spreads in much the same way as does light from a small source. We analyzed the effects that this acoustic spreading has on some optical processing operations.

For a single transducer Bragg cell, the principal effect of acoustic spreading is a curvature of the Fourier spectral components. The locus of this curve is a parabola whose vertex is at the position corresponding to the RF frequency and whose focus is at the optical axis. The degree of curvature is dependent on the anisotropic nature of the interaction medium; a special case is an isotropic medium for which the parabola degenerates into a circular function.

The effects of this curvature on spectrum analysis is a function of the size of the photodetector in a direction orthogonal to that of the acoustic propagation. For a photodetector having a very large size (one which would be acceptable if the curvature were not present) the effect is to cause the peak value of the diffraction pattern to move toward the optical axis by 4% of its main lobe width, to increase the main lobe half power points by 3%,

and to increase the sidelobe levels by 5 dB on the side of the main lobe toward the optical axis. Analysis shows that these effects can be controlled by reducing the size of the photodetector with a penalty in the light collecting power of about 10%. Further details of this analysis and experimental results are given in a paper which was published in Applied Optics (Reference 2).

The acoustic spreading manifests another problem in Bragg cells having multiple transducers. The phenomena is that the spreading acoustic wave from a given transducer overlap with waves from adjacent transducers. An analysis of this phenomena showed that the optical effects of acoustic spreading can be compensated by a holographic optical element placed in a combination image/Fourier plane. At an image plane of the Bragg cell, we find that the corrected light distribution is constrained to lie within channels whose height is nearly equal to that of the transducer. We demonstrated that, for a 12-channel Bragg cell operating over an 80 MHz bandwidth, the usable aperture (defined as that region for which the channel information does not overlap) could be increased from 10% to 100%. Furthermore, the channel packing density can be increased by a factor of four. Details of this analysis and the supporting experiments will be published in the December 1983 issue of Applied Optics (Reference 3).

4.0 ADAPTIVE OPTICAL PROCESSING

The transversal filter is widely used in digital data processing. An even wider range of applications are possible when feedback loops are used; we have developed a method for implementing such operations optically. The basic concept is to consider a Bragg cell as being equivalent to a delay line which can be tapped optically instead of electrically. In this fashion, very wide bandwidth signals can be processed.

Fundamental to the notion of transversal filtering is the need to produce the appropriate tap weights. An innovative way to produce them optically is to use two orthogonally oriented Bragg cells arranged so that they are mutually imaged at a given plane. We show that if the light in this plane is integrated along one of the diagonals, the tap weights are produced. A convenient way to perform the integration is to create the two-dimensional Fourier transform of the tap weight image plane and to evaluate the transform along a line normal to the diagonal over which the integration is to be made.

The processing is completed by interferometrically adding the Fourier transform of the signal to be processed to the Fourier transform of the tap weights. This total light distribution is then square-law detected by a single element photodetector to produce an estimate of the received signal. Depending on the application, the estimate is further processed electronically and the difference between it and the received signal provides the feedback signal. Thus, the system adapts to a changing signal environment.

The chief advantage of this optical processing technique is that transversal filtering concepts can now be applied to signals having bandwidths in the 50 MHz to 500 MHz range. The system has an excellent dynamic range because it is interferometric in nature and is linear in light amplitudes. The tap weights contain both amplitude and phase information which provides for increased computational accuracy. Scattered light from the undiffracted beam does not affect the performance of the system. Details of this concept are contained in a paper published in Applied Optics (Reference 4).

The finite length of the Bragg cells impose a constraint on the number of signal components that are integrated to produce the tap weights. We

performed several computer simulations of the adaptive filtering system to characterize and determine the performance due to this limitation (digital systems can integrate signal contributions for an indefinite period). The application we chose to illustrate these effects is that of notch filtering or frequency excision. We found that we can improve the performance of the system significantly if the tap weight plane is tapered so that the readaptation phenomena is minimized as signal components leave the tap weight plane (the accumulator). In principle, the performance could be improved if the taper were extended to also weight the signal components as they enter the accumulator; this was not tested in the simulations. The taper is equivalent to using a "leaky" integrator in conventional analog systems.

The simulations show that the performance improves as the number of tap weights increase; this argues for using Bragg cells having a large time-bandwidth product. We also found that the system adapts rapidly so that notches can be quickly formed to track agile jammers. Notch depths of the order of 30-40 dB were obtained, depending on the time-bandwidth product and the number of taps used. Since the time-bandwidth product of Bragg cells are exceptionally high, a much larger number of tap weights are available as compared to digital processing systems. The results show that the finite length of the accumulators is not a serious drawback for many applications, particularly those in which the system must operate in a rapidly changing signal environment. The performance of the system then approaches that of one having an infinite accumulator and the feedback gain value needed to give equivalent tracking performance. Details of these simulations are given in a paper that has been accepted for publication by Optical Engineering (Reference 5). A paper, summarizing these results was given at the SPIE Conference on Advances in Optical Information Processing in January 1983 at Los Angeles. A short paper also appears in the conference proceedings (Reference 6).

5.0 SCIENTIFIC PERSONNEL

The principal investigator on this contract was A. VanderLugt. A.M. Bardos, Senior Scientist, and G.S. Moore, Associate Principal Engineer, assisted in some portions of the work and were partially supported by this contract.

6.0 REFERENCES

1. A. VanderLugt, "Interferometric Spectrum Analyzer," Applied Optics, Volume 20, page 2770, August 1981.
2. A. VanderLugt, "Bragg Cell Diffraction Patterns," Applied Optics, Volume 21, page 1092, March 1982.
3. A. VanderLugt, G.S. Moore and S.S. Mathe, "Multichannel Bragg Cells: Compensation for Acoustic Spreading," accepted for publication in Applied Optics; will appear in Volume 22, December 1983.
4. A. VanderLugt, "Adaptive Optical Processor," Applied Optics, Volume 21, page 4025, November 1982.
5. A. VanderLugt, "Optical Transversal Processor for Notch Filtering," accepted for publication in Optical Engineering; will appear in Volume 23, May-June 1984.
6. A. VanderLugt, "Optical Transversal Processor," SPIE Conference Proceedings, Volume 388, November 1983.

APPENDIX A

INTERFEROMETRIC SPECTRUM ANALYZER

REPRINTED FROM APPLIED OPTICS

VOLUME 20, PAGE 2770, AUGUST, 1981

Interferometric spectrum analyzer

A. Vander Lugt

Dynamic range is a key performance parameter for spectrum analyzers. The dynamic range of a Bragg cell power spectrum analyzer is generally limited by the dynamic range of self-scanned photodetector arrays. Interferometric techniques can be used to increase the dynamic range; but it is at the expense of increasing the number of photodetectors required, when the interference is introduced in the spatial domain, or a large photodetector bandwidth, when the interference is introduced in the temporal domain. In this paper we describe an interferometric approach wherein a second Bragg cell generates a spatially modulated reference waveform to produce an interference term that has a constant temporal frequency for all spatial frequencies. The advantages of this approach are lower photodetector bandwidth, improved dynamic range, improved cross talk suppression, more efficient use of the Bragg cell time-bandwidth product, immunity to scattered noise, and improved short pulse detectability. The chief disadvantage is the need for a discrete element photodetector array; when such arrays become available in hybrid or integrated packages, an additional advantage will be that of parallel postdetection processing.

1. Introduction

Optical processing techniques can be used to produce the instantaneous spectrum of wide bandwidth signals. Lambert¹ described how acoustooptic Bragg cells can be used to convert an electrical waveform $f(t)$ to an optical waveform that is a function of both space and time. If the cell is coherently illuminated, the optical system displays the Fourier transform of that segment of the waveform present within the cell. The complex valued Fourier transform can be described as

$$F_T(\omega, t) = \int_{t-T}^{t-T} f(u) \exp(-j\omega u) du, \quad (1)$$

where T is the processing time of the cell and ω is a temporal radian frequency. Generally, $F_T(\omega, t)$ is called the instantaneous spectrum of the input waveform $f(t)$; we note that it is a function of the present time t as well as a segment of its past history.

A photodetector array at the Fourier plane senses the instantaneous energy spectrum $|F_T(\omega, t)|^2$; such a system is generally called a power spectrum analyzer. A key performance parameter of any spectrum analyzer is the achievable dynamic range which is a function of the laser power, the dynamic ranges available from the Bragg cell and the photodetector array, the time-

bandwidth product, and the overall efficiency of the system. Power spectrum analyzers that use self-scanned photodetector arrays are generally limited to a 25-35-dB dynamic range due to the squaring operation on $F_T(\omega, t)$ and the inherent dynamic range limitation of the array. As the photodetector dynamic range improves, the laser power is the next important limitation to achieving a large dynamic range since Bragg cells have been developed having very large dynamic ranges.

One method for increasing the dynamic range is to use an interferometric spectrum analyzer whose output is proportional to the instantaneous magnitude spectrum $|F_T(\omega, t)|$. King *et al.*² describe heterodyning techniques for recovering both the amplitude and phase information in a light distribution. In their system the interference of an unmodulated reference beam with $F_T(\omega, t)$ produces a temporal frequency proportional to the input signal frequency ω . Since the fractional bandwidth of the input signal is usually ~50%, centered on a frequency of several hundred megahertz, the interference term occurs at a rather high frequency that varies as a function of the spatial frequency.

In this paper, I describe an interferometric spectrum analyzer in which a spatially modulated reference beam is used to reduce the temporal interference frequency to a small and fixed value over the entire spectrum. Discrete element photodetectors having a small bandwidth and a low noise equivalent power can then be used; an additional benefit of discrete detectors is that the postprocessing operations are more flexible and can be performed in parallel to reduce the output data rate.

The author is with Harris Corporation, Advanced Technology Department, Government Systems Group, P.O. Box 27, Melbourne, Florida 32901.

Received 9 February 1981.

003-6935/81/162770-10\$00.50/0.

© 1981 Optical Society of America.

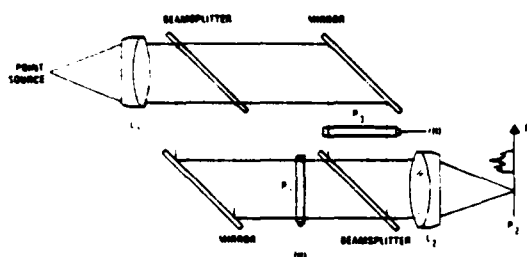


Fig. 1. Interferometric spectrum analyzer.

Self-scanned arrays cannot be used with this technique because they integrate over a time period large compared with $2\pi/\omega$, and the information contained in the interferometric output is lost. Turpin³ and Bader⁴ describe interferometric spectrum analyzers which produce a spatial fringe structure instead of a temporal fringe structure; self-scanned arrays can be used in such systems, but the number of elements must be increased to resolve the spatial fringes. Although discrete photodetectors are not the most elegant for use in systems having a large time-bandwidth product, fairly large arrays have been implemented,⁵ and advanced photodetector fabrication techniques⁶ may produce integrated devices having attractive operational features.

Some additional advantages of interferometric spectrum analysis are improved cross talk rejection, immunity to scatter noise, short pulse detectability, and uninterrupted evaluation of the spectrum. In Sec. II we describe the basic theory of the interferometric spectrum analyzer and establish the required characteristics of the reference beam. In Sec. III we determine the photodetector geometry and postdetection bandwidth required to achieve a given frequency resolution. In Sec. IV we analyze and compare the performance of candidate reference-beam waveforms. In Sec. V we compare the laser power required and the dynamic range obtained by this interferometric method with those of a power spectrum analyzer.

II. Basic Theory

Consider the interferometric system shown in Fig. 1; this system does not suggest how a practical spectrum analyzer would be configured but is used to explain the theory of operation. The two Bragg cells are illuminated by a collimated source of monochromatic light at the Bragg angle. The signal waveform $f(t)$ is applied to the transducer of the Bragg cell located in the lower leg of the interferometer at plane P_1 . Lens L_2 produces the Fourier transform of the complex light amplitude $a_1(x,t)$ leaving the cell; for a low modulation index we have a series expansion for the signal given by

$$a_1(x,t) = A_1[1 + jm_1 f(t - x/v) \cos[\omega_c(t - x/v)] + H.O.T.], \quad (2)$$

where m_1 is the modulation index, v is the velocity of the acoustic wave within the cell, and ω_c is the center frequency of the applied rf signal. The higher order terms can generally be neglected if the fractional bandwidth is $<50\%$. Further, we are usually interested in only the positive diffracted order so that the constant as well as

the negative diffracted order, which is highly suppressed by the Bragg mode of operation, can be ignored. A fraction α of the laser power P is directed into the signal beam so that the amplitude factor A_1 is equal to $(\alpha P/L)^{1/2}$, where L is the length of the cell. The effects of weighted illumination and optical losses will be considered later.

The amplitude light distribution for the first diffracted order, if we ignore a time delay $T/2$, is

$$A_1(p,t) = jm_1 A_1 \int_{-L/2}^{L/2} f(t - x/v) \exp[j\omega_c(t - x/v)] \exp(-jpx) dx. \quad (3)$$

where p is a radian spatial frequency variable related to a physical distance ξ in plane P_2 by $p = 2\pi\xi/\lambda F$, λ is the wavelength of the source, and F is the focal length of lens L_2 . Through a change of variables, we can rewrite Eq. (3) as

$$A_1(p,t) = -jm_1 A_1 \exp(-jpv) \int_{t-T/2}^{t+T/2} f(u) \exp[juv(p - p_c)] du. \quad (4)$$

The integral portion of Eq. (4) is similar to Eq. (1) except that it is centered at a position corresponding to p_c in plane P_2 , and the limits of integration are slightly different because we ignored a time delay equal to $T/2$ in the representation given by Eq. (2). The exponential phase factor shows that the light frequency is shifted linearly as a function of p . Since $pv = \omega$, the light diffracted by any continuous waveform has the same temporal frequency as the signal component.

Suppose that the input signal waveform has a cw component of frequency ω_k and amplitude C_k . The light distribution in plane P_2 can then be calculated from either Eq. (3) or (4):

$$A_1(p,t) = jm_1 A_1 L C_k \exp(-j\omega_k t) \text{sinc}[(p - p_k)L/2\pi], \quad (5)$$

which reveals that the spectrum of a sinusoidal input is a $(\sin \pi x)/\pi x$ function, centered at p_k , whose amplitude is proportional to C_k . The entire function (including the sidelobes) is multiplied by a phasor of frequency ω_k . Equation (5) further shows that the frequency resolution is $2\pi v/L$ if we use the Rayleigh criterion for resolution. We will use the function $A_1(p,t)$ as given by Eq. (5) extensively in subsequent analyses; first, however, we consider the spectrum of short pulses whose duration may be less than or equal to the processing time of the cell.

Consider the case of a pulse having a duration T_0 less than or equal to T and having a carrier frequency ω_k . Let the time of arrival be at $t = 0$; at some later time t , the leading edge of the pulse will have moved to a position $-1/2 L + vt$. Consider the output for the time interval $0 < t \leq T_0$ so that the trailing edge of the pulse has not yet entered the cell; we have that

$$A_1(p,t) = jm_1 A_1 \int_{-L/2}^{-L/2+vt} \exp[-j\omega_k(t - x/v - T/2)] \times \exp(-jpx) dx. \quad (6)$$

where we have now included the delay factor $T/2$ in the integral. After a change of variables, we find that

$$A_1(p,t) = jm_1 A_1 v t \exp(jpL/2) \exp[-j(p + p_k)vt/2] \times \text{sinc}[(p - p_k)vt/2\pi]. \quad (7)$$

This result shows that the spectrum of the pulse is centered at p_k and that as t increases, the amplitude of the sinc function increases while its width decreases. We are particularly interested in the temporal frequency behavior of this function. Note that at p_k , the centroid of the sinc function, the temporal frequency is ω_k which is the frequency of the carrier. In contrast to the case of a cw signal, however, the sidelobes of the sinc function have a frequency $(p + p_k)v/2\pi$ which varies continuously as p varies. In particular, note that at some spatial frequency $p_k + \Delta p$, the temporal frequency is $\omega_k + \Delta\omega/2$.

The last situation we consider is that of a pulse whose leading and trailing edges are both within the aperture of the Bragg cell. Let $t = 0$ be the time at which the trailing edge of the pulse has just entered the cell; then, for $0 < t < (T - T_0)$, we have

$$A_1(p,t) = jm_1 A_1 \int_{-L/2+vt}^{-L/2+vt+T_0} \exp[-j\omega_k(t - x/v - T/2)] \times \exp(-jpx) dx \\ = jm_1 A_1 v T_0 \exp[jp(L - vT_0)/2] \times \exp(jp_k v T_0/2) \exp(-jpv t) \times \text{sinc}[(p - p_k)vT_0/2\pi]. \quad (8)$$

We see that the sinc function has an amplitude and a width that are determined by vT_0 ; both are independent of time. As before, the temporal frequency at p_k is ω_k . The frequency of the sidelobes at some spatial frequency $p = p_k + \Delta p$ is equal to $\omega_k + \Delta\omega$.

We can now summarize the three cases discussed so far. In each case, the temporal frequency at the centroid of the sinc function is ω_k . At some incremental spatial frequency Δp away from the centroid, we find that the temporal frequency of the sidelobes differs from that at the centroid by zero for the case of a cw signal (or a very long pulse), by $\Delta\omega/2$ for a pulse with only its leading edge in the aperture, or by $\Delta\omega$ for a pulse with both leading and trailing edges within the aperture. The explanation for this phenomenon is that in the first case neither edge defining the pulse moves in time since it is the aperture of the Bragg cell that determines the signal length. In the second case one edge moves, but the other is stationary; in the third case, both edges move at the same velocity. The temporal frequencies in the sidelobe structure, then, contain the information about where the centroid of the pulse is located within the Bragg cell. For example, if we collect the terms in p from Eq. (8), we have a term

$$\exp[-j(p - p_k)(-L/2 + vt + vT_0/2)], \quad (9)$$

which shows that the centroid of the pulse is at $-L/2 + vt + vT_0/2$; the centroid moves at the velocity of the acoustic wave. The residual phase term in Eq. (8) is then $\exp(jp_k v T_0/2)$ which is a constant; the argument $p_k v T_0/2$ is equal to one half the number of carrier cycles contained in the pulse. A similar calculation for the case of a pulse with only the leading edge in the aperture

is obtained from Eq. (7) which shows that the centroid of the pulse, located at $-L/2 + vt/2$, is moving at one half the acoustic velocity. The number of cycles in the pulse is $p_k v t/2$ which increases as the effective pulse width increases. For a very long pulse the centroid is fixed at the optical axis and the number of cycles in the pulse is fixed at $p_k v T/2\pi = p_k L/2\pi$.

We now turn our attention to the question of generating a reference beam that will produce an interferometric fringe structure having a fixed temporal variation at all spatial frequencies. A spatially modulated reference beam will produce a fixed offset frequency because the light distribution at the Fourier plane will have a temporal and spatial frequency relationship similar to that of the signal spectrum. The reference distribution must, however, be displaced in plane P_2 relative to the signal spectrum so that the spatial displacement does not affect the temporal frequency distribution. The spatial displacement can be achieved by rotating the combining beam splitter through a small angle or by placing a prism immediately after the reference-beam Bragg cell. In either case, the reference-beam waveform at plane P_2 will be displaced to produce a fixed frequency offset over the entire spectrum as we shall now show.

We denote the bandwidth of the Bragg cell by W so that the time-bandwidth product is TW . We begin by choosing a reference-beam waveform that is a pulse of unit amplitude and length L/TW . Such a signal is equivalent to one resolution element at the plane of the Bragg cell. The Fourier transform of this narrow pulse can be obtained directly from Eq. (8) if we replace vT_0 by L/TW and replace p by $p + p_d$, where p_d represents the small displacement between the reference and signal beams at plane P_2 . The reference-beam distribution in plane P_2 then becomes

$$A_2(p,t) = \frac{jm_2 A_2 L}{TW} \exp(j\phi) \exp[-j(p + p_d)vt] \times \text{sinc}[(p + p_d - p_c)L/2\pi TW], \quad (10)$$

where ϕ is a phase term that is not a function of time and p_c is the same center frequency as that used in the signal beam Bragg cell. The envelope of the reference beam is not, of course, constant in p as we desire, but is a sinc function that is a factor of TW broader than the signal distribution. For the moment, we shall assume that the reference beam is constant over the frequency band.

The intensity at plane P_2 is given by the squared magnitude of the sum of the signal and reference-beam distributions:

$$I(p,t) = |A_1(p,t) + A_2(p,t)|^2 \quad (11)$$

$$= |A_1(p,t)|^2 + |A_2(p,t)|^2 + 2 \text{Re}[A_1(p,t)A_2^*(p,t)], \quad (12)$$

where $*$ denotes complex conjugate. Each photodetector will integrate light over an interval $p_k - \Delta p$ to $p_k + \Delta p$, where p_k denotes the center position and $2\Delta p$ the width of the photodetector. Let β be one half the ratio of the width of the photodetector to the spacing between the photodetectors so that $\Delta p = 2\pi\beta L$. The integrated intensity for the first term of Eq. (12) is calculated by using Eq. (11):

$$Q_1 = \frac{1}{2\pi} \int_{p_k - \frac{\pi d}{2}}^{p_k + \frac{\pi d}{2}} |A_1(p, t)|^2 dp = 2\beta m_1^2 A_1^2 L C_k^2, \quad (13)$$

which is valid for $\beta \leq 0.4$. The integrated intensity for the second term of Eq. (12) is obtained from Eq. (10):

$$Q_2 = \frac{1}{2\pi} \int_{p_k - \frac{\pi d}{2}}^{p_k + \frac{\pi d}{2}} |A_2(p, t)|^2 dp = 2\beta m_2^2 A_2^2 L / (TW)^2. \quad (14)$$

The contribution to the output from the third term of Eq. (12) is obtained by combining Eqs. (5) and (10):

$$Q_3(t) = \frac{1}{2\pi} \int_{p_k - \frac{\pi d}{2}}^{p_k + \frac{\pi d}{2}} 2 \operatorname{Re}[A_1(p, t) A_2^*(p, t)] dp \\ = \frac{4\beta m_1 m_2 A_1 A_2 L}{TW} C_k \cos(p_d t - \phi). \quad (15)$$

We see that the third term is proportional to the magnitude of the signal multiplied by a constant temporal offset frequency $p_d t = \omega_d$ which can be set at a convenient value. This term can, therefore, be separated from the signal and reference-beam bias terms, as given by Eqs. (13) and (14), by postdetection filtering. Since $Q_3(t)$ is not a function of p_k , the same temporal frequency offset is provided by the reference beam for any input signal. The reference beam, in this sense, is a distributed local oscillator whose temporal frequency can be changed by a simple geometric adjustment.

The total optical power collected by a photodetector is the sum of Eqs. (13), (14), and (15). When the optical power is multiplied by the photodetector sensitivity S , expressed in A/W, and we account for the optical efficiencies of the signal and reference beams (ϵ_s and ϵ_r), we find that the photodetector output current is

$$i(t) = i_1 + i_2 + i_3(t) \\ = 2\beta m_1^2 A_1^2 \epsilon_s L S C_k^2 + 2\beta m_2^2 A_2^2 \epsilon_r L S / (TW)^2 \\ + \frac{4\beta m_1 m_2 A_1 A_2 \sqrt{\epsilon_s \epsilon_r} L S}{TW} C_k \cos(\omega_d t + \phi). \quad (16)$$

Each photodetector in the Fourier plane produces a signal similar to $i(t)$ except that the value of C_k will vary depending on the strength of that frequency component in the input signal. Because the output current is proportional to C_k instead of $|C_k|^2$, as it would be for a power spectrum analyzer, the improvement in dynamic range is significant. We now consider the factors that determine the value of the parameter β associated with the photodetector geometry and postdetection bandwidth.

III. Photodetector Geometry and Bandwidth

In Fig. 2 we show the light distribution in the Fourier plane caused by two cw signals that are just resolved by the Rayleigh criterion. For sake of clarity, only the central lobe of the sinc functions as given by Eq. (5) are shown; we can also represent the signals by $\operatorname{sinc}(fT)$ which show that the signals are separated by $1/T$ Hz. The reference beam is shown as a uniform amplitude light distribution whose temporal frequency is offset by a fixed amount from that of the central frequency of the $\operatorname{sinc}(fT)$ functions. That is, if f is the temporal frequency of a cw signal, the reference-beam frequency at the centroid is $f_r = f + f_d$, where $f_d = p_d c / 2\pi$.

If we have R photodetectors per resolvable frequency, the center spacing is $1/RT$, and, if the duty cycle is $0 < d < 1$, the width of each photodetector is d/RT . Suppose that the postdetection bandwidth is a rectangular function of width b/T centered at f_d . The effect of the postdetection bandwidth is to accept light if the difference frequency between the cw signal and the reference beam falls within the bandpass and to reject it otherwise. As an example, suppose that the cw signal has a frequency of 300 MHz and that the reference-beam frequency is adjusted geometrically so that it is 310 MHz. The interference beat frequency will then be $f_d = 10$ MHz, and the narrowband postdetection filter will accept all the light near the centroid of the sinc function associated with the signal. As noted in Sec. II, the entire sinc function oscillates at a temporal frequency of 300 MHz so that, as we move the photodetector away from the 300-MHz position, we continue to collect light until the difference between the reference and signal frequency exceeds $f_d \pm b/2T$. For example, if the frequency resolution of the system is $1/T = 3$ MHz and if b is chosen to be 1, we find that when the photodetector is placed at a position corresponding to 301.5 MHz (or 298.5 MHz), the output of the narrowband filter rapidly falls to a low value.

The narrowband filter is therefore highly effective in reducing cross talk in the spectrum analyzer. The sidelobe levels decay rather slowly so that, in the absence of filtering, they contribute to an erroneous measurement of the true signal levels at nearby frequencies. Since the filter can suppress out-of-band signals by 30–40 dB in addition to the inherent roll-off of the sidelobes, it is not necessary to control the sidelobe levels by input aperture weighting.

The postdetection filtering does not, however, prevent the detection of narrow pulses. In Sec. II we showed that the spectrum of a pulse whose duration is $\ll T$ is a sinc function whose sidelobes oscillate at a frequency proportional to their distance from the centroid. The interference frequency is therefore fixed over a large spatial range so that any photodetector within the sinc function envelope will respond with the proper output. This result can be seen by noting that Eq. (8) contains a term $\exp(-jpvt)$ that, when multiplied by the term $\exp[+j(p + p_d)vt]$ from the reference beam as given by Eq. (10), produces a fixed interference frequency.

A second benefit of narrowband filtering is in resolving two signals closely spaced in frequency. As shown in Fig. 2, two received signals spaced by $1/T$ Hz

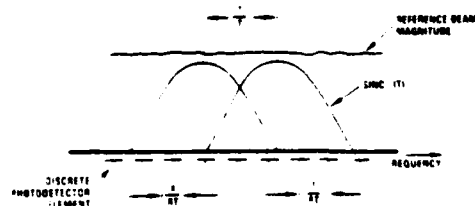


Fig. 2. Reference and signal beam distribution in the Fourier plane for two cw signals.

may occur at any position relative to a set of photodetector elements. We must ensure that the response from a photodetector is sufficiently high when it is sampling the light at the centroid of any sinc function to provide accuracy and sufficiently low at the midpoint between sinc functions to provide resolution. Since the received signals may occur at any position relative to the photodetectors, we must find a way to relate the number of photodetectors per frequency, the spatial duty cycle, and the postdetection bandwidth to the required dip between resolvable frequencies.

The first step is to determine the response of a fixed photodetector to a cw signal as a function of its frequency. The output of the photodetector will be the convolution of a $\text{sinc}(fT)$ function with the rectangular function of width d/RT (representing the photodetector), followed by a multiplication with the bandpass filter function. The postdetection filter function is approximated by a uniform response for $|f| \leq b/2T$ and a linearly decreasing response from $|f| = b/2T$ to $|f| = q/2T$ as shown in Fig. 3. This function is, aside from passband and stop-band ripple, similar to that produced by an elliptic filter. Since the convolution is nearly constant over the defined range of frequencies, the net result can be represented by

$$C(f) = d/RT; \quad 0 \leq |f| \leq b/2T,$$

$$= \frac{d}{RT} - \frac{2d}{R(q-b)} (f - b/2T); \quad b/2T \leq |f| \leq q/2T, \quad q \neq b,$$

$$= 0; \quad |f| \geq q/2T. \quad (17)$$

The smallest dip between two frequencies occurs when the midpoint between the frequencies falls between two photodetectors. This condition is shown in Fig. 4 where we show $C(f)$ centered at the positions corresponding to two resolvable frequencies. Since we have already accounted for the convolutional effects introduced by photodetectors having a finite size, we can now determine the response from a given photodetector by using the value of $C(f)$ at a point corresponding to the center of the photodetector. The output of the photodetector nearest the center of $C(f)$ is equal to $C(f_0)$. The largest possible value of $|f_0|$ is $1/2RT$, and we require that the output be constant for any frequency less than $|f_0|$. By referring to Fig. 3, we see that this condition is satisfied if

$$R \leq 1/b. \quad (18)$$

The outputs from the two photodetectors symmetrically positioned about the midpoint are equal and have values given by $C(f_1)$. The second relationship can then be obtained by requiring that

$$C(f_1) \leq hC(f_0), \quad (19)$$

where $0 < h < 1$ is the desired dip between the two frequencies. Since $f_1 = 1/2T - 1/2RT$, we use Eqs. (17) and (19) to obtain the relationship that

$$R \geq \frac{1}{1 - q(1 - h) - hb}. \quad (20)$$

The inequalities as given by Eqs. (18) and (20) must be satisfied to achieve a given dip between frequencies

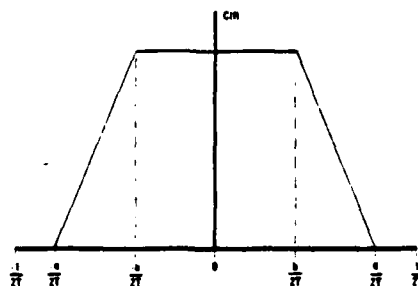


Fig. 3. Convolution of a $\text{sinc}(fT)$ function and a photodetector of width d/RT .

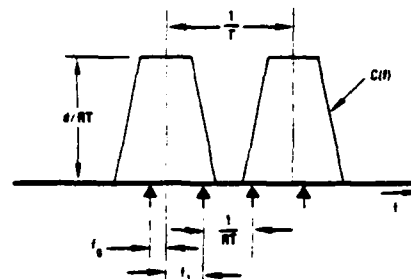


Fig. 4. Worst-case signal position relative to the photodetectors for resolving two frequencies.

as well as to ensure that the magnitudes of the frequencies are accurately measured. In the limit as the slope of the filter becomes very high, we have that $q = b$ and Eq. (20) reduces to $R \geq 1/(1 - b)$. If Eq. (18) is also satisfied, we find that $R = 2$ is the minimum number of photodetectors per resolvable frequency.

For $h = 0.5$, which corresponds to a 3-dB dip between frequencies, Eq. (20) becomes

$$R \geq \frac{1}{1 - q/2 - b/2}. \quad (21)$$

Again, if we use the equality from Eq. (18), and let $q = 2b$, we have that $b = 0.4$ and $R = 2.5$.

One of the key advantages of using narrowband postdetection filtering, then, is to provide the necessary dip between cw signals with a number of photodetectors per frequency that is close to the theoretical limit. The natural dip between the two Rayleigh resolved frequencies will vary from zero to 1.3 depending on the relative phases of the two spectral components. Equation (20) shows that a fixed dip of value h can be achieved independently of the phase relationship without increasing the length of the Bragg cell to separate physically the spectral components.

We now calculate the relationship between R and the Bragg cell length for a power spectrum analyzer. Gaussian illumination is generally used to control the sidelobe levels to meet the cross talk requirements. This, in turn, causes a loss in resolution which must be restored by increasing the Bragg cell length. We denote the increased cell length by L_1 so that the input aperture illumination function, in terms of amplitude, is given by

$$a(x) = A_1 \exp(-4T_1^2 x^2/L_1^2), \quad (22)$$

where T_1 is a truncation ratio whose value is chosen to control the sidelobe level.⁷ The intensity response of the system to a cw input frequency is then obtained by squaring the Fourier transform of $a(x)$:

$$I(p) \propto \exp(-p^2 L_1^2/8T_1^2). \quad (23)$$

By following the same procedure as before, we find that the convolution of $I(p)$ with a small photodetector of width d/RT yields a normalized result that is very close to being Gaussian:

$$C(f) = \frac{d}{RT} \exp\left(-\frac{4\pi^2 L_1^2}{8v^2 T_1^2} f^2\right), \quad (24)$$

where we have replaced pv with $2\pi f$. The worst-case condition for resolving two frequencies occurs when the midpoint between those frequencies lies at the midpoint between two photodetectors. Since the intensities add, the relationship that must be satisfied is

$$C(f_1) + C\left(f_1 + \frac{1}{RT}\right) \leq hC(f_0), \quad (25)$$

where $f_1 = (R-1)/2RT$ and the maximum value of $|f_0|$ is $1/2RT$ as before. For a dip of $h = 0.5$ between frequencies, we find that Eq. (25) is satisfied when

$$L_1 = 0.76T_1 LR/(R-1). \quad (26)$$

Suppose we set $R = 2.5$ for comparison purposes and set $T_1 = 1.7$ which ensures that the maximum sidelobe is down by at least 40 dB.⁷ We then find that $L_1 = 2.15L$ which shows that the length of a Bragg cell used in a power spectrum analyzer must be more than twice as long as that required for an interferometric spectrum analyzer. The impact of the larger aperture required in a power spectrum analyzer is significant since the increased length translates directly into the need for an increased time-bandwidth product to achieve equivalent performance.

Another advantage of the interferometric approach is that any scattered noise caused by stationary elements in the system is rejected by the narrowband filter because it does not interfere to produce in-band components. This feature also causes the light distribution at the optical axis to be rejected.

We conclude this section by calculating the value of the parameter β which is equal to one half of the ratio of the width of the photodetector d/RT to the spacing $1/T$ between resolvable frequencies. We choose $d = 0.7$, which, for $R = 2.5$, gives a value for β equal to 0.14; this value justifies several assumptions made in Sec. II in connection with deriving Eq. (16).

IV. Reference Waveforms

In Sec. II we used a narrow pulse as the reference-beam waveform to develop the basic theory of a fixed offset frequency interferometric spectrum analyzer. The narrow pulse approximates a delta function that provides most of the desired properties of the reference waveform in the Fourier plane which are that (1) the amplitude should be uniform in spatial frequency; (2) the spatial and temporal frequencies should be coupled

so that, with a geometric displacement of the reference waveform, a fixed offset frequency is produced at each photodetector location; (3) the amplitude should not be a function of time; (4) the duty cycle should be high so that short duration signals are not missed; and (5) the light is efficiently used. The major drawback to the use of a narrow pulse as the reference signal is that a fraction of only $1/TW$ of the light at the Bragg cell is intercepted by the pulse.

An equivalent way to generate a traveling pulse is to use a chirp waveform to activate a Bragg cell situated so that the focused beam scans across plane P_3 . If we project the rays produced by a traveling impulse from plane P_3 toward the source, we find that the Bragg cell must have a length equal to $2L$, given that the chirp rate is equal to the bandwidth of the signal divided by the processing time T . The focal length of the chirp is then equal to $L^2/\lambda TW$, which is of the order of several meters for typical values of these parameters. The advantages of this approach are that sharply formed impulses are produced at plane P_3 and that the resultant reference beam in the Fourier plane is a plane wave. The disadvantages are that a Bragg cell of twice the time-bandwidth product is required and the length of the optical system is excessive.

Another way to generate the reference beam is to drive the Bragg cell in plane P_3 with a chirp directly.⁸ Lens L_2 then focuses the chirp at plane P_4 so that, at the Fourier plane, the expanding beam covers the signal spectrum. The chirp waveform can be represented by

$$r(t) = \cos\left(\omega_c t + \frac{\pi W}{T} t^2\right)$$

for a chirp of increasing frequency on a carrier ω_c . The Fourier transform of the chirp, valid over the spatial frequency range corresponding to the bandwidth of the signal, is

$$\begin{aligned} A_2(p, t) &= jm_2 A_2 \int_{-L/2}^{L/2} \exp\left[-j\left[\omega_c + \frac{\pi W}{T}(t - T - x/v)\right] \right. \\ &\quad \times (t - T - x/v)\left.\right] \exp[-j(p + p_d)x] dx \\ &= \frac{jm_2 A_2 L}{\sqrt{TW}} \exp(j\phi) \exp[-j(p + p_d)vt] \\ &\quad \times \exp\left[-j\frac{vL}{4\pi W}(p + p_d - p_c)^2\right], \end{aligned} \quad (27)$$

where $2\pi W$ is the bandwidth of the rf signal and the chirp rate is $2\pi W/T$. We see that Eq. (27) is similar to Eq. (10) but with two notable differences: (1) the amplitude is larger by \sqrt{TW} , which increases the efficiency of the system; and (2) the sinc function envelope is replaced by a Fresnel amplitude diffraction pattern.

Figure 5(a) shows the focused spot at plane P_4 for the instant in time when the Bragg cell is just filled with one chirp function. At plane P_2 , the spatial extent of the reference beam is equal to that of the signal spectrum; the amplitude is uniform except near the edges of the spectrum where the ripple effects of the Fresnel diffraction pattern are evident. At a time $T/2$ sec later, the reference waveform consists of parts of two chirp functions that produce two focused spots in plane P_4 as

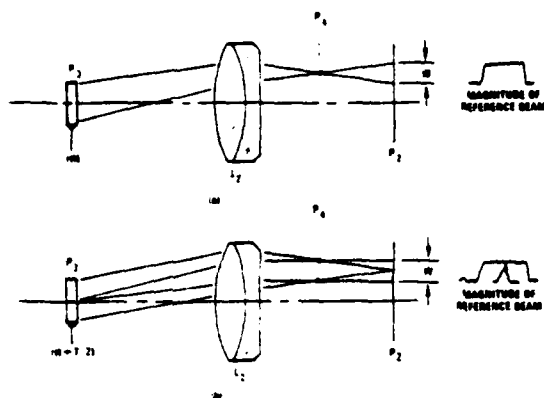


Fig. 5. Chirp reference beam: (a) Bragg cell with one chirp segment, and (b) Bragg cell with one half of two chirp segments.

shown in Fig. 5(b). Each spot has increased in width by a factor of 2 but each expands to cover only one half of the spectral range. Thus, as the chirp waveforms move through the Bragg cell, the reference waveform in the Fourier plane will generally consist of two segments of Fresnel patterns which move at the same velocity. If the chirp duty cycle is not 100%, there will be a small gap between segments which should not adversely affect the performance of the system.

When the chirp waveform is used, the integrated intensity of the desired output term is similar to Eq. (15), except that TW is replaced by \sqrt{TW} , and the chirp produces a residual spatial fluctuation that is a potential source of time-amplitude modulation on the output current of the photodetector. Since the Fresnel pattern travels at a high velocity, the modulation is well outside the postdetection bandwidth so that there is no temporal modulation on the output due to spatial fluctuations.

A second type of time-amplitude modulation of the reference function at the Fourier plane arises from the movement of the input chirp waveform under the Gaussian input illumination. A frequency ω_j within the bandwidth of the chirp will appear at a fixed position p_j in the Fourier plane; its amplitude as a function of time, however, is determined by its position in the input plane. Since a severe truncation of the Gaussian illumination is not needed to control the sidelobe levels, we can reduce the amplitude variation at the expense of some loss of light. A reasonable compromise is to truncate the Gaussian illumination at the $\exp(-1/2)$ points at the edges of the aperture which leads to a $\pm 25\%$ variation in the output current over the time interval T . This time-amplitude modulation is not a concern because it can be eliminated by the bandpass filter if $f_d \gg 1/T$. The chirp reference waveform therefore satisfies most of the requirements set forth at the beginning of this section.

An alternative reference-beam waveform that is continuous in time is a pseudonoise sequence (PNS) whose Fourier transform also satisfies many of the stated requirements. These sequences and similar

codes have been studied for applications such as generating random phase masks for holography, recovering imagery from coded aperture systems, and spectral shaping.⁹⁻¹⁶ Generally, only the spatial properties of these codes have been considered; we are interested in both the spatial and temporal properties of their Fourier transforms to determine whether they are better than those of a chirp waveform.

A shift register sequence is one whose period, or frame length, is $N \leq 2^r - 1$, where N is the number of elements in the frame and r is an integer. If the period is equal to $2^r - 1$, the sequence is said to have maximal length and has the properties (1) that in every period the difference between the number of +1's and -1's is equal to one; (2) that in every period the longest run of +1's and -1's is equal to r , and for each run of length $m + 1$ there are two runs of length m ; and (3) that the autocorrelation function has only two values. Such sequences can be produced by an r -stage linear shift register having the appropriate feedback.¹⁷

Figure 6 shows the magnitude of the Fourier transform of an $N = 2^5 - 1 = 31$ element sequence at time $t = 0$ and $t = T/31$; that is, in a time interval corresponding to one shift position of the PNS in the input plane, the magnitude changes by the amount shown. At the integer frequencies the normalized magnitude is exactly equal to one for any shift position.¹⁷ The Fourier transform is symmetric about the spatial frequency $N/2$; in an optical system the sequence modulates a carrier so that the spectrum is centered at p_c . In practice the input waveform will consist of a sequence of narrow pulses so that the spectrum must be shifted and multiplied by a sinc function as given by Eq. (10).

As shown in Sec. III, we need at least 2.5 photodetectors per resolvable frequency which means that some photodetectors will be located where the spectrum is not uniform in either space or time. Further, since photodetectors of finite size must be used to collect optical

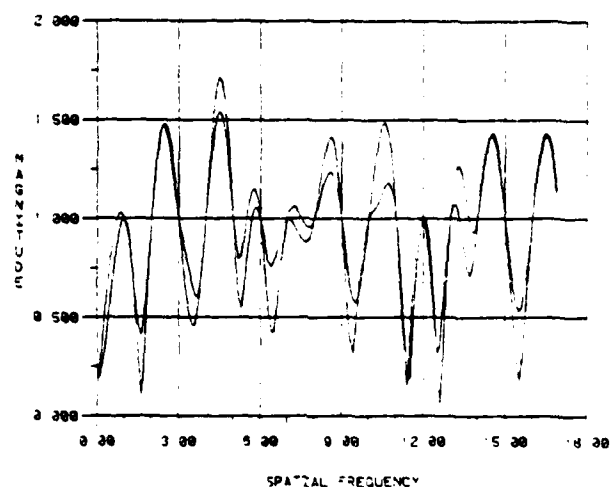


Fig. 6. Magnitude of the Fourier transform of a pseudonoise sequence for two adjacent shift positions.

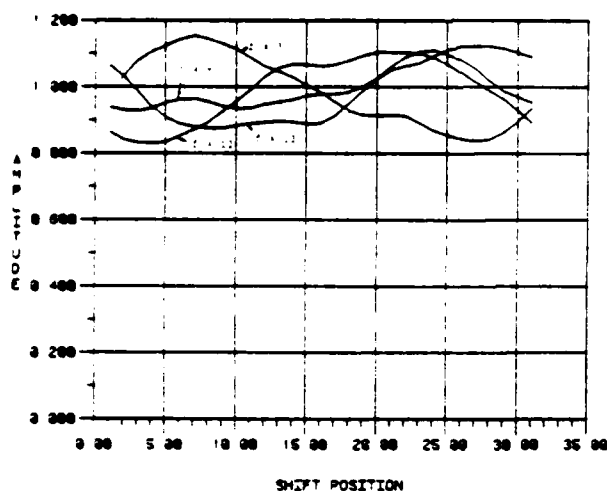


Fig. 7. Magnitude as a function of shift position for four frequencies.

power efficiently, we investigated the spatial and temporal variations in amplitude for finite photodetectors. Figure 7 shows the magnitude variation as a function of shift position (equivalent to time) for a photodetector whose width is $d/RT = 0.28$, centered at four different spatial frequencies. The variation in magnitude as a function of time is of the order of $\pm 15\%$, which is caused by using a Gaussian input illumination beam truncated at the $\exp(-1/2)$ points in amplitude at the edges of the sequence. We note that the functions are the sums of sinusoidal functions whose frequencies are $1/T$ and multiples thereof; these components can also be removed by the narrowband filter. As noted before, the instantaneous output of a spectrum analyzer is generally integrated for at least T sec. Figure 8 shows the average value of the amplitude as a function of spatial frequency for a full frame of the PNS. Except at zero spatial frequency, where the magnitude is low because the average value of the sequence is low, the average magnitude varies by $\pm 5\%$. These variations, along with others such as Bragg cell frequency roll-off and the sinc function weighting, can be compensated when the system is calibrated.

The question of whether the temporal frequencies of these candidate waveforms are continuous functions of the spatial frequency variable depends on the waveform and the postdetection process. Equations (8) and (27) suggest that the spectrum of a moving impulse or a chirp waveform is indeed continuous so that the theory is valid if the output is sampled, after narrowband filtering and envelope detection, once for each time period T . The results are less clear for the PNS because the Fourier transform cannot be calculated in the same way. Some insights can be gained for the case of longer observation times such that the reference waveform is repetitious with period T .

Let $f(x)$ represent the amplitude of the reference beam over the time interval T and let $F(p)$ be its Fourier transform. Suppose that this distribution is repeated

at intervals of L and that the entire distribution moves with velocity v . The Fourier transform of the extended signal $g(x)$ is then

$$G(p) = v \exp(-jput) F(pv) \frac{1}{T} \sum_{n=-\infty}^{\infty} \delta(pv/2\pi - n/T). \quad (28)$$

We now account for the finite aperture in the input plane by convolving $G(p)$ with the aperture function $A(p) = L \text{sinc}(pL/2\pi)$ to get

$$G(p) = \sum_{n=-\infty}^{\infty} F\left(\frac{2\pi n}{T}\right) \exp(-j2\pi n t/T) \text{sinc}(pv/2\pi - n/T). \quad (29)$$

Equation (29) shows that the Fourier transform consists of a set of sinc functions spaced at intervals of $2\pi/L$, which is consistent with our notion of the spatial resolution of the optical system. These sinc functions take on the sample values $F(2\pi n/T)$ and oscillate at a temporal frequency of $2\pi n/T$. The final step is to multiply $G(p)$ by $\text{sinc}(pL/2\pi TW)$ to account for the finite duration of each pulse in the PNS or by a rectangular function for the case of a chirp.

If we observe the output of a given photodetector for a long time period $T' \gg T$, we will see the discrete nature of the temporal spectrum of the reference beam. Furthermore, if we increase the frame length of the PNS so that it is greater than T but less than T' , we will note that the discrete temporal frequency resolution will increase whereas the spatial frequency resolution is fixed. The exact nature of the output for the candidate waveforms and an observation time of the order of T will be deferred to a later paper where we will discuss the experimental results.

V. Laser Power and Dynamic Range

The current produced by a photodetector is given by Eq. (16); the values of A_1 and A_2 are given by

$$A_1 = \left(\frac{\alpha P}{L}\right)^{1/2}, \quad A_2 = \left[\frac{(1-\alpha)P}{L}\right]^{1/2}, \quad (30)$$

where P is the power of the laser and α is the fraction of the power directed into the signal beam. The output current can then be arranged in the form

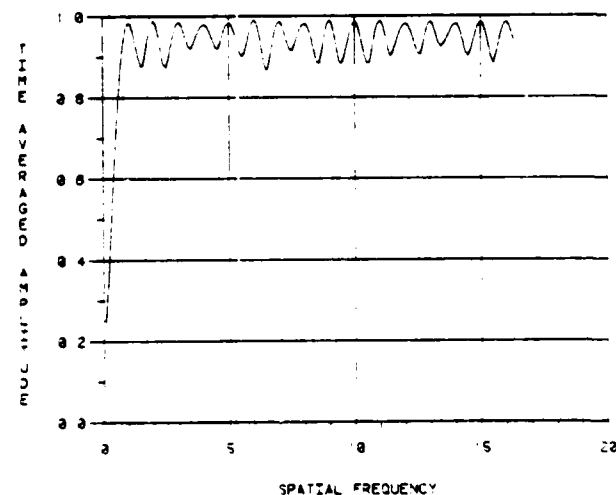


Fig. 8. Magnitude averaged over a frame period as a function of spatial frequency.

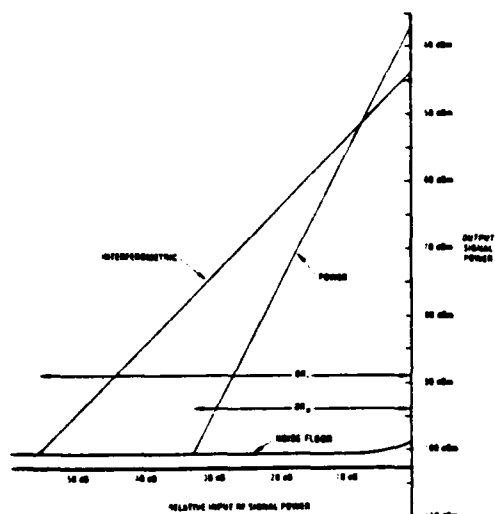


Fig. 9. Dynamic range for interferometric and power spectrum analyzers.

$$i(t) = i_1 + i_2 + i_3(t)$$

$$= aP(1 - \alpha) + bP\alpha + cP[\alpha(1 - \alpha)]^{1/2} \cos(\omega_d t + \phi), \quad (31)$$

where the coefficients a , b , and c contain the values of parameters associated with various system components. Equation (31) represents the general form of the output of any interferometric system, and the SNR is given by the ratio of the output signal power to the sum of the shot noise and thermal noise powers:

$$\text{SNR} = \frac{\langle i_3^2(t) \rangle R}{2eB(i_d + i_1 + i_2)R + 4kTB}, \quad (32)$$

where the brackets denote time average, R is the load resistance of the photodetector, e is the charge of an electron, B is the bandwidth, i_d is the photodetector dark current, k is Boltzmann's constant, and T is the equivalent system temperature in degrees kelvin. By using Eq. (31) in (32), we obtain

$$\text{SNR} = \frac{0.5c^2P^2\alpha(1 - \alpha)}{D[aP(1 - \alpha) + bP\alpha] + F}, \quad (33)$$

where $D = 2eB$ and $F = (2eBi_d + 4kTB/R)$.

We want to find the minimum laser power required to achieve a given dynamic range. The procedure is to solve Eq. (33) for the laser power required to produce a detectable signal (a SNR of 1) when c has its minimum value as determined from the required dynamic range. After some algebraic manipulations, we find that the minimum laser power is obtained when

$$\alpha = \frac{g + 1}{2g + 1}, \quad (34)$$

where $g = (Fc^2/2D^2a^2)^{1/2}$. The minimum laser power is then

$$P_{\min} = \frac{2Da(2g + 1)}{c^2}. \quad (35)$$

We are now in a position to make some numerical calculations using Eq. (16) as our basis for determining the values of the constants in Eq. (31). We will assume that the efficiency of each optical path is $\epsilon_s = \epsilon_r = 1/2$,

that the sensitivity of the photodetector is $S = 0.5 \text{ A/W}$, and that $\beta = 0.14$. The modulation indices m_1 and m_2 are chosen to keep the intermodulation products at an acceptable level. If we require third-order two-tone intermodulation products to be down by at least 50 dB when 20% of the possible cw signals in the Bragg cell are saturated, we must keep the diffraction efficiency per frequency to <0.01 . Since the modulation index is equal to the square root of the diffraction efficiency, we have that $m_1 = 0.1$. The diffraction efficiency of the reference beam can be much higher because intermodulation products are not a factor; we choose $m_2 = 0.7$. We will also use a time-bandwidth product of $TW = 100$, and, if we use the chirp reference-beam waveform, we replace TW by \sqrt{TW} in Eq. (16) so that

$$i(t) = i_1 + i_2 + i_3(t) \quad (36)$$

$$= 7(10^{-4})C_k^2P\alpha$$

$$+ 3.5(10^{-4})P(1 - \alpha) + 9.8(10^{-4})C_kP[\alpha(1 - \alpha)]^{1/2}, \quad (37)$$

from which we note that $a = 3.5(10^{-4})$, $b = 7(10^{-4})C_k^2$, and $c = 9.8(10^{-4})C_k$.

The value of g is a function of the parameters associated with the photodetector elements and the required dynamic range. A dynamic range of 60 dB in terms of input signal power yields a minimum value of $C_k = 10^{-3}$ from which we have that $c_{\min} = 9.8(10^{-7})$. We chose a photodetector having a dark current of $i_d = 10^{-9} \text{ A}$, a bandwidth of $B = 1 \text{ MHz}$, and a load resistance value of $R = 50 \text{ k}\Omega$. From these parameters we calculate that $g = 7.2$ and, from (35), that the minimum laser power is $P = 3.2 \text{ mW}$.

We now calculate the dynamic range produced by a power spectrum analyzer that has the same system parameters. The SNR for a power spectrum analyzer can be given in a form similar to Eq. (32):

$$\text{SNR} = \frac{\langle i_1^2 \rangle R}{2eB(i_d + i_1)R + 4kTB}, \quad (38)$$

where $i_1 = 7(10^{-4})C_k^2P$; we have set $\alpha = 1$ because all the laser power can be directed into the signal beam. The dynamic range can be found by setting the $\text{SNR} = 1$; we then have

$$\text{DR}_P = 10 \log[7(10^{-4})P/\sqrt{F}], \quad (39)$$

which, for a laser power of 3.2 mW, gives a dynamic range of 33 dB. We find that the interferometric spectrum analyzer provides 27 dB more dynamic range than a power spectrum analyzer for the set of parameters given.

It is frequently cited in the literature that an interferometric spectrum analyzer provides twice the dynamic range in decibels as that produced by a power spectrum analyzer. We now examine in more detail the relationships between the interferometric and power spectrum analyzer dynamic ranges. In Fig. 9 we graph the output signal power, as given by the numerators of Eqs. (32) and (38), as a function of the rf input signal power. The noise floor is established by the noise equivalent power of the photodetector, except at high input signal levels where the system has a slightly higher noise floor caused by signal dependent shot noise.

As expected, the output vs input line for a power spectrum has a slope of two, whereas the slope is one for an interferometric spectrum analyzer. For a given laser power, the vertical axis intercept point is lower for the interferometric spectrum analyzer because (1) half of the laser power is lost by the recombining beam splitter, and (2) the reference-beam power is spread over a larger range of spatial frequencies so that the reference-beam amplitude at any particular photodetector is low.

The dynamic range is determined by the points at which the two input/output lines intercept the noise floor. A relationship between the interferometric dynamic range (DR_I) and the power dynamic range (DR_P) can be obtained by substituting the laser power, as given by Eq. (35), required to provide a given DR_I into Eq. (39). We can simplify Eq. (35) for the case of g very much greater than one to the form

$$P = \sqrt{8F/c}. \quad (40)$$

Since $DR_I = 20 \log(C_k)$ and $c = 9.8(10^{-4})C_k$, we can rearrange Eq. (39) in the form of

$$DR_I = 2DR_P - 10 \log(TW/25). \quad (41)$$

This result shows that, in the limit of small time-bandwidth products, the interferometric system does provide twice the dynamic range in decibels as expected. A small time-bandwidth product has the effect of closing the gap between the vertical axis intercept points shown in Fig. 9 so that the superior performance of the interferometric approach is evident at higher input signal levels. We also note from Eq. (41) that the improvement factor asymptotically approaches two as the absolute performance level increases for a fixed value of TW .

VI. Summary and Conclusions

The dynamic range of a power spectrum analyzer is generally limited by the dynamic range available from self-scanned photodetector arrays. Furthermore, the output current is proportional to the input rf power so that a significant amount of laser power is needed to achieve a high dynamic range. Interferometric spectrum analyzers produce an output that is proportional to the input rf magnitude and generally provide more dynamic range for a given laser power.

In this paper a technique is described wherein the reference beam is spatially modulated and geometrically shifted so that the interference temporal frequency is constant over the entire spectrum. This fixed frequency offset permits a narrowband postdetection filter to separate the signal term from the bias terms at the output. Furthermore, the filter rejects sidelobe contributions from nearby cw signals so that reduced cross talk levels can be achieved without the need to weight the input illumination. A more uniform input illumination, in turn, leads to better short-pulse detectability because the pulse amplitude is more constant over the processing time of the cell. A further advantage of the interferometric technique is that scattered light does not contribute to the output because it falls outside the bandwidth of the filter.

Two types of reference-beam modulation have been studied. A chirp waveform, having the same bandwidth at the rf signal, provides a continuum of spatial and temporal frequencies at the output plane and, for most applications, has adequate amplitude stability as a function of space and time. We also investigated the properties of pseudonoise sequences; the same post-detection filtering techniques apply, and, for very short-pulse or cw signals, the results are similar to those obtained from the chirp waveform except that the sidelobe suppression effect may not be as strong as with the chirp waveform. A potential advantage of the pseudonoise sequence waveform is that it can be recirculated through the Bragg cell and provides phase continuity at the output of the system. The choice of which reference-beam modulation to use is dependent on the application.

We have also determined the minimum laser power required to achieve a given dynamic range and compared the performance of an interferometric and a power spectrum analyzer having the same operating parameters. The dynamic range of the interferometric system is, in the limit of small time-bandwidth products, a factor of 2 larger in decibels than that of a conventional system. The improvement in the dynamic range is a function of the time-bandwidth product and the absolute dynamic range obtained.

I thank E. H. Young, Jr., for discussions on the concept of a fixed offset frequency based on his earlier unpublished work, M. L. Shah for discussions and experimental work on the spectrum of pseudorandom sequences, and G. H. Thaker for the computer simulations of the spectrum of pseudorandom sequences. Special thanks to A. M. Bardos for stimulating discussions and viewpoints throughout this work which was partially supported by the U.S. Army Research Office and by the U.S. Air Force Avionics Laboratory.

References

1. L. B. Lambert, IRE Int. Conv. Rec. 10, 69 (1962).
2. M. C. King, W. R. Bennett, L. B. Lambert, and M. Arm. Appl. Opt. 6, 1367 (1967).
3. T. M. Turpin, Proc. IEEE 69, 79 (1981).
4. T. R. Bader, Proc. Soc. Photo-Opt. Instrum. Eng. 232, 1 (1980).
5. A. M. Bardos, R. H. Nelson, H. N. Roberts, and C. A. Shuman, Proc. Electro-Optic Systems Design Conference, Anaheim, Calif., 1975.
6. G. M. Borsuk, Proc. IEEE 69, 100 (1981).
7. D. L. Hecht, Proc. Soc. Photo-Opt. Instrum. Eng. 90, 148 (1976).
8. M. L. Shah, Harris Corp.; private communication.
9. C. B. Burckhardt, Appl. Opt. 9, 695 (1970).
10. R. H. Katyl, Appl. Opt. 11, 198 (1972).
11. W. C. Stewart, A. H. Firester, and E. C. Fox, Appl. Opt. 11, 604 (1972).
12. D. C. Chu and J. W. Goodman, Appl. Opt. 11, 1716 (1972).
13. W. J. Dallas, Appl. Opt. 12, 1179 (1973).
14. M. C. Gailagher and B. Liu, Appl. Opt. 12, 2328 (1973).
15. T. F. Knie, M. O. Hagler, W. D. Redus, and J. F. Waikup, Appl. Opt. 18, 52 (1979).
16. E. E. Fenimore, Appl. Opt. 19, 2165 (1980).
17. S. W. Golomb, Shift Register Sequences (Holden-Day, San Francisco, 1967).

APPENDIX B

BRAGG CELL DIFFRACTION PATTERNS

REPRINTED FROM APPLIED OPTICS

VOLUME 21, PAGE 1092, MARCH, 1982

Bragg cell diffraction patterns

A. VanderLugt

The 2-D diffraction patterns produced by fully illuminated Bragg cells can be characterized by curved singularity functions. The degree of curvature is related to the optical wavelength, the acoustic wavelength, and the degree of anisotropy of the interaction material. Analytical expressions are derived for the singularity functions, and the impact of the nonideal diffraction pattern in certain signal processing problems is calculated. The most notable effect is an increase in the sidelobe levels and a slight loss in resolution when Bragg cells are used in spectrum analyzers. Truncation of the diffraction pattern or the use of the line illumination, when possible, reduces the degradation of the diffraction pattern.

I. Introduction

Bragg cells are widely used as modulators, beam deflectors, and analog or digital delay lines for signal processing.¹ In each case light waves interact with sound waves, produced by an electrical/acoustic transducer, so that the light is modulated in space and time. The quality of the optical wave front is particularly important in applications such as spectrum analysis, wherein the resolution of the system is significantly reduced if the wave front is distorted.

One method for testing the optical quality of a wave front is to use Fourier analysis techniques which give a direct measure of performance. We examined the Fourier transforms of various Bragg cells operating in the longitudinal wave mode. The diffraction pattern was the expected 2-D sinc² function, except that in one dimension the function was curved toward the optical axis.

The purpose of this paper is to analyze this phenomenon for both isotropic and anisotropic interaction materials, to illustrate the phenomenon for certain types of Bragg cells, and to calculate its effect on the performance of some optical processing systems.

II. Theory

One way to visualize the optical wave front produced by a Bragg cell is through use of a schlieren imaging technique. Figure 1 shows a schlieren image of a lead

molybdate (PbMoO₄) device operated in the longitudinal mode at a 400-MHz frequency. In the near field of the transducer, the acoustic waves interfere to produce an intricate pattern that has been studied by Cook *et al.*² A null is formed at a distance $\sim H^2/8\Lambda$ from the transducer, where H is the height of the transducer and Λ is the acoustic wavelength. As the distance from the transducer increases, the acoustic waves diverge to produce the far-field interference pattern. Several studies have been made in which the sound pressure fields have been calculated and measured by optical probing techniques.³⁻⁹ These analyses begin with the observation that the transducer is equivalent to an optical source so that the sound field can be calculated by using the Huygens-Fresnel diffraction formula. The excitation produced by a finite source is decomposed into a family of plane waves, and the far-field pattern is generally expressed in terms of an angular spectrum.

We take a related approach in which we start with the sound field produced by a transducer of infinitesimal height and account for its finite height after we find the Fourier transform of the coupled optical waveform. Our model for the acoustic wave front is described with reference to Fig. 2. The Bragg cell is located in plane P_1 , having coordinates x and y , which lies in the front focal plane of a lens having focal length F . The Bragg cell has length L in the x direction; the transducer has a height H in the y direction and a width W in the direction of the optical axis. The cell is illuminated by a uniform collimated beam of monochromatic light. The acoustic wave produced by a wide transducer having a very small height can be represented as cylindrical sheets that diverge in the y direction as they propagate in the x direction. We shall assume that the width of the transducer is nearly equal to the width of the Bragg cell and ignore effects due to reflections.

The author is with Harris Corporation, Advanced Technology Department, P.O. Box 37, Melbourne, Florida 32901.

Received 19 October 1981.

0003-6935/82/061092-09\$01.00/0.

© 1982 Optical Society of America.



Fig. 1. Schlieren image of a lead molybdate Bragg cell (400 MHz).

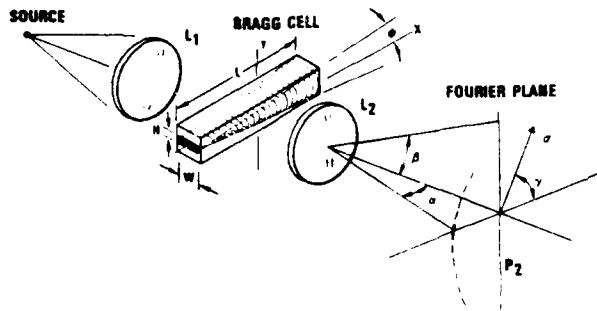


Fig. 2. Fourier transform setup for displaying diffraction patterns.

The acoustic wave front propagation within the cell is similar to the optical wave front propagation from a line source. Given an ideal interaction between light and sound, the optical wave front at the exit side of the Bragg cell for the negative first-order diffracted light is

$$a(x,y) = \frac{1}{\sqrt{j\Delta r}} \exp(-j2\pi r/\Lambda) \exp(-\epsilon r), \quad (1)$$

where $r^2 = x^2 + y^2$ and ϵ is a parameter that accounts for the frequency dependent attenuation of the acoustic wave as it propagates. We have suppressed the time dependence of this propagating wave because we are interested in only the spatial characteristics of the resulting diffraction pattern. The optical wave front as given by Eq. (1) does not account for the Bragg angle matching conditions which change the amplitude as a function of the acoustic frequency. These effects are not of fundamental importance here; we are interested in the form of the normalized diffraction pattern of a single acoustic frequency.

We first consider the situation for a Bragg cell made from an isotropic medium in which the acoustic velocities are equal in all directions. The Fourier transform of $a(x,y)$ is given by

$$A(\alpha,\beta) = \int_{P_1} \int \frac{1}{\sqrt{j\Delta r}} \exp(-j2\pi r/\Lambda) \exp(-\epsilon r) \times \exp\left[-j\frac{2\pi}{\lambda}(\alpha x + \beta y)\right] dx dy, \quad (2)$$

where $\alpha = \arctan(\xi/F)$ and $\beta = \arctan(\eta/F)$; the variables ξ and η are the physical coordinates in the Fourier transform plane. We now change to polar coordinates by letting $x = r \cos\theta$ and $y = r \sin\theta$ so that Eq. (2) becomes

$$A(\alpha,\beta) = \int_0^L \int_{-\pi/2}^{\pi/2} \frac{1}{\sqrt{j\Delta r}} \exp(-j2\pi r/\Lambda) \exp(-\epsilon r) \times \exp\left[-j\frac{2\pi r}{\lambda}(\alpha \cos\theta + \beta \sin\theta)\right] r dr d\theta, \quad (3)$$

where the region of integration extends over the semi-circle in the right-hand plane of the Bragg cell. It is also convenient to convert the coordinates in the Fourier plane to the polar form; that is, let $\alpha = \sigma \cos\gamma$ and $\beta = \sigma \sin\gamma$. Considering the integration on θ first, we have

$$G(r,\sigma,\gamma) = \int_{-\pi/2}^{\pi/2} \exp\left[-j\frac{2\pi r\sigma}{\lambda} \cos(\gamma - \theta)\right] d\theta, \quad (4)$$

which is independent of γ and equal to 1^0

$$G(r,\sigma) = 2\pi J_0(2\pi r\sigma/\lambda), \quad (5)$$

where $J_0(z)$ is the zeroth-order Bessel function of the argument z . We now use $G(r,\sigma)$ in Eq. (3) to obtain

$$A(\sigma) = \int_0^L \frac{2\pi r}{\sqrt{j\Delta r}} J_0(2\pi r\sigma/\lambda) \times \exp(-j2\pi r/\Lambda) \exp(-\epsilon r) dr, \quad (6)$$

We can extend the upper limit to infinity if we multiply the integrand by $\text{rect}(r/L - 1/2)$, and, after Eq. (6) has been solved, we account for the finite length of the Bragg cell through a convolution in σ with a function $W(\sigma)$, which is the Fourier transform of the product $\text{rect}(r/L - 1/2) \exp(-\epsilon r)$. The solution to Eq. (6) is given by the relationship¹¹

$$\int_0^\infty \exp(-at) J_\nu(bt) t^{\mu-1} dt = \frac{\left(\frac{b}{2a}\right)^\nu \Gamma(\mu+\nu)(a^2+b^2)^{1/2-\mu}}{a^{\mu-1/2} \Gamma(\nu+1)} \times F\left(\frac{\nu-\mu+1}{2}, \frac{\nu-\mu}{2}+1; \nu+1; -\frac{b^2}{a^2}\right). \quad (7)$$

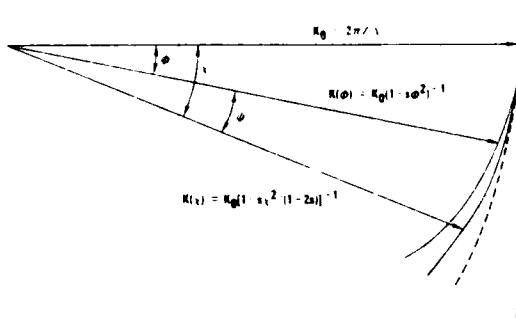


Fig. 3. Phase vector $\mathbf{K}(\phi)$ and Poynting vector $\mathbf{K}(\chi)$ plotted for $s = -1/2$. Both vectors follow the dashed circle for isotropic materials ($s = 0$).

where $F(\cdot)$ is the hypergeometric function. For our application, we have $v = 0$ and $\mu = 3/2$ so that

$$A(\sigma) = \frac{2\pi\Gamma(3/2)}{\sqrt{j\Lambda a}\Gamma(1)(a^2 + b^2)^{1/2}} F\left(-1/4, 3/4; 1; -\frac{b^2}{a^2}\right), \quad (8)$$

where $a = j2\pi/\Lambda$ and

$$b = 2\pi\sigma/\Lambda. \quad (9)$$

Since $A(\sigma)$ is the Fourier transform of a (nearly) co-phased optical wave front over the infinite half-plane, we expect $A(\sigma)$ to be a singularity function that behaves as a δ function.¹² A singularity function in σ results if $b^2 = -a^2$, provided that $a \neq 0$ and that $F(-1/4, 3/4; 1; 1)$ is finite. If $b^2 = -a^2$, we use Eq. (9) to obtain

$$\sigma^2 = \alpha^2 + \beta^2 = (\Lambda/\Lambda)^2, \quad (10)$$

which is a valid solution because $a \neq 0$, and we have that¹³

$$F(-1/4, 3/4; 1; 1) = \frac{\Gamma(1)\Gamma(1/2)}{\Gamma(5/4)\Gamma(1/4)} \approx 0.54,$$

so that the hypergeometric function is finite. The equation of the singularity function as given by Eq. (10) is that of a circle having a radius Λ/Λ centered on the optical axis. As the acoustic wavelength changes for different rf drive frequencies, the singularity function is always a circle centered on the optical axis, but its radius varies inversely with the wavelength.

To complete the analysis for isotropic crystals, we now consider the effect of the Bragg angle matching conditions which have not been explicitly included in the analysis. To maximize the amplitude of the diffracted light, the input illumination must be at the Bragg angle ($\theta_B = \lambda/2\Lambda$). If we illuminate the cell at the Bragg angle with respect to the y - z plane, the diffracted light will be maximized in the direction of $\gamma = \pi$, and the singularity occurs at $\alpha = -\lambda/\Lambda$. Since the position of the singularity is measured with respect to the point at which the undiffracted light is focused (defined here as the optical axis), we get the classical result that the angle between the diffracted and undiffracted light is twice the Bragg angle.

The singularity must also be convolved in the radial direction with $W(\sigma)$, which is the Fourier transform of $\text{rect}(r/L - 1/2) \exp(-\epsilon r)$. If the attenuation is small over

the aperture of the cell, $W(\sigma)$ can be approximated by $\text{sinc}(\sigma L/\Lambda)$. Finally, we account for the finite height of the transducer through a multiplication by $\text{sinc}(\beta H/\Lambda)$.

In an anisotropic crystal, the phase velocity of the acoustic wave varies as a function of the direction of propagation and the orientation of the crystal relative to the transducer. Waterman¹⁴ has developed relationships for the velocities and the relative changes in velocity for waves propagating in directions close to the principal axes of crystals. He shows, for example, that velocity v in the $[001]$ propagation direction for a tetragonal crystal is

$$v = (c_{33}/\rho)^{1/2}, \quad (11)$$

and the relative change in velocity in a direction close to the direction of propagation is

$$\frac{\Delta v}{v} = \frac{\phi^2}{2c_{33}} \frac{(c_{13} + c_{33})(2c_{44} + c_{13} - c_{33})}{(c_{33} - c_{44})}, \quad (12)$$

where c_{ij} are the elastic constants, ρ is the density of the crystal, and ϕ is shown in Fig. 2. For small values of ϕ we can write Eq. (12) as $\Delta v = -s\phi^2 v$, so that the phase velocity at an angle ϕ is

$$v(\phi) = v(1 - s\phi^2). \quad (13)$$

We use a negative sign in the relationship for Δv to be consistent with Papadakis⁵ and Cohen.⁸ Since the acoustic wavelength is $\Lambda = 2\pi v/\omega$, where ω is the acoustic frequency, the wavelength dependence on ϕ has the same form as Eq. (13).

We are now in a position to see how the solution to the isotropic case can be modified to account for the anisotropy of certain materials. The coupling of the optical and acoustic wave fronts requires that we first find the acoustic pressure field within the cell. In Fig. 3 we show the acoustic K vector associated with the phase velocity of a propagating wave. The magnitude of this vector at an angle ϕ is given by

$$K(\phi) = \frac{\omega}{v(\phi)} = \frac{2\pi}{\Lambda(1 - s\phi^2)}. \quad (14)$$

The acoustic energy in an anisotropic material propagates at an angle $\chi = \phi + \psi$. Auld¹⁵ derives a relationship between the magnitudes of the phase velocity and the energy velocity in which $v_e(\chi) = v(\phi)/\cos\psi$, where ψ is the angle between the phase vector and the energy (Poynting) vector. Furthermore, Papadakis⁵ shows that $\psi = -2s\phi$ so that

$$v_e(\chi) = v \left[1 - \frac{s\chi^2}{(1 - 2s)} \right], \quad (15)$$

which is valid to terms of the order of χ^2 . The magnitude of the acoustic K vector associated with the energy flow is then

$$K_e(\chi) = \frac{\omega}{v_e(\chi)} = \frac{2\pi}{\Lambda[1 - s\chi^2/(1 - 2s)]}. \quad (16)$$

The scalar product of the Poynting vector and a distance vector defines the pressure at each point within the cell. The scalar product is

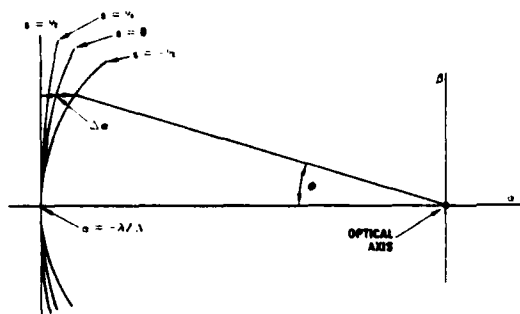


Fig. 4. Singularity curves in the Fourier plane for anisotropic Bragg cells.

$$\mathbf{K}_s \cdot \mathbf{r} = \frac{2\pi}{\Lambda} [x + y^2/2x(1 - 2s)], \quad (17)$$

where we have used the relationship that $\chi = \arctan(y/x) \approx y/x$. The Fourier transform of the optical wave front in the anisotropic case is then

$$A(\alpha, \beta) = \int_{P_1} \int \frac{1}{\sqrt{j\Lambda x}} \exp \left\{ -j \frac{2\pi}{\Lambda} [x + y^2/2x(1 - 2s)] \right\} \times \exp \left[-j \frac{2\pi}{\Lambda} (\alpha x + \beta y) \right] \exp(-\epsilon x) dx dy, \quad (18)$$

where we have replaced r by x in the denominator and in the attenuation factor because we require that χ be small. This integral is considerably more difficult to solve than Eq. (2); the solution is given in the Appendix where we find that the singularity function has the parabolic form

$$\beta^2 = \frac{\lambda(\alpha + \lambda/\Lambda)}{\Lambda(1/2 - s)}. \quad (19)$$

Although Eq. (18) is the more complete diffraction integral because it accounts for the pressure field via the Poynting vector, the same singularity function can be obtained in a simpler fashion for the special case of a continuous wave signal. In this case we cannot physically distinguish the direction of the Poynting vector since we assume that the infinitesimal transducer radiates energy in all directions. We can then find the singularity function more directly from the isotropic solution by using the scaling property of the Fourier transform. If a 2-D aperture function is extended by a scale factor in a particular direction, the diffraction pattern contracts in the same direction, and the amplitude is adjusted by the same scale factor.¹⁶ From Eq. (14) it is easily seen that the acoustic wavelength is scaled by a factor $(1 - s\phi^2)$ so that the spatial frequency σ for the isotropic case is scaled by $(1 - s\phi^2)^{-1}$ in the direction ϕ . We then have that $\sigma(\phi) = (\lambda/\Lambda)(1 - s\phi^2)^{-1}$ so that

$$\alpha = \frac{\lambda \cos \phi}{\Lambda(1 - s\phi^2)}, \quad \beta = \frac{\lambda \sin \phi}{\Lambda(1 - s\phi^2)}. \quad (20)$$

The amplitude $A(\sigma)$ as given by Eq. (8) must also be scaled by $(1 - s\phi^2)$ to obtain the result for the anisotropic case. Since the physical boundaries of the aperture do not change, the weighting functions are the same as those for the isotropic case.

The parabolic form of the singularity function can also be obtained from Eqs. (20) if we note that $\beta \approx \lambda\phi/\Lambda$ and use this value for β in the expression for α . For the negative diffracted order, we have

$$\alpha \approx \frac{-\lambda}{\Lambda} [1 - (s - 1/2)\phi^2] \approx \frac{-\lambda}{\Lambda} [1 - (s - 1/2)(\Lambda\beta/\lambda)^2],$$

from which we get the result that

$$\beta^2 \approx \frac{\lambda(\alpha + \lambda/\Lambda)}{\Lambda(1/2 - s)}$$

in agreement with Eq. (19).

In Fig. 4 we show the singularity function of anisotropic materials for several values of the parameter s . For $s = 0$, the singularity function is a sector of a circle. For $s < 0$ the singularity function curves more rapidly toward the optical axis, whereas for $s > 0$, the singularity function curves less rapidly toward the source. The horizontal difference between the spatial frequency at an angle ϕ and that at $\phi = 0$ is obtained from Eq. (20):

$$\Delta\alpha(\phi) = \alpha_0 - \alpha_s = (s - 1/2)\phi^2\lambda/\Lambda. \quad (21)$$

From this relationship we see that $s = 1/2$ results in a singularity function that is a straight vertical line passing through $\alpha = -\lambda/\Lambda$. Papadakis⁵ gives some limits on the value of s in terms of the elastic constants and argues that s must $< 1/2$. The values of s as given by Papadakis and by Waterman range from +0.38 for KCl to -5.23 for Zn. Cohen⁸ observed that a crystal for which $s = 1/2$ is one in which the acoustic beam divergence is zero. Such a crystal would produce a self-collimating acoustic beam, and the diffraction pattern would be identical to that produced by a 2-D rectangular aperture having a uniform phase weighting.

Equation (21) also shows that the magnitude of $\Delta\alpha(\phi)$ can be large if s is highly negative, which is the case for TeO₂ operated in the slow-shear mode. Furthermore, $\Delta\alpha(\phi)$ gives a direct measure of s from experimentally generated diffraction patterns as we shall show in the next section.

III. Experimental Results

Figure 2 shows the experimental setup used to generate the diffraction patterns. Light from a He-Ne laser is collimated so that the Bragg cell is illuminated at the Bragg angle. Lens L_2 produces the 2-D Fourier transform of the fully illuminated Bragg cell at plane P_2 . Figure 5 shows the resulting diffraction pattern for a PbMoO₄ cell driven by a single frequency at 400 MHz. The intensity $I(\alpha, \beta)$ follows the singularity function whose coordinates are given by Eq. (20). The intensity weighting in the β direction is $\text{sinc}^2(H\beta/\lambda)$, and the intensity weighting normal to the singularity function is $\text{sinc}^2(L\sigma/\lambda)$. An additional weighting in the horizontal direction is due to the Bragg angle mismatch conditions; it is not obvious unless the value of s is highly negative. At $\beta = 0$ the singularity function occurs at $\alpha = -\lambda/\Lambda$ relative to the focal point of the undiffracted light, where λ/Λ is twice the Bragg angle.



Fig. 5. Diffraction pattern for a fully illuminated lead molybdate Bragg cell driven at 400 MHz. Undiffracted light is attenuated by neutral density filter.



Fig. 6. Diffraction patterns for a tellurium dioxide Bragg cell driven at 500 and 300 MHz (double exposure).

Table I. Elastic Constants ($\times 10^{11}$ N/m²)

	PbMoO ₄ ¹⁷	TeO ₂ ¹⁸
c_{11}	1.092	0.532
c_{12}	0.683	0.486
c_{13}	0.528	0.212
c_{33}	0.917	1.085
c_{44}	0.267	0.244
c_{66}	0.337	0.552

Figure 6 is a photograph obtained by a double exposure of diffraction patterns for TeO₂ excited at 500 and 300 MHz. The features noted above are evident, as well as the fact that the location of $I(\alpha, \beta)$ is a function of Δ and that the singularity function becomes less highly curved as the acoustic drive frequency increases. In the limit of very high frequencies, or a large ratio of λ/Λ , the diffraction pattern more nearly approximates an orthogonal set of sinc^2 functions. From this figure we can also deduce that the TeO₂ cell produces a singularity function that opens more slowly than that for PbMoO₄. At 400 MHz, the acoustic wavelength is 9.1 μm for PbMoO₄ and 10.5 μm for TeO₂, which accounts for part of the decreased curvature. The remainder is due to different values for the relative changes in velocity. By measuring the locus for each singularity and by using Eq. (19), we find that $s = -0.168$ for PbMoO₄ and $s = 0.24$ for TeO₂. These values will now be compared with those obtained from the elastic constants. From Eq. (12) we note that

$$s = \frac{-(c_{13} + c_{33})(2c_{44} + c_{13} - c_{33})}{2c_{33}(c_{33} - c_{44})} \quad (22)$$

In Table I we give the values of the elastic coefficients for PbMoO₄ and TeO₂ from which we calculate that $s = -0.176$ for PbMoO₄ and $s = 0.274$ for TeO₂. Our measured data for s are in reasonable agreement with those calculated from Eq. (22), given the degree of accuracy in measuring the c_{ij} .¹⁹

We also tested a Bragg cell fabricated from fused quartz, which is isotropic, and found the singularity function to be a circle as predicted by Eq. (10) or (20). Since the rate at which the singularity function deviates from a straight line is proportional to $(1/2 - s)$, we find that the rate is lowest for TeO₂ and highest for PbMoO₄; the rate for fused quartz is nearly halfway between these two values.

The diffraction patterns produced by acousto-optic cells operated in the Bragg mode are similar to those obtained by Shaeffer and Bergmann²⁰ for cells operated in the Raman-Nath mode. In the examples they give, as well as those illustrated in Refs. 21 and 22, the diffraction patterns are symmetric about the focal point of the undiffracted light because drive frequencies are low. These patterns are also generally more complicated because both shear and longitudinal waves propagate within the cell.

The significance of the fact that the diffraction pattern for Bragg cells lies along a curved singularity function instead of a straight line depends on the application. The Fourier transform of signals introduced by Bragg cells is used extensively in spectrum analysis and in spatial filtering applications. In these applications the Bragg cell is often illuminated by a line source generated by inserting a cylindrical lens between L_1 and the Bragg cell (see Fig. 2) as well as between the Bragg cell and lens L_2 . In this fashion, a 1-D Fourier transform is generated with the line source being imaged in the orthogonal direction. In some configurations, however, it may not be possible to use a line illumination because two Bragg cells are used in series,²³ or they are used in a Rayleigh interferometer wherein a single lens is used to ensure that the Fourier transforms overlap. For such configurations we want to know the effect of integrating (detecting) light in the vertical direction.

In Fig. 7 we see the results of integrating $I(\alpha, \beta)$ in the β direction to the tenth zeros on either side of the horizontal axis. Since $\Delta\alpha$ as given by Eq. (21) gives the deviation of the singularity function from a straight line, we define a parameter $D = (1/2 - s)\lambda/\Lambda$; the integrated intensity is shown for D equal to 0, 1/16, 1/32, and 1/64. The result for $D = 0$ represents the integrated intensity of the diffraction pattern of a hypothetical self-collimating Bragg cell ($s = 1/2$) and forms a basis for comparing the results for other values of D . We compare the results for $D = 1/64$ with the ideal case, since it shows the greatest departure from the ideal. First, the sidelobes are asymmetric, being higher in the direction of the optical axis, and the nulls are less well formed. Second, the main lobe width is 3% wider and is shifted toward the optical axis by 4% of the main lobe width as

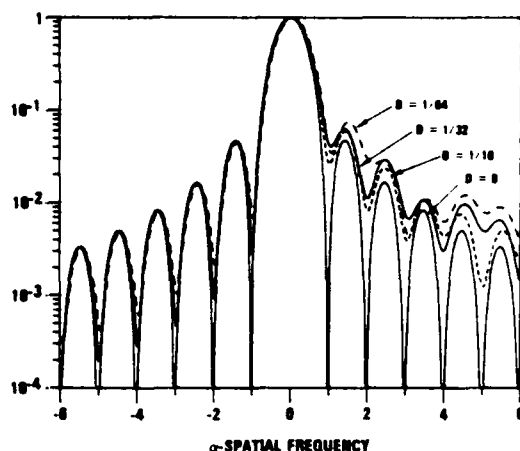


Fig. 7. Normalized intensity of diffraction pattern integrated in the vertical direction. The result for $D = 0$ is a $\text{sinc}^2(\alpha)$ function centered at $-\lambda/\Lambda$.

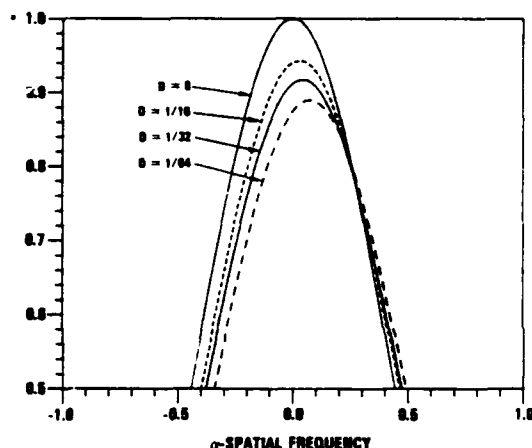


Fig. 8. Details of the intensity of the central lobe of diffraction pattern.

can be seen more clearly in Fig. 8. Third, the peak intensity is reduced by 13% because the diffraction pattern is highly curved toward the source. Note that the results for an isotropic material ($D \approx 1/16$) show a similar trend; the best results are obtained for an anisotropic material having a value of s as close to $1/2$ as possible.

In Fig. 9 we show the results when $I(\alpha, \beta)$ is integrated to the fifth zeros on either side of the horizontal axis. The same general features as described above are evident except that the degradation from the ideal is not as great. Experimental data obtained from a TeO_2 cell operating at 290 MHz (equivalent to $D = 1/32$) is also plotted in Fig. 9. Although the overall level of the sidelobes is higher for the experimental data due to scattered light, the general form of the data is in good agreement with the theory.

The best performance is obtained when we integrate only to the first zeros in the vertical direction. The results, shown in Fig. 10 for the sidelobes extending

toward the optical axis, suggest that the Fourier transform should be truncated at the first zeros by the detector to avoid an increase in the sidelobe levels. The penalty for truncation is a loss of $\sim 10\%$ of the available optical power.

IV. Bragg Cell Illumination

In some applications, the Bragg cell is illuminated by a line source generated by the use of a cylindrical lens arrangement as described in Sec. III. We now compare the effects of 1-D illumination with that of 2-D illumination on the diffraction pattern. In this case, the diffraction pattern is understood to exist in the horizontal direction, whereas the light distribution in the vertical direction is the image of the line source.

We use the same model for acoustic wave propagation as shown in Fig. 2. We now cannot account for the finite height of the transducer through a multiplication of the singularity function by $\text{sinc}(H\beta/\lambda)$ in the Fourier plane; instead we must calculate the effect of the finite

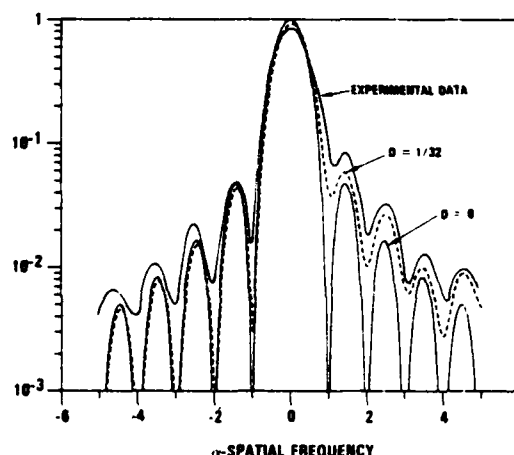


Fig. 9. Theoretical and experimental intensity of diffraction pattern for TeO_2 (290 MHz) integrated to the fifth zeros.

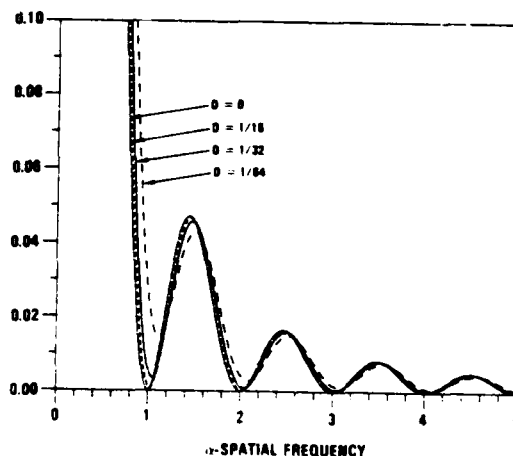


Fig. 10. Intensity of diffraction patterns when integrated in the vertical direction to only the first zero. Normalized so that the intensity is 1.0 at $\alpha = 0$ for $D = 0$.

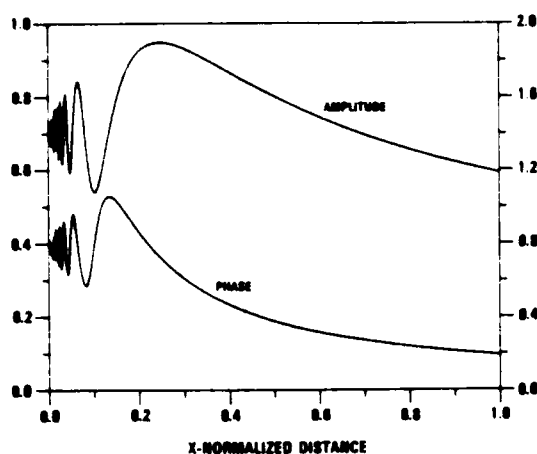


Fig. 11. Amplitude (left-hand scale) and phase (right-hand scale in radians) along the $y = 0$ axis due to the entire transducer.

transducer at the plane of the Bragg cell. The contribution from an elemental area of the transducer for the anisotropic case is obtained from Eq. (18):

$$a(x, y) = \frac{1}{\sqrt{j\Lambda x}} \exp \left\{ -j \frac{2\pi}{\Lambda} [x + y^2/2x(1 - 2s)] \right\} \exp(-\epsilon x).$$

We convolve this function with $\text{rect}(y/H)$ to obtain the total amplitude and phase function over the exit face of the Bragg cell. The convolution integral is then

$$a(x, y) = \int_{-H/2}^{H/2} \frac{1}{\sqrt{j\Lambda x}} \exp \left[-j \frac{\pi(y - u)^2}{\Lambda x(1 - 2s)} \right] \text{rect}(u/H) du, \quad (23)$$

where we have neglected the attenuation factor ϵ .

As before, we assume that the width of the transducer along the optical axis is large so that end effects are negligible. This assumption may seem to be less valid than before because the light is now focused within the cell. The transducer for the PbMoO_4 cell is $150 \mu\text{m}$ high and $600 \mu\text{m}$ wide. If a Gaussian beam is focused within the cell so that the beam waist height is $\approx 40 \mu\text{m}$, the beam waist does not grow by more than 4% at the entrance and exit faces of the cell.²⁴ The line illumination is, therefore, more nearly equivalent to a collimated beam than it is to a convergent or divergent beam.

The $\text{rect}(u/H)$ function in Eq. (23) can be removed by restricting the limits of integration to $|u| \leq H/2$ so that²⁵

$$a(x, y) = \frac{1}{2} [C[(1 - y)\sqrt{q/x}] + jS[(1 - y)\sqrt{q/x}] + C[(1 + y)\sqrt{q/x}] + jS[(1 + y)\sqrt{q/x}]], \quad (24)$$

where $C(\cdot)$ and $S(\cdot)$ are the Fresnel sine and cosine integrals, and $q = H^2/2\Lambda(1 - 2s)L$. The variables in Eq. (24) have been normalized so that $|y| \leq 1$ and $0 \leq x \leq 1$; this result shows that the amplitude transmittance along the Bragg cell at any value of y is a combination of Fresnel integrals. The amplitude and phase along the horizontal axis ($y = 0$) are shown in Fig. 11 for a PbMoO_4 Bragg cell driven at 400 MHz with $H = 150 \mu\text{m}$ and $L = 2.6 \text{ mm}$. Since the Fresnel integrals are functions of $\sqrt{1/x}$, both the amplitude and phase oscillate

rapidly at small values of x . The frequency of oscillation decreases as the distance from the transducer increases, and, for large values of x , the amplitude decays slowly. The maximum dip in the amplitude occurs at x_0 ; from Eq. (24) we find that this dip occurs when the argument of the Fresnel integral is ≈ 1.88 . Therefore, we find that

$$x_0 \approx \frac{H^2}{7\Lambda L(1 - 2s)}. \quad (25)$$

For an isotropic medium, this value of x_0 agrees reasonably well with that predicted by Ingenito and Cook⁹ who give a value of $x_0 = H^2/8\Lambda L$.

We now compute the Fourier transform of $a(x, y)$ to obtain the diffraction pattern in the horizontal direction. For convenience, we normalize the angular spatial frequency so that $\alpha_1 = (\alpha + \lambda/\Lambda)L/\lambda$:

$$F(\alpha_1, y) = \int_0^1 a(x, y) \exp(-j2\pi\alpha_1 x) dx. \quad (26)$$

The final step is to integrate the intensity of the Fourier transform over y to obtain the diffraction pattern that will be measured by a photodetector. Figure 12 shows the normalized magnitude squared of $F(\alpha_1)$ for PbMoO_4 as well as the diffraction pattern for the ideal case of a self-collimating material. We see that the central lobe is slightly broader due to a combination of the amplitude and phase weighting of $a(x, y)$. The entire diffraction pattern is shifted by a small amount; from Fig. 11 we see that the linear component of the phase over the region $0.2 \leq x \leq 1$ is $\approx 0.5 \text{ rad}$ so that the pattern should shift by nearly $\pi/10$ (i.e., $\sim 10\%$ of the angular distance between adjacent nulls). In comparing the results in Fig. 12 with those in Fig. 7, we see that the sidelobes toward the optical axis are lower, instead of higher, than those due to a uniformly illuminated aperture. The use of line illumination, therefore, causes the sidelobe levels to be more nearly equal to those produced by a uniformly illuminated aperture.

From Eq. (24) and Fig. 11, we see that the amplitude transmittance fluctuates rapidly in the region $x < x_0$.

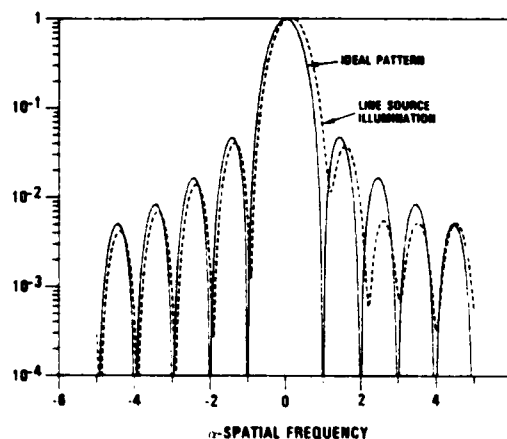


Fig. 12. Intensity of diffraction pattern when the Bragg cell is illuminated by a line source.

We might expect, therefore, that the Fourier transform would be more nearly ideal if we were to truncate the illumination so that this region does not contribute to the Fourier integral. We calculated the Fourier transform of $a(x,0)$ only over the range $x_0 \leq x \leq 1$ and noted some differences in the structure of the sidelobes extending toward the optical axis. The major change is in the value of the second sidelobe and the depth of the second null in the Fourier transform. As we increased the range of y over which we integrate at the Fourier plane, we found the differences to diminish so that truncation of the oscillating portion of $a(x,y)$ has less effect.

IV. Summary and Conclusions

The diffraction pattern of a uniformly illuminated Bragg cell lies along a singularity function that is determined by the phase velocity of the interaction material. For an isotropic material, this curve is a circle whose origin is at the focal point of the undiffracted beam and whose radius is twice the Bragg angle. For an anisotropic interaction medium we used Waterman's approximation to the phase velocity profile and found that the singularity function is a parabola having its vertex at twice the Bragg angle. Experimental measurements of s are in close agreement with those obtained from the elastic constants.

In signal processing applications where the Bragg cell must be uniformly illuminated, the curved singularity function causes the sidelobe levels in the direction of the source to increase when the diffraction pattern is integrated along a vertical line instead of along the locus of the curve. The severity of this problem can be reduced by restricting the region of integration in the vertical direction; the permissible region of integration is a function of λ , Λ , and s . Line illumination of the Bragg cell can be used to further reduce the deterioration of the diffraction pattern. Some residual aberrations still exist under these conditions, but their effects are small. A final technique for improving the diffraction pattern is to use an aperture stop to remove the contributions of rapid acoustic wave front oscillations near the transducer.

I thank A. M. Bardos, M. L. Shah, and G. S. Moore for stimulating technical discussions and G. H. Thaker and M. A. Epstein for assistance with the computer programs. Special thanks to S. J. Adhav for assistance in the experimental work. This activity was performed under a grant from the U.S. Army Research Office.

Appendix

From Eq. (18) we have that the effective amplitude distribution at the Bragg cell is

$$a(x,y) = \frac{1}{\sqrt{j\Lambda x}} \exp\left\{-j\frac{2\pi}{\Lambda} \left[x + y^2/2x(1-2s)\right]\right\} \exp(-\epsilon x),$$

and the region of integration is a wedge having its apex at $x = 0$ so that $0 \leq x \leq L$ and $|y| \leq \phi_0 x$, where ϕ_0 determines the upper and lower boundaries of the wedge. We first perform the integration on y :

$$G(x,\beta) = \int_{-\phi_0 x}^{\phi_0 x} \exp[-j2\pi y^2/2\Lambda x(1-2s)] \exp(-j2\pi\beta y/\lambda) dy,$$

which can be solved by using the relationship that²⁶

$$\int \exp(-ct^2 - 2dt) dt = \frac{1}{2} \sqrt{\frac{\pi}{c}} \exp(d^2/c) \times \operatorname{erf}(\sqrt{c}t + d/\sqrt{c}); c \neq 0.$$

If we make the associations and definitions that

$$\begin{aligned} c &= j\pi/\Lambda x(1-2s), \\ d &= j\pi\beta/\lambda, \\ e &= j\pi/\Lambda(1-2s), \end{aligned} \quad (A1)$$

we have that

$$\begin{aligned} G(x,\beta) &= \frac{1}{2} \sqrt{j\Lambda x} \exp(d^2/x/e) \\ &\times \left[\operatorname{erf}\left[(\phi_0\sqrt{e} + d/\sqrt{e})\sqrt{x}\right] - \operatorname{erf}\left[-(\phi_0\sqrt{e} + d/\sqrt{e})\sqrt{x}\right] \right]. \end{aligned} \quad (A2)$$

We now account for the finite transducer height H by multiplying $G(x,\beta)$ by $\operatorname{sinc}(H\beta/\lambda)$. The integration on x now becomes

$$\begin{aligned} A(\alpha,\beta) &= \frac{1}{2} \operatorname{sinc}(H\beta/\lambda) \int_0^L \operatorname{erf}\left[(\phi_0\sqrt{e} + d/\sqrt{e})\sqrt{x}\right] \\ &\times \exp[(d^2/e - \epsilon)x] \exp\left[-j\frac{2\pi}{\lambda}\left(\alpha + \frac{\lambda}{\Lambda}\right)x\right] dx \end{aligned} \quad (A3)$$

minus a similar integral in which ϕ_0 is replaced by $-\phi_0$. We can extend the upper limit to infinity if we multiply the integrand by $\operatorname{rect}(x/L - 1/2)$ and account for the finite limit through a convolution in α with $\operatorname{sinc}(L\alpha/\lambda)$. We now use the relationship that²⁶

$$\int_0^\infty \exp(-ft) \operatorname{erf}\sqrt{gt} dt = \frac{1}{f} \sqrt{\frac{g}{f+g}}; \operatorname{Re}(f+g) > 0. \quad (A4)$$

The presence of the attenuation factor ϵ ensures that $\operatorname{Re}(f+g) > 0$ so that Eq. (A4) is valid. We must exercise some care in applying Eq. (A4) in evaluating Eq. (A2) because the signs of the arguments of the error function change as a function of β . Consider the interval for which $|d/\sqrt{e}| \leq \phi_0\sqrt{e}$; from Eq. (A1) we find that this corresponds to $|\beta| \leq \phi_0\lambda/\Lambda(1-2s)$. For this range on β , the sign of the argument of the second error function in Eq. (A2) is negative, and we can use the relationship that $\operatorname{erf}(-t) = -\operatorname{erf}(t)$. We now make the associations that

$$\begin{aligned} f &= j\frac{2\pi}{\lambda}\left(\alpha + \frac{\lambda}{\Lambda}\right) - d^2/e + \epsilon, \\ \sqrt{g_1} &= \phi_0\sqrt{e} + d/\sqrt{e}, \\ \sqrt{g_2} &= \phi_0\sqrt{e} - d/\sqrt{e}, \end{aligned} \quad (A5)$$

where we use g_1 in Eq. (A3) and g_2 in the companion integral. We now have that

$$A(\alpha,\beta) = \frac{1}{2} \operatorname{sinc}(H\beta/\lambda) \left(\frac{1}{f} \sqrt{\frac{g_1}{f+g_1}} + \frac{1}{f} \sqrt{\frac{g_2}{f+g_2}} \right). \quad (A6)$$

As explained in the text, we expect $A(\alpha,\beta)$ to be a singularity function in α and β . Such a function is obtained in the limit as f tends toward zero. From Eqs. (A5) and (A1) we find that $f = 0$ yields

$$\beta^2 = \frac{\lambda(\alpha + \lambda/\Lambda)}{\Lambda(1/2 - s)} \quad (\text{A7})$$

in the limit as $\epsilon \rightarrow 0$. Letting $\epsilon \rightarrow 0$ is equivalent to the requirement that the acoustic attenuation be very small; in a practical sense, if ϵ is small over the aperture length L , use of the singularity function is valid. Equation (A6) now becomes

$$A(\alpha, \beta) = \frac{1}{2} \text{sinc}(H\beta/\lambda) \delta \left[\beta^2 - \frac{\lambda(\alpha + \lambda/\Lambda)}{\Lambda(1/2 - s)} \right], \quad (\text{A8})$$

which must be convolved with $\text{sinc}(L\alpha/\lambda)$ to account for the finite length of the Bragg cell. The resulting intensity of the Fourier diffraction pattern is then

$$I(\alpha, \beta) = \frac{1}{4} \text{sinc}^2 \left[\frac{L}{\lambda} f(\alpha, \beta) \right] \text{sinc}^2(H\beta/\lambda), \quad (\text{A9})$$

where $f(\alpha, \beta)$ is the argument of the δ function in Eq. (A8).

Equation (7) is an important result since it embodies many features of the diffraction pattern. First, it is the standard form of a parabola whose vertex is located at $\alpha = -\lambda/\Lambda$. The position of the vertex is inversely related to the acoustic wavelength and directly related to the acoustic frequency. Second, the ratio of λ/Λ is twice the Bragg angle; that is, at any acoustic frequency ω , the angular displacement of $I(\alpha, \beta)$ at $\beta = 0$ is at $2\theta_B$ with respect to the undiffracted light. If we had illuminated the cell at the Bragg angle with respect to the optical axis, which requires a factor $\exp(-j2\pi\theta_B x/\lambda)$ in the integrands of Eqs. (2) and (18) in the text, the undiffracted and diffracted light would propagate at angles of $\pm\theta_B$ with respect to the normal to the Bragg cell. Third, the *latus rectum* of the parabola is equal to $\lambda/\Lambda(1/2 - s)$; the value of s then determines the degree of curvature of the diffraction pattern in the vicinity of $\alpha = -\lambda/\Lambda$. Fourth, if $s = 0$, the crystal is isotropic so that the singularity equation becomes

$$\beta^2 = \frac{2\lambda}{\Lambda} (\alpha + \lambda/\Lambda), \quad (\text{A10})$$

which shows that the focus of the parabola is midway between the vertex and the axis defined by the undiffracted light.

References

1. Proc. IEEE 69 (Jan. 1981) contains papers relating to these subjects.
2. B. D. Cook, E. Cavanagh, and H. D. Dardy, IEEE Trans. Sonics Ultrason. SU27, 202 (1980).
3. A. Freedman, J. Acoust. Soc. Am. 32, 197 (1960).
4. R. F. Weeks, J. Acoust. Soc. Am. 33, 741 (1961).
5. E. P. Papadakis, J. Acoust. Soc. Am. 35, 490 (1963); 36, 414 (1964); 40, 863 (1966).
6. M. G. Cohen and E. I. Gordon, Bell Syst. Tech. J. 44, 693 (1965).
7. W. T. Maloney, G. Meltz, and R. L. Gravel, IEEE Trans. Sonics Ultrason. SU-15, 167 (1968).
8. M. G. Cohen, J. Appl. Phys. 35, 3821 (1967).
9. F. Ingenito and B. D. Cook, J. Acoust. Soc. Am. 45, 572 (1969).
10. G. N. Watson, *A Treatise on the Theory of Bessel Functions* (Cambridge U. P., London, 1966), p. 20.
11. Ref. 10, p. 385.
12. A. Papoulis, *Systems and Transforms with Applications to Optics* (McGraw-Hill, New York, 1968), p. 40.
13. M. Abramowitz and I. A. Stegun, *Handbook of Mathematical Functions* (Dover, New York, 1965), p. 556.
14. P. C. Waterman, Phys. Rev. 113, 1240 (1959).
15. B. A. Auld, *Acoustic Fields and Waves in Solids*, Vol. 1 (Wiley, New York, 1973), p. 227.
16. M. Born and E. Wolf, *Principles of Optics* (Macmillan, New York, 1964), p. 399.
17. G. A. Coquin, D. A. Pinnow, and A. W. Warner, J. Appl. Phys. 42, 2162 (1971).
18. N. Uchida and Y. Omachi, J. Appl. Phys. 40, 4692 (1969).
19. The elastic constants given by G. Arlt and H. Schweppe, Solid State Commun. 6, 783 (1968), differ from those in Ref. 18 by as much as 28%; the values given by Arlt and Schweppe (also in Ref. 18) yield $s = +0.193$ for TeO_2 .
20. L. Bergmann, *Ultrasonics and Their Scientific and Technical Applications* (Wiley, New York, 1939).
21. E. G. Spencer, P. V. Lenzo, and A. A. Ballman, Proc. IEEE 55, 2074 (1967).
22. Y. Ohmachi, N. Uchida, and N. Niizeki, J. Acoust. Soc. Am. 51, 164 (1972).
23. C. Atzeni and L. Pantani, Proc. IEEE 58, 501 (1970).
24. L. D. Dickson, Appl. Opt. 9, 1854 (1970).
25. Ref. 13, p. 304.
26. Ref. 13, p. 303.

APPENDIX C

MULTICHANNEL BRAGG CELLS: COMPENSATION FOR ACOUSTIC SPREADING

TO APPEAR IN APPLIED OPTICS

VOLUME 22, DECEMBER, 1983

MULTICHANNEL BRAGG CELLS: COMPENSATION FOR ACOUSTIC SPREADING

by

A. VanderLugt

G.S. Moore

S.S. Mathe

Harris Corporation
Government Systems Sector
P.O. Box 37
Melbourne, Florida 32901

ABSTRACT

In some applications, the performance of multichannel Bragg cells is compromised by the spreading of the acoustic waves as they propagate; the spreading causes the signals in the channels to overlap. The overlapping can be significantly reduced by a spatial filter in a Fourier/image plane the spatial filter is shown to be a cylindrical lens whose power is a function of the distance from the transducer. The effects of changes in the drive frequency as well as those of displacements of the filter are calculated. The reduction in the modulation transfer function as a function of propagation distance is calculated and some bounds on the time-bandwidth product and the number of channels are derived. In general, the overall performance can be improved by increasing the center frequency of the Bragg cell while keeping the bandwidth fixed.

1. INTRODUCTION

In some signal processing applications, multichannel Bragg cells are required to handle wideband parallel signals. One example is that of processing signals from a phased array antenna wherein we associate each channel of the Bragg cell with an antenna element. Multichannel Bragg cells were developed in the early 1960's by Lambert and his associates^{1,2}, and cells with as many as 128 channels have been described³. As the channels become more densely packed, the transducer heights are reduced causing the acoustic energy to spread over larger angles as it propagates through the interaction material. The acoustic waves from adjacent channels therefore overlap after a short propagation distance so that the utility of the device may be less than that desired.

Experiments with a 128-channel Bragg cell constructed from SF-8 dense flint glass and with a 32-channel device constructed from TeO₂, clearly show the acoustic spreading phenomena. In the high speed recording applications for which these devices were developed³, only the region near the transducer was used to modulate the light beam. We also noted, however, that even after the acoustic beams had overlapped completely, the diffracted light pattern could be separated into discrete channels to resemble the pattern produced near the transducer. This was accomplished by forming a Schlieren image at a plane displaced axially from that of the Bragg cell itself. This result, in turn, suggested that the acoustic spreading, in some sense, introduces the equivalent of a variable focusing power which is a linear function of the propagation distance. If this focusing action could be compensated so that, at some plane in an optical system, the diffracted light from each channel is confined to that channel, a more widely useful multichannel Bragg cell would result.

It is not sufficient, however, to confine the diffracted light to the channel without giving consideration to the impact that the compensation has on the modulation transfer function. As the acoustic energy propagates, the information diverges so that compensation causes it to be spread in the direction of propagation. The result is a loss in the modulation transfer function that is a function of the propagation distance. The desire to

confine the acoustic spreading must then be balanced by an acceptable loss in the modulation transfer function.

2. THEORY

The model that we use for analyzing the acoustic spreading is the same as that used before⁴ and is shown in Figure 1. An electrical signal drives a piezoelectric transducer having height H and an interaction width W . The transducer launches an acoustic wave within the Bragg cell which changes the index of refraction; this, in turn, causes the phase of light from a coherent source to be modulated in space and time. If the drive signal is an RF signal at frequency f_0 , the acoustic wavelength is $\Lambda_0 = V/f_0$, where V is the velocity of sound in the medium.

The acoustic wavefronts propagate in a fashion similar to optical wavefronts derived from a line source ($H \rightarrow 0$). If $W \gg H$, we can model the wavefronts as cylindrical sheets which, for an isotropic medium, spread at an angle $\pm\phi$ with respect to the x -axis. The degree to which acoustic spreading occurs is a function of the anisotropy of the medium, the acoustic wavelength and the transducer height.

The first step is to calculate the Fourier transform of a single channel Bragg cell driven as shown in Figure 1. We wish to derive the transform in the y -direction only, while we image the Bragg cell in the x -direction. We begin by considering the transducer to be a infinitesimal line source and account for its finite height by multiplying the Fourier transform by a sinc-function. The fourier integral to be solved is⁴

$$G(x, \beta) = \frac{1}{\sqrt{j\Lambda x}} \int_{-\phi_0 x}^{\phi_0 x} \exp[-j2\pi y^2/2\Lambda x(1-2s)] \exp(-j2\pi\beta y/\lambda) dy, \quad (1)$$

where β is the angular spatial frequency, s is a parameter that characterizes the degree of anisotropy as given by the elastic constants,^{4,5} Λ is the wavelength of the acoustic wave within the medium, and λ is the wavelength of light. The region of integration is over a wedge whose apex is

at $x = 0$ and θ_0 is the angle at which the acoustic beam has its first nulls; this region contains most of the optical energy. The far field value of ϕ_0 is ⁶

$$\phi_0 = \Lambda(1-2s)/H. \quad (2)$$

In reference 4, we solved (1) in terms of error functions having complex valued arguments. An equivalent result that is somewhat simpler to derive and provides more physical insight can be obtained through the use of Fresnel integrals. We let

$$c = \pi/\Lambda x(1-2s) \quad (3)$$

$$d = \pi\beta/\lambda$$

so that

$$G(x, \beta) = \frac{1}{\sqrt{j\Lambda x}} \int_{-\phi_0 x}^{\phi_0 x} \exp[-j(cy^2 + 2dy)] dy \quad (4)$$

By completing the square of the exponential and by changing variables, we obtain

$$G(x, \beta) = \frac{1}{\sqrt{j\Lambda x}} \exp(jd^2/c) \operatorname{sinc}(\beta H/\lambda) \int_a^b \exp(-ju^2) du, \quad (5)$$

where $a = -\phi_0 x \sqrt{c} + d/\sqrt{c}$, $b = \phi_0 x \sqrt{c} + d/\sqrt{c}$, and $\operatorname{sinc}(\beta H/\lambda)$ is the multiplicative factor needed to account for the finite height of the transducer. The integral is a Fresnel integral that further modifies the amplitude of $G(x, \beta)$. Depending on the values of the limits, this function may be nearly rectangular (similar to the near field diffraction pattern of a slit) or nearly a sinc-function (similar to the far field diffraction pattern of a slit). In all cases, the most rapid change in the value of the Fresnel integral occurs at those values of β where either the upper or the lower limit is equal to zero. By using (3), we find that the Fresnel "window" has a nearly uniform value for

$$|\beta| \leq \phi_0 \lambda / \Lambda(1-2s). \quad (6)$$

We substitute (2) into (6) and find that the Fresnel integral has a nearly uniform value for

$$|\beta| \leq \lambda/H, \quad (7)$$

which is the same as the region occupied by the central lobe of the $\text{sinc}(\beta H/\lambda)$ weighting due to the finite transducer height. The Fresnel integral, then, has the effect of suppressing the sidelobes of the $\text{sinc}(\beta H/\lambda)$ function as well as producing some low modulation fringes in the central lobe. At small values of x , the Fresnel integral transitions into a broad Fraunhofer diffraction pattern of a narrow slit and has very little impact on the amplitude of $G(x, \beta)$.

If we denote the total amplitude weighting of $G(x, \beta)$ by $f(x, \beta)$, we have that

$$G(x, \beta) = f(x, \beta) \exp[j\pi x \Lambda (1-2s) \beta^2 / \lambda^2]. \quad (8)$$

We now concentrate on the phase part of $G(x, \beta)$. The key point is that the phase factor is quadratic in β and linear in x . At the transducer, where $x = 0$, there is no optical power, whereas the optical power is greatest at $x = L$. If the optical power could be canceled, the inverse Fourier transform would confine the light to rectangular channels with no spreading into adjacent channels. In principle, the optical power can be compensated by a section of a conical lens whose power varies linearly from zero, at $x = 0$, to a value of $L\Lambda(1-2s)/\lambda^2$ at $x = L$. An alternative method is to construct a holographic correcting element from one channel of the Bragg cell; such an element will then correct the acoustic spreading for all channels simultaneously in the same fashion as would a matched filter.

The use of a holographic element for compensating the acoustic spreading has been reported by Vodovatov, *et al.*⁷. The derivation given there for the value of $G(x, \beta)$ does not agree with (8), particularly with respect to the phase factor having quadratic dependence on β and linear dependence on x . The result from (8), however, is consistent with the observation that the channels can be separated by focusing at a different

plane using auxiliary optics. As an aside, it is easy to show that the axial distance from the Bragg cell at which the channels become separated is equal to $x(1-2s)\Lambda/\lambda$. Thus, the "focal line" has a slope of $(1-2s)\Lambda/\lambda$ with respect to the horizontal axis; for typical Bragg cell parameters, this slope corresponds to an angle of 88° to 89° which is nearly parallel to the optical axis.

We now consider some details relating to the construction of a holographic correcting element based on the result given by (8). This analysis provides some useful insights into the performance relationships of multi-channel Bragg cells. We construct the element by using a line reference source, as shown in Figure 2, that lies horizontally in the plane of the Bragg cell and is displaced vertically by a distance D . The line source is produced by a cylindrical lens that collects part of the same collimated beam that illuminates the Bragg cell. A spherical-cylindrical lens combination then creates a Fourier transform in the vertical direction and an image in the horizontal direction. The figure also shows a second Fourier/imaging lens combination that will be used later to create a corrected image of the Bragg cell at the output plane. The reference beam is modulated by a device (not shown) so that it has the same temporal frequency as the light diffracted by the Bragg cell. The total light distribution in the Fourier plane is then

$$A(x,\beta) = R e^{j2\pi\beta D/\lambda} + G(x,\beta), \quad (9)$$

where R is the amplitude of the reference beam. This light distribution is square-law recorded on a photographic plate and the developed plate is replaced in the system. If we select the appropriate diffracted order at the output plane, the effective holographic transmittance function is

$$H(x,\beta) = R G^*(x,\beta) \exp[j2\pi\beta D/\lambda]. \quad (10)$$

The action of the holographic element is to correct, or conjugate, the cylindrical phase factor contained in $G(x,\beta)$. We see from (8) that if the holographic element is constructed at an acoustic wavelength Λ_0 , there will be some residual aberrations as the drive frequency changes to produce a

different acoustic wavelength Λ . We now examine the nature of this error as well as the effects of positioning errors of the hologram.

To simplify the notation, let $a = \pi(1-2s)\Lambda/\lambda^2$ and we ignore any amplitude weighting terms as well as the linear exponential phase factor that merely causes an overall vertical displacement of the corrected image. Suppose that the holographic filter was made at an acoustic wavelength Λ_0 . If the operational wavelength is at some other value, aberrations will arise whose phase is proportional to $\exp[ja\beta^2x - j(a+a_0)\beta^2x]$, where a_0 is due to the value of $\Lambda - \Lambda_0$. We can also determine the effects of displacement of the filter in the β and x directions so that the residual phase error $\theta(x, \beta)$ becomes

$$\theta(x, \beta) = a\beta^2x - (a+a_0)(\beta+\beta_0)^2(x+x_0), \quad (11)$$

where β_0 and x_0 are the positional errors. Note that the principal terms in $a\beta^2x$ cancel so that, if we arrange the terms in descending powers of β , we have that

$$\begin{aligned} \theta(x, \beta) = & a_0\beta^2 + a\beta^2x_0 + a_0\beta^2x_0 \\ & + 2(a+a_0)\beta_0\beta x + 2(a+a_0)\beta_0\beta x_0 \\ & + (a+a_0)\beta_0^2x + (a+a_0)\beta_0^2x_0. \end{aligned} \quad (12)$$

The first three terms of (12) are residual errors in correcting the cylindrical phase factor and lead to a defocusing of the output; the next two terms are linear in β , leading to a slight vertical displacement of the output; the last two terms are not functions of β but one of them is linear in x which can produce a horizontal shift in the output. These terms provide a convenient diagnostic tool for properly aligning the filter. Suppose that after the filter is placed in the system, we illuminate it with the channel driven at the same constructional acoustic wavelength. In this case, $a_0 = 0$ and the residual terms are

$$\begin{aligned}
\theta(x, \beta) \big|_{a_0=0} &= a\beta^2 x_0 \\
&+ 2a\beta_0 \beta x + 2a\beta_0 \beta x_0 \\
&+ a\beta^2 x + a\beta^2 x_0.
\end{aligned} \tag{13}$$

Since the effects of the first term (defocusing) may be difficult to detect, we first observe the point in the output for which $x = 0$. The two key terms remaining are $2a\beta_0 \beta x_0$ and $a\beta^2 x_0$. The first of these two terms will cause the output to shift up or down depending on the signs of β_0 and x_0 . Set $x_0 = 0$ by noting when the output is symmetrically positioned about the image of the reference beam; the remaining terms are $2a\beta_0 \beta x$ and $a\beta^2 x$. If we now focus at $x = L$ to get maximum sensitivity, we can set a $\beta_0 = 0$ by again causing symmetry in the vertical direction about the reference beam.

Since the filter is now properly positioned, all the error terms from (13) are equal to zero so that we can now examine the effects of a wavelength change ($a_0 \neq 0$). The only remaining term is then $\theta(x, \beta) = \exp[ja_0 \beta^2 x]$, a defocusing term which shows the degree to which the acoustic spreading has not been compensated. At $x = 0$, we see that this term has no effect on the output, whereas at $x = L$ the phase is bounded by $\pm a_0 \beta^2 L$. This suggests that we might be able to balance the aberration so that it has equal but opposite values at $x = 0$ and $x = L$. This can be done by focusing the reference beam at that plane, axially displaced from the Bragg cell, where the self-focusing property of the diffracted light causes the channels to be fully separated. If we let x_1 be the corresponding horizontal distance at which the two beams are jointly focused, the residual phase, for $\beta_0 = x_0 = 0$, is given by

$$\theta(x, \beta) = -a\beta^2 x_1 + a_0 \beta^2 x. \tag{14}$$

This procedure, in effect, provides a focusing bias term which offsets the bias in x (i.e., x is bounded by the range 0 to L). To balance the aberrations at the ends of the cell, we find that $x_1 = (a_0/a)L/2$, so that

$$\theta(x, \beta) = \pm a_0 \beta^2 (x-L/2) \quad (15)$$

and the aberrations are properly balanced.

We now consider the optimum value of the acoustic wavelength to be used in constructing the holographic element. A Bragg cell is generally specified by its center frequency f_0 and a bandwidth Δf . If $f_1 = f_0 - \Delta f/2$ and $f_2 = f_0 + \Delta f/2$, the Bragg cell is operated so that $f_2 \leq 2f_1$ to prevent intermodulation products. Since Λ is inversely proportional to f , constructing the holographic filter at the center frequency does not equally divide the wavelength range. Instead, we construct the hologram so that

$$\Lambda_0 = V(f_2 + f_1)/2f_2f_1 \quad (16)$$

This wavelength choice shows that the hologram tends to favor correction of the aberrations at the lower drive frequencies where the acoustic spreading is greatest.

We now compare the corrected wavefront aberration with the uncorrected wavefront. Without the holographic element, we have a maximum phase error equal to $(a + a_0)\beta^2 L$, whereas the maximum error with correction is $\pm a_0 \beta^2 L$. The ratio of $|a_0|/(a + a_0)$ is equal to $(1 - f_1/f_2)/2$; for the worst case of an octave bandwidth, the ratio is 1/4. Therefore, the maximum phase error with correction is at least four times less than the worst case (at f_1) without correction, and at least two times better than the best case (at f_2) without correction. If the holographic element is constructed to balance the aberrations along the cell, the corrected wavefront is yet another factor of two better than the uncorrected case.

3. EXPERIMENTS

We constructed a holographic element from one channel of a 32-channel Bragg cell. This cell has a nominal bandwidth $\Delta f = 80$ MHz at a center frequency $f_0 = 135$ MHz. The cell is fabricated from tellurium dioxide material having a longitudinal velocity of 4.2 Km/sec. The active length of

the crystal is $L = 6$ mm so that the time delay is ~ 1.5 μ sec and the time-bandwidth product is ~ 120 . The transducers have heights equal to 100 μ and they are placed on 250 μ center spacings. The acoustic wavelength at the center frequency is 31 μ . This Bragg cell was originally designed and successfully used as a high-speed, multi-channel light modulator wherein only the region near the transducer was used.³ Since this cell produces a considerable amount of acoustic spreading, it represents a severe test of the ability of a holographic element to channelize the light over a significant amount of the horizontal aperture.

The light source is a 10 mw He-Ne laser for which $\lambda = 632.8$ nm. The holographic elements were constructed on SO-120 glass plates with a reference-to-signal beam ratio of unity near $\beta = 0$. After the plate was developed and replaced in the system, we positioned it by using the procedure outlined above to set β_0 and x_0 equal to zero. This was achieved by driving only the channel used to construct the hologram (see Figure 2), while observing the corrected image of the Bragg cell at the output plane.

Figure 3 shows the uncorrected and the corrected output when channels are driven at the frequency corresponding to Λ_0 . Figure 3a shows the degree of acoustic spreading for the uncorrected case. Of the twelve channels available, we drove the top channel to illustrate how rapidly the acoustic energy spreads and the bottom four channels to illustrate how the beams overlap and add coherently. We see that the beams are well separated only in the region near the transducer as noted earlier. If we wish to process a significant amount of time history, we find that the beams begin to overlap at a position that is only 10% of the available aperture. Figure 3b shows the corrected output; we see that there is very little evidence of beam spreading and that the light has been confined to within channel heights as determined by the transducers. The amount of beam spreading is a function of the drive frequency; it is greatest at the low frequency band edge (due to a large Λ) and least at the high frequency band edge (where Λ is small). Furthermore, as shown by (12), the output is fully corrected only when $a_0 = \beta_0 = x_0 = 0$. If $\beta_0 = x_0 = 0$, the residual aberration is $\theta(x, \beta) = \pm a_0 \beta^2 x$, so that if we drive the Bragg cell at its lowest and highest frequencies, we can see the effects of the residual aberrations.

Figures 4a and 4b show the corrected output at the low and high drive frequencies. We see no appreciable change in the spreading due to the residual aberration as a function of drive frequency except at the lowest frequency. This was confirmed visually by sweeping the drive oscillator over the frequency band and noting very little change in the channel height which is most evident at $x = L$. The reason can be seen from the following arguments. The value of ϕ_0 is given by (2) so that at $x = L$, the acoustic beam extends a distance h above and below the center line of the channel:

$$h = \Lambda(1-2s)L/2H \quad (17)$$

For the parameters of the TeO_2 Bragg cell ($s = 0.2$), we have that $h = 558\mu$ so that the main beam spreads through the adjacent channel and nearly to the center of the third channel away. This behavior is consistent with the results shown in Figure 3a. At the lowest frequency, the spreading at the end of the cell increases to 792μ , whereas at the highest frequency the spreading decreases to 432μ . The holographic element corrects the spreading completely at the midband frequency; at the high and low frequencies the spreading is that produced by an equivalent acoustic wavelength $\Lambda_0 = V[(f_2 - f_1)/2f_1 f_2]$. When this value of wavelength is used in (17) the worst case spreading is reduced to 182μ . This degree of spreading extends approximately to the center line between transducers and is apparent only at the end of the Bragg cell remote from the transducer. If the correction were made so that the spreading is balanced at both $x = 0$ and $x = L$, the spreading would be further reduced by a factor of two.

4. THE MODULATION TRANSFER FUNCTION

We see, then, that the holographic element confines the diffracted light waves to channels as defined by the transducer height. The next issue is to determine the effect that this correction has on the modulation transfer function of the Bragg cell. We can estimate the degree of modulation transfer loss as a function of the propagation distance by considering the Poynting vector surface as a function of x . The acoustic energy propagating at an angle ϕ with respect to the x -axis (see Figure 5) travels at a velocity

$$V_{\phi} = V[1 - s\phi^2/(1-2s)]. \quad (18)$$

Suppose that we were to drive the Bragg cell with an impulse function and observe the surface defining the acoustic energy at some time t . The acoustic energy will occupy a finite pulse width, centered on the curved line shown in Figure 5, consistent with the reciprocal bandwidth of the Bragg cell. The energy along the axis will have traveled a distance $x_2 = Vt$ whereas the energy at an angle ϕ will have traveled a distance $V_{\phi}t$. The horizontal projection of this distance is $x_1 = V_{\phi}t \cos\phi$:

$$x_1 = Vt[1 - \phi^2/2(1-2s)], \quad (19)$$

and the difference between x_2 and x_1 is

$$d_1 = Vt\phi^2/2(1-2s). \quad (20)$$

If we use (2) in (20), we have

$$d_1 = x\Lambda^2(1-2s)/2H^2. \quad (21)$$

The effect of imaging the Bragg cell in the horizontal direction while correcting for spreading in the vertical direction is to integrate the energy function in the vertical direction. We now need to form a basis for a reasonable estimate for the resulting pulse width.

The 3-dB bandwidth of the cell is Δf so that, if there were no acoustic spreading, the equivalent rectangular pulse width⁸ would be $T_0 = 1/\Delta f = d_0/V$. This result is obtained by representing the MTF by $\text{sinc}[d_0(f-f_c)/V]$ where f_c is the center frequency. The effect of integration in the vertical direction due to compensating the acoustic spreading is approximately $d_1/30$, obtained by numerical integration. The equivalent rectangular pulse width d_2 after correction is then $d_0 + d_1/30$

$$d_2 = \frac{V}{\Delta F} + \frac{x\Lambda^2(1-2s)}{60H^2} \quad (22)$$

The argument of the sinc-function representing the corrected MTF is then $Z = d_s(f-f_c)/V$ or

$$Z = \frac{(f-f_c)}{\Delta f} \left[1 + \frac{x' \Lambda^2 (1-2s) N}{60H^2} \right], \quad (23)$$

where $N = \Delta f T = T/T_0$ is the time bandwidth product of the Bragg cell and $x' = x/L$ is a normalized distance. For $x' = 0$, there is no loss in MTF; at $x' = 1$, there may be some loss in the MTF. For the parameters of the Bragg cell used in these experiments, the MTF is reduced by 0.8 dB at $x'=1$ and by 0.4 dB at $x'=1/2$.

We now calculate the number of channels that can be used, subject to the restriction that the main lobes of the far-field acoustic waves do not overlap. If the Bragg cell crystal is square, we have that $L = (N_c - 1)kH + H = N_c kH$, where N_c is the number of channels and kH is the separation between transducers. The condition for avoiding overlap is to require that h , as given by (17), be less than or equal to $kH/2$ as shown in Figure 5. By combining these relationships, we have that

$$N_c \leq H/\Lambda_1(1-2s), \quad (24)$$

where $\Lambda_1 = V/f_1$ is the worst case wavelength. For the corrected case, we substitute the equivalent value of the acoustic wavelength which is

$$\Lambda_c = V\Delta f/2f_1f_2, \quad (25)$$

so that

$$N_c \leq \frac{2f_1f_2H}{V\Delta f(1-2s)}. \quad (26)$$

The increase in the number of usable channels is then $\Lambda_1/\Lambda_c = 2f_2/\Delta f$, provided that N_c is not greater than L/H . Since the minimum value of the transducer height may be set by other considerations, the value of N_c as given by (26) may not be achievable. For the parameters of the Bragg cell we used, the maximum value of N_c without correction is about 4; with

correction, N_c is about 17. To achieve the full utility of the device, it is necessary to correct the spreading so that (15) is satisfied; in that case N_c is equal to 34. Equation (26) then indicates how closely packed the channels can be without the residual aberrations causing the light to interact, while (23) indicates the loss in modulation transfer function. Experimental results confirm the analysis that the acoustic spreading can be successfully corrected without introducing an excessive loss in the MTF. We modulated the carrier with a 12.5 MHz square wave and measured the increase in the equivalent pulse width at the midpoint and at the two ends of the cell. The results were consistent with those predicted by the MTF as given by (23).

5. Summary and Conclusions

We have shown that the effects of acoustic spreading within the Bragg cell can be compensated in the sense that the diffracted light can be more nearly contained within channels as defined by the transducers. The results show that the best performance, both in terms of correcting for the acoustic spreading and limiting the loss in MTF, is obtained when we use a Bragg cell interaction medium that has a large value of s . A value of s approaching $1/2$ implies that the acoustic spreading is intrinsically small; such materials may not, however, have the characteristics required to achieve large bandwidths, high diffraction efficiencies or low attenuation per unit length. For a given interaction medium, the results show that the performance improves as the fractional bandwidth decreases. The correction for acoustic spreading can also be improved by a factor of two if the correction is optimized at the midpoint of the cell; this optimization does not, in general, affect the MTF.

The degree of correction required is application dependent. If each channel is driven by an independent wideband signal plus noise and we wish to correlate these signals with a reference signal in a time-integrating architecture, a high degree of correction is required. The reason is that we do not want the information in any one channel to spread into adjacent channels; there are other applications where the Bragg cell is used as a two-dimensional light modulator that also require a high degree of correction. In applications such as processing bistatic or monostatic radar

returns using a phased array antenna, the data in adjacent channels due to adjacent antenna elements generally does not change rapidly. Nevertheless, in high performance radars, where the return pulse must be processed through correlation, the performance may be improved by optically correcting for the acoustic spreading.

In both of the general applications cited above, a correlation operation is performed on the received time signal in a space-plane implementation. An alternative way to perform correlation is through frequency plane multiplication techniques wherein we create the two-dimensional Fourier transform of the multichannel Bragg cell and multiply it by the Fourier transform of the reference signal. If, for example, the reference function is time-invariant, the constructed matched filter will automatically incorporate the holographic correcting element that we have implemented. In many cases, however, the reference function must be programmable (i.e., it is time-variant) so that the multiplication technique is less attractive when applied to multichannel Bragg cells.

The notion of frequency plane processing also suggests applications such as emitter sorting. In this case, the two dimensional Fourier transform of the multichannel Bragg cell produces an optical mapping of the microwave field. The frequency of a particular emitter is displayed along a frequency axis while the azimuth (or direction of arrival) is displayed along an azimuth axis. Results obtained without the use of the holographic correcting element show that the diffraction pattern is not an exactly orthogonal sinc-function; in the vertical direction the sinc-function follows the locus of a parabola having its foci at the optical axis.⁴ If the holographic correction element is used, the parabola becomes a straight line. Since the azimuth information does not map directly into the rectangular coordinates of the Fourier plane (i.e., the vertical displacement is proportional to $\sin \psi$), some post processing of a photodetector array output is needed to properly remap the azimuth information. This remapping could also include any geometric scaling needed to compensate for the effects of acoustic spreading.

The use of a holographic corrector plate for the acoustic spreading, as well as a broader understanding of the basic diffraction patterns, opens the way for new application of multichannel Bragg cells. As the bandwidths of communication and collection systems increase, the need for such devices will expand because they help utilize the full parallel processing capabilities of optical systems.

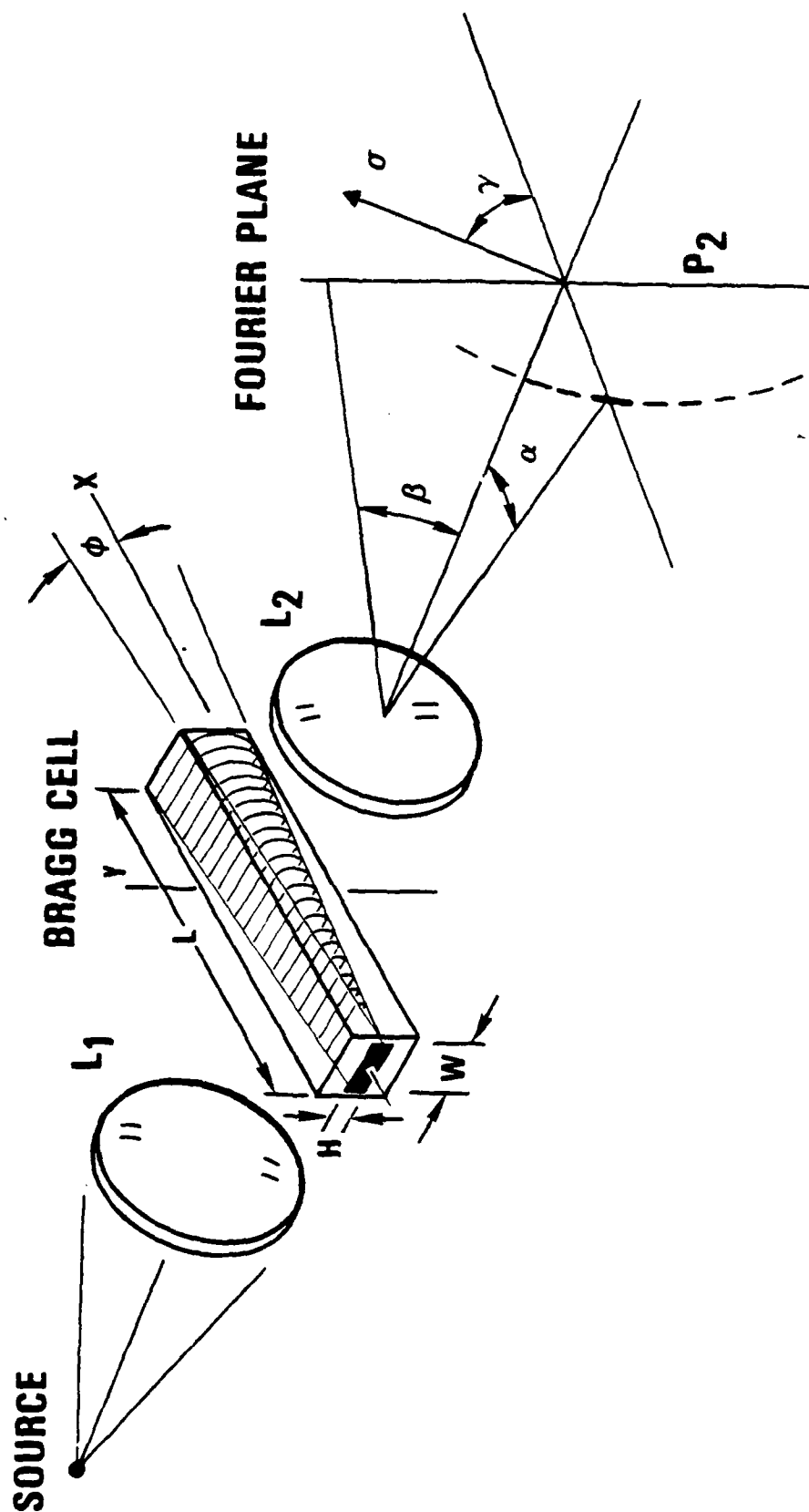
This work was supported by the U.S. Army Research Office.

REFERENCES

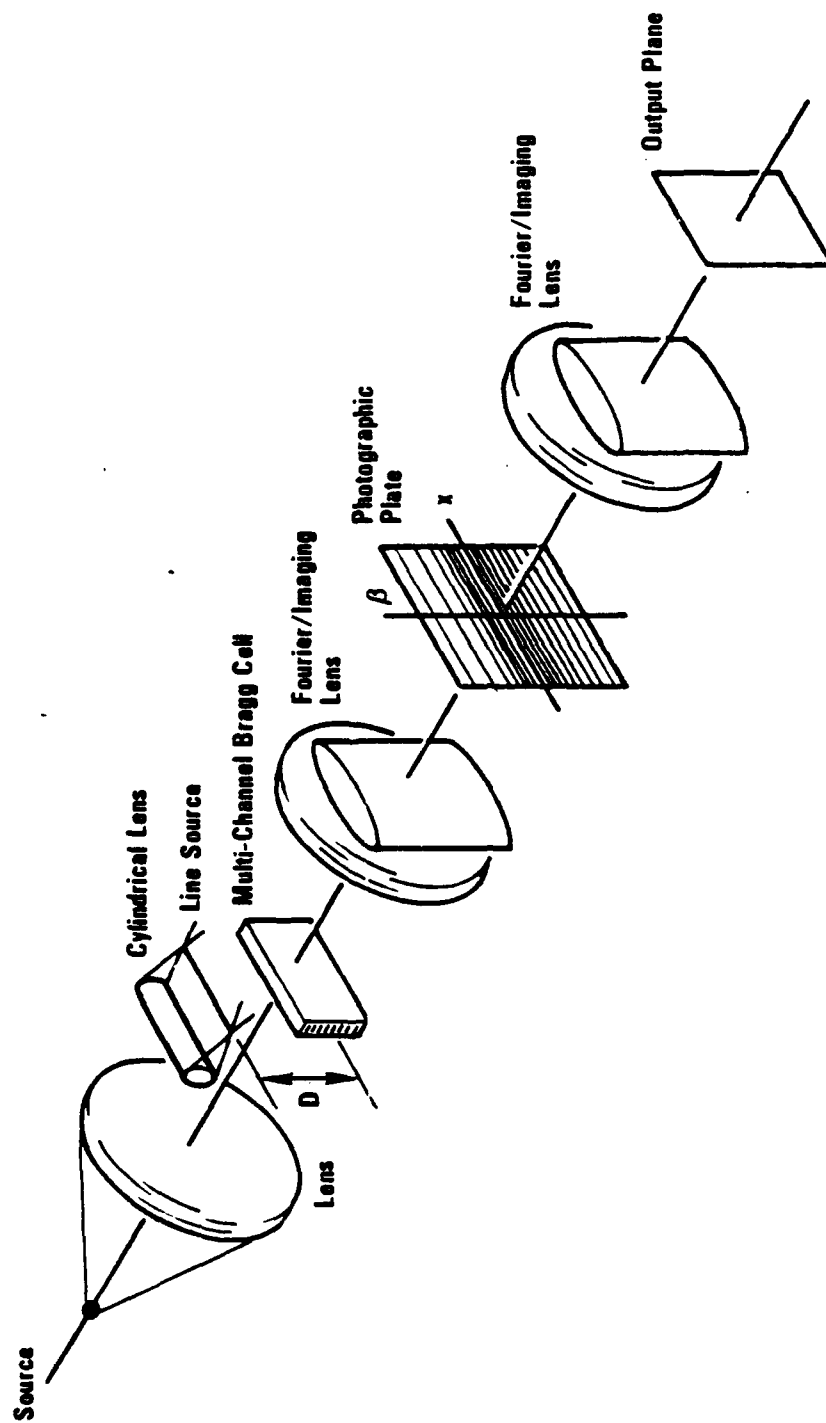
1. L.B. Lambert, IRE Nato Conv. Record, Vol. 10, Part 6 (1962)
2. L.B. Lambert, M. Arm and A. Aime, "Optical and Electro-Optical Information Processing," Ed. J.T. Tippet, et al, MIT Press, 1965.
3. A.M. Bardos, Appl. Opt., Vol. 13, p. 832 (1974).
4. A. VanderLugt, Appl. Opt., Vol. 21, p. 1092 (1982).
5. P.C. Waterman, Phys. Rev., Vol. 113, p. 1240 (1959).
6. M.G. Cohen, J. Appl. Phys., Vol. 35, p. 3821 (1967).
7. I.A. Vodovotov, N.A. Esepkina, V. Yu Petrun'kin, and S.A. Rogov, Pis'ma Zh. Tekh. Fiz, Vol. 7, p. 369 (1981). Appears in the American Institute of Physics translation of Sov. Tech. Phys. Lett. 7(3), 1981, page 159.
8. J.B. Thomas, Statistical Communication Theory, John Wiley and Sons, N.Y., 1969, p. 388.

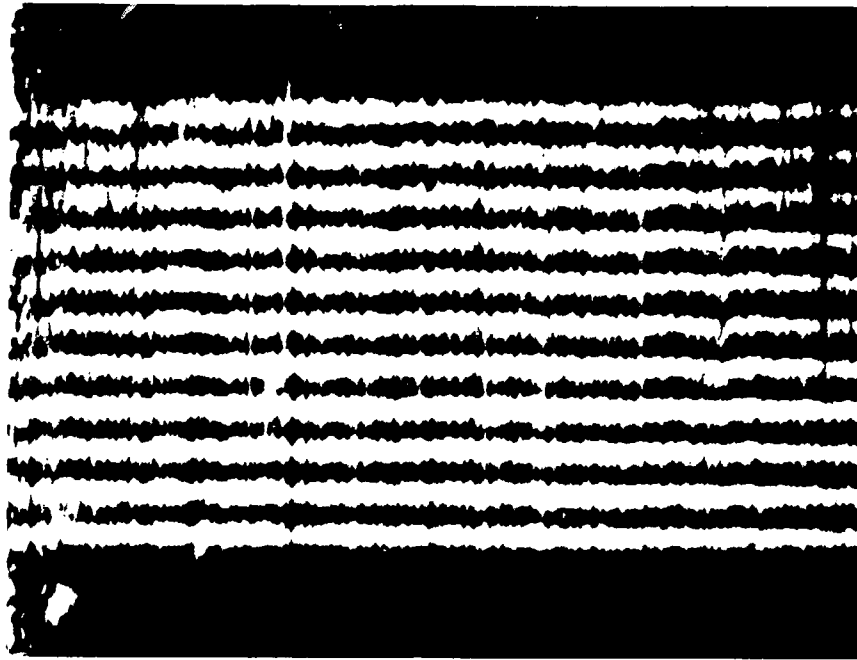
FIGURE CAPTION LIST

- FIGURE 1. Model for Acoustic Spreading in a Bragg Cell.
- FIGURE 2. Optical System for Constructing the Holographic Element and Correcting the Acoustic Spreading.
- FIGURE 3. Multichannel Bragg Cell Diffraction Beams: (a) Uncorrected Case Showing Beam Overlap; (b) Corrected Beams at Optimum Acoustic Wavelength (123 MHz).
- FIGURE 4. Corrected Beams Showing Energy Confinement: (a) Result for 175 MHz; (b) Result for 95 MHz.
- FIGURE 5. Diagram Showing the Surface of Acoustic Energy and the Transducer Geometry.

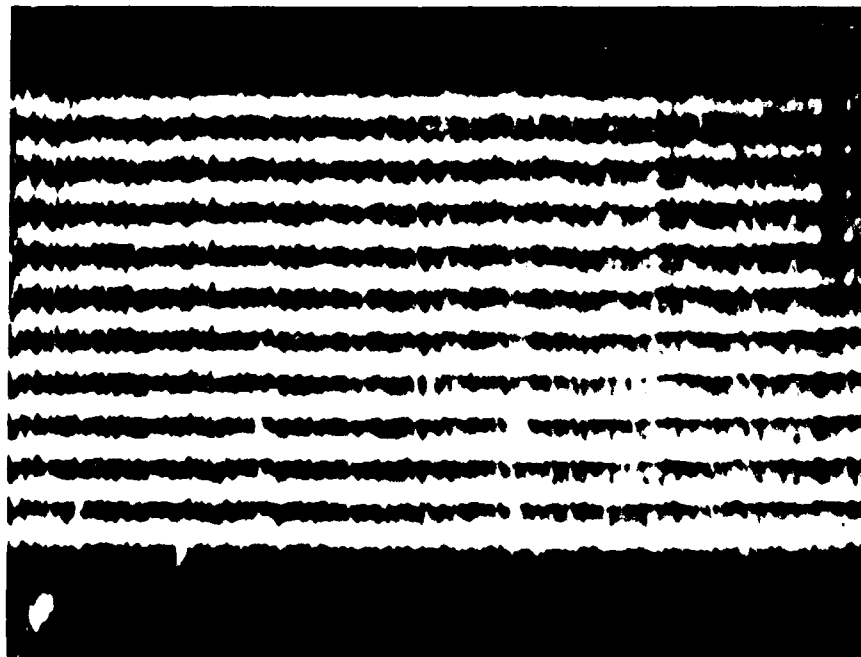


12417-1





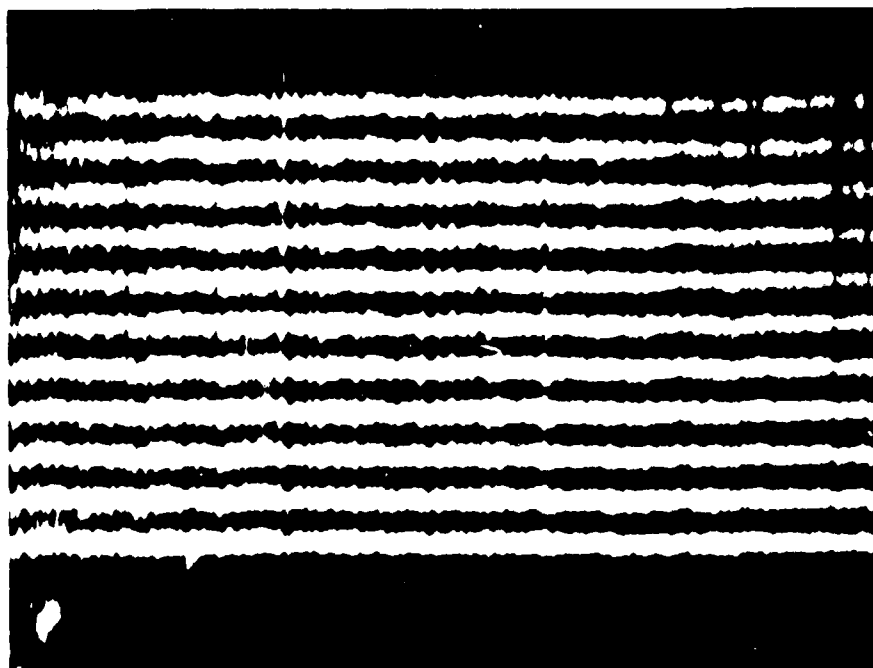
(a)



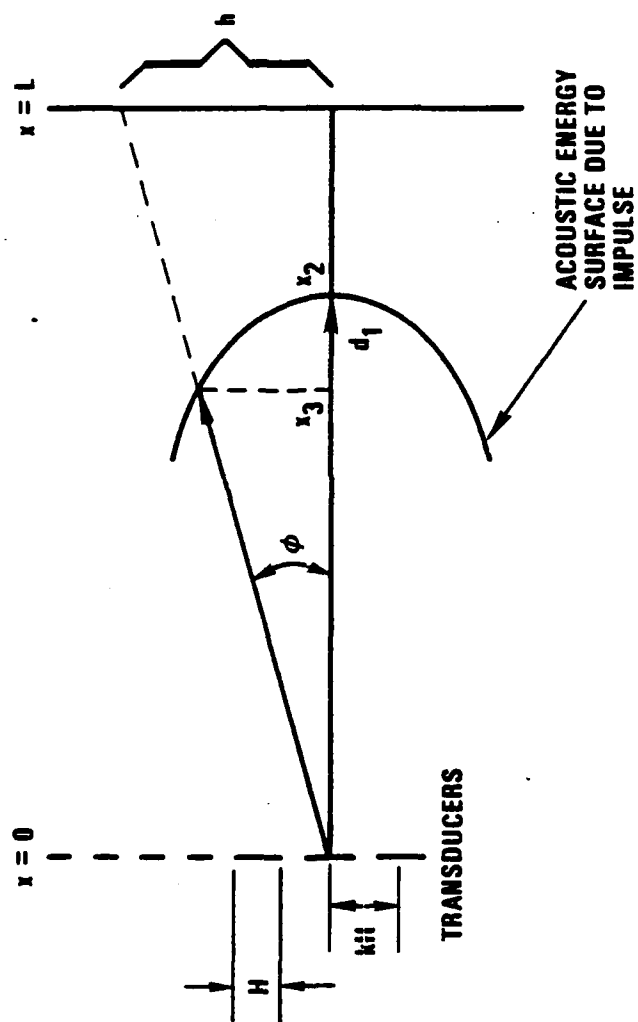
(b)



(a)



(b)



APPENDIX D

ADAPTIVE OPTICAL PROCESSOR

REPRINTED FROM APPLIED OPTICS

VOLUME 21, PAGE 4025, NOVEMBER, 1982

Adaptive optical processor

A. Vander Lugt

The transversal filter is widely used in digital data processing. In this paper, we describe a method for using optically tapped, Bragg cell delay lines to implement a general adaptive linear prediction algorithm. Flexibility is achieved through changing the electronic signals. The implementation is in the Fourier domain so that the wide bandwidth of the Bragg cells can be fully used. A high dynamic range can be achieved because the system is interferometric and linear in light amplitude.

I. Introduction

In this paper we describe an adaptive optical processing technique wherein the processing operation is performed in the frequency domain. Adaptive filtering as implemented by linear prediction has been applied in several areas. A tutorial review of linear prediction has been given by Makhoul¹ and a survey of its application to communications, including adaptive techniques, was given by Lucky.² The early work by Lucky was on adaptive redundancy removal in data³ and adaptive equalization of digital communications systems^{4,5} to increase the rate of data transmission. Variations of these adaptive schemes, in which the system is equalized either by transmitting a training set or by operating on the data itself (decision directed), have been reported.⁶⁻⁸ Adaptive equalization significantly increases the allowable data rate over a filtered channel for a given bit error rate required at the output of a receiver.

Adaptive filtering has also been applied to antenna sidelobe weighting by Widrow *et al.*⁹ and others.^{10,11} Widrow *et al.*¹² have also described adaptive noise-cancellation techniques such as notch filtering for interference rejection, adaptive self-tuning for spectral line enhancement, and spectral analysis. Griffiths, in particular, has addressed the problem of estimating the instantaneous frequency contained in digital signals.¹³ The same basic algorithms are finding widespread application in speech processing¹⁴⁻¹⁶ and in combating intersymbol interference.^{4-8,17}

The wide range of applications of adaptive filtering is due partly to the flexibility of the transversal filter that is a basic element of all these schemes. A transversal filter consists of a tapped delay line that contains the discrete time-sampled values of a received signal. The outputs of each tap are weighted as determined by the processing operation and summed to provide an estimate of the signal. If the weights are selected to provide the best estimate of the received signal, the system is called a linear predictor or estimator. If the estimated signal is subtracted from the received signal and if the residual signal is used to control the tap weights, the system is an adaptive linear predictor. We would like to extend these processing algorithms to handle wide bandwidth signals.

An acoustooptic cell has wide bandwidth and behaves as a delay line which can be tapped optically; we describe here an optical processing architecture that can be used to implement operations similar to those cited. In Sec. II, we briefly review the basic theory of adaptive linear prediction and derive the equivalent frequency plane operator. We then describe the adaptive optical processing technique and relate its operation to those that have been implemented digitally. An important observation is that the optical system can operate with either analog (continuous-time) or sampled (discrete-time) signals with no change in the basic components in the system.

II. Adaptive Linear Prediction

We now describe the basic function of an adaptive linear predictor. A general version of the predictor for discrete-time signals is shown in Fig. 1. Let $s(t)$ be the received signal that has been sampled at the proper rate. The delayed samples are multiplied by the weights c_j , $j = 1$ to N , to produce an estimate $\hat{s}(t)$:

$$\hat{s}(t) = \sum_{j=1}^N c_j s(t - jD), \quad (1)$$

where D is the time delay of each element of the tapped

The author is with Harris Corporation, Government Systems Group, Advanced Technology Department, P.O. Box 37, Melbourne, Florida 32901.

Received 22 June 1982.

0003-6935/82/224005-07\$01.00/0.

© 1982 Optical Society of America.

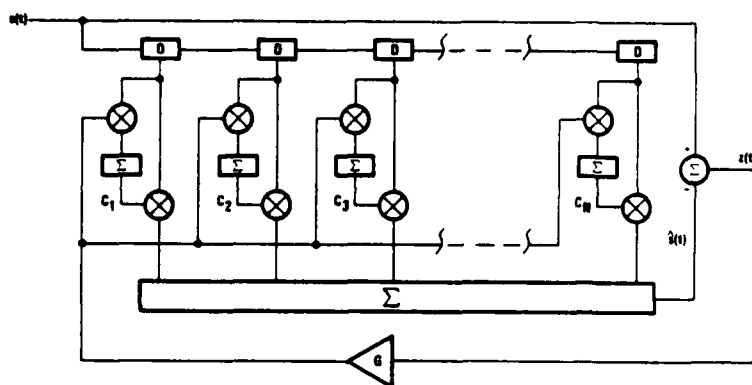


Fig. 1. Block diagram of adaptive linear predictor using discrete tapped delay lines.

delay line, and N is the number of delays. The optimum weights must be determined based on our criterion for how well the estimated signal $\hat{s}(t)$ represents $s(t)$. A commonly used criterion is to minimize the squared error of the residual signal $z(t) = s(t) - \hat{s}(t)$.

Let E be the total energy of the residual signal:

$$E = \sum_M \left[s(t) - \sum_{j=1}^N c_j s(t - jD) \right]^2, \quad (2)$$

where the energy is summed over M samples. We minimize E with respect to a specific tap weight c_i through the derivative

$$\frac{\partial E}{\partial c_i} = -2 \sum_M \left[s(t) - \sum_{j=1}^N c_j s(t - jD) \right] s(t - iD). \quad (3)$$

If we set the derivative equal to zero, we find that the optimum fixed tap weights are given by the solutions to the N equations

$$\sum_{j=1}^N c_j R[(i - j)D] = R(iD), \quad i = 1 \text{ to } N, \quad (4)$$

in which $R(\cdot)$ can be thought of as the covariance matrix if the sum is over a set of sample values, or as the correlation function if the sum is over time.

In some applications, the characteristics of $s(t)$ are such that we can improve the performance of the system by adapting the weights in time. If the rate of change is slow (i.e., the process is quasi-stationary), we can use the method of steepest descent^{3,9} to determine the direction in which we need to adjust the weights. From Eq. (3) we see that the value of the derivative can also be computed as

$$\frac{\partial E}{\partial c_j} = -2 \sum_M z(t) s(t - jD), \quad j = 1 \text{ to } N. \quad (5)$$

We can calculate these derivatives if we multiply the residual signal by the delayed values of the received signal and use this signal to update the tap weights. This process is shown in Fig. 1, wherein the predicted signal $\hat{s}(t)$ is subtracted from $s(t)$, the residual $z(t)$ is multiplied by a loop gain G , and the residual signal is then multiplied by the delayed received signal at the output of each tap to provide the derivative for adjusting the tap weight as given by Eq. (5).

Rhodes¹⁸ described an optical implementation of the adaptive linear prediction filter shown in Fig. 1. The

implementation was in the time domain using a combination of an electrooptic light modulator and an acoustooptic Bragg cell in a time-integrating architecture to form the product given in Eq. (5). The integration and the storage of the tap weights was performed by a liquid crystal spatial modulator; the spatial positions in the light modulator correspond to the time delays. A second Bragg cell was then used to perform the operation given by Eq. (1) and a photodetector provided the signal $\hat{s}(t)$. This implementation has some disadvantages in that the full bandwidth of the Bragg cells is not used and the spatial modulator has limited dynamic range. The implementation can also be performed in the frequency domain to more fully utilize the available bandwidth. The main purpose of this paper is to develop such a technique; its advantages will become apparent later.

To cast the problem into frequency domain notation, we must first describe the adaptive linear predictor in terms of continuous-time variables. In the optical implementation, the delay line taps are not discrete, although the number of independent tap weights is determined by the time-bandwidth product of the Bragg cells. We begin by calculating the value of the tap weights. Let the j th weight at time t be the sum of its value at the previous update time $t - \tau_1$ and the value of the error derivative:

$$c_j(t) = c_j(t - \tau_1) + G \int_{t-\tau_1}^t z(u) s(u - jD) du, \quad (6)$$

where T_1 is the integration time of the accumulator whose output provides the updated weight value. When the system reaches steady state, we find that $c_j(t) = c_j(t - \tau_1)$, so that the value of the integral in Eq. (6) must be zero. Since the integral is the cross-correlation of the received signal and the residual signal, we have the physical insight that the system adapts its weights until the residual contains no components that are correlated with the input; this is sometimes called the correlation cancellation loop method for implementing adaptive filtering.¹⁴ This method for calculating the adaptive weights can be done in real time and saves the computational complexity of inverting the matrix formulation given by Eq. (4).

The passage to a continuous-time representation is fairly straightforward. We represent the delayed signal

as $s(t - \tau)$; it is multiplied by $c(\tau)$ and integrated over the total time delay T of the delay line to give

$$\hat{s}(t) = \int_0^T c(\tau) s(t - \tau) d\tau. \quad (7)$$

The value of the continuous-weight function $c(\tau)$ can be found by repeated application of Eq. (6) or directly by noting that

$$c(\tau) = G \int_{t-T_1}^t z(u) s(u - \tau) du. \quad (8)$$

If the accumulator time window T_1 is sufficiently long relative to the variations in the statistics of the input signal, the weights are not a function of the present time t . During the adaptation period, or during periods when the signal statistics change significantly, the weights are functions of both t and T . We retain the implicit relationship of $c(\tau)$ to time t as in Eq. (8) to aid in deriving the Fourier domain solution. We now substitute Eq. (8) into Eq. (7) to get

$$\hat{s}(t) = G \int_{t-T_1}^t \int_0^T z(u) s(u - \tau) s(t - \tau) d\tau du. \quad (9)$$

After some changes of variables, we can express Eq. (9) as

$$\hat{s}(t) = G \int_{-T_1}^0 \int_{-T}^0 z(t+q) s(t+q+\tau) s(t+\tau) dq d\tau. \quad (10)$$

To assist in solving Eq. (10), we need a definition for the instantaneous Fourier transform of a truncated continuous-time signal. We define

$$F_T(\omega, t) = \int_{t-T}^t f(u) \exp(-j\omega u) du, \quad (11)$$

or, in an equivalent and sometimes useful form, we have

$$\exp(j\omega t) F_T(\omega, t) = \int_{-\infty}^{\infty} \text{rect}\left(\frac{u+T/2}{T}\right) f(t+u) \exp(-j\omega u) du. \quad (12)$$

We use the rectangular function and the inversion of Eq. (12) in Eq. (10) to get that

$$\begin{aligned} \hat{s}(t) = G \int_{-\infty}^{\infty} \int_{-\infty}^{\infty} dq d\tau & \left[\int_{-\infty}^{\infty} Z_{T_1}(\omega, t) \exp[j\omega(t+q)] d\omega \right] \\ & \times s(t+q+\tau) \left[\int_{-\infty}^{\infty} S_T(\xi, t) \exp[j\xi(t+\tau)] d\xi \right], \end{aligned} \quad (13)$$

or that

$$\begin{aligned} \hat{s}(t) = G \int_{-\infty}^{\infty} \int_{-\infty}^{\infty} Z_{T_1}(\omega, t) S_T(\xi, t) \exp[j(\omega + \xi)t] \\ \times \int_{-\infty}^{\infty} s(t+q+\tau) \exp[j(\omega q + \xi\tau)] dq d\tau d\xi d\omega. \end{aligned} \quad (14)$$

We now perform the integration on τ , using a change of variables in which $t+q+\tau = u$. Further, although the range of integration on τ appears to be infinite, the rectangular functions must be used again to limit the range on u to the interval $t+q-T$ to $t+q$. The integral on u now becomes

$$\begin{aligned} \int_{t+q-T}^{t+q} s(u) \exp(j\xi u) du \exp[-j\xi(t+q)] \\ = S_T(-\xi, t+q) \exp[-j\xi(t+q)] \end{aligned} \quad (15)$$

by virtue of Eq. (11). If the statistics of $s(t)$ are slowly varying relative to the total delay time represented by the taps, we have $S_T(-\xi, t+q) \approx S_T(-\xi, t)$. Furthermore, we note from Eq. (11) that $S_T(-\xi, t) = S_T^*(\xi, t)$ if the received signal is real. We can now combine Eq. (15) with Eq. (14) to get

$$\begin{aligned} \hat{s}(t) = G \int_{-\infty}^{\infty} \int_{-\infty}^{\infty} Z_{T_1}(\omega, t) |S_T(\omega, t)|^2 \exp(j\omega t) \\ \times \left\{ \int_{-\infty}^{\infty} \exp[-jq(\xi - \omega)] dq \right\} d\xi d\omega. \end{aligned} \quad (16)$$

The integral on q is bounded by the range $0 \leq q \leq T_1$; we see that this integral has the form $\text{sinc}[(\xi - \omega)T_1/2]$. We note, however, that the definition of $F_T(\omega, t)$ is such that it already contains the effects of convolution with a sinc function due to a time truncation. If $T_1 \geq T$, the additional convolution in Eq. (16) will not affect the results and we can complete the integrations to get the final result:

$$\hat{s}(t) = G \int_{-\infty}^{\infty} Z_{T_1}(\omega, t) |S_T(\omega, t)|^2 \exp(j\omega t) d\omega. \quad (17)$$

If the received signal is bandlimited to a bandwidth W , the limits in Eq. (17) are finite and restricted to the frequency range of the signal.

Equation (17) is the frequency domain representation of the estimated signal $\hat{s}(t)$. We carried out the derivation in some detail, because treating the limits of integration required considerable care throughout. Furthermore, the derivation gives some insight into how the result given by Eq. (17) can be implemented by the use of Bragg cells.

III. Adaptive Optical Processor

If a Bragg cell is positioned so that its transducer is located on the optical axis, we can represent a signal traveling in the negative direction as $f(t+x/v)$, where v is the acoustic velocity, and x is the spatial coordinate. Equation (10) suggests that we need to convolve three such functions whose values are shown in Fig. 2. The function $z(t+q)$ can be produced by a Bragg cell whose transducer is located at the $q=0$ axis, with the wave propagating in the negative q direction. The function $s(t+\tau)$ can be produced by a Bragg cell whose transducer is located at the $\tau=0$ axis, with the wave propagating in the negative τ direction. The function $s(t+q+\tau)$ must be multiplied by the other two functions. We see that if a third Bragg cell has its transducer located on the $q=-\tau$ axis, with the wave propagating in the negative $q+\tau$ direction, we have formed the appropriate products. The limits of integration are also shown in Fig. 2.

We now show how to implement these functions optically by first generating the product equivalent to $z(t+q)s(t+\tau)$. Consider the optical configuration shown in Fig. 3. This subsystem contains two orthogonally oriented Bragg cells in which the information contained in the first Bragg cell is multiplied by the information contained in the second. These two Bragg cells are then imaged onto a common plane P_3 , although in practice it is sufficient that the optical system perform the ap-

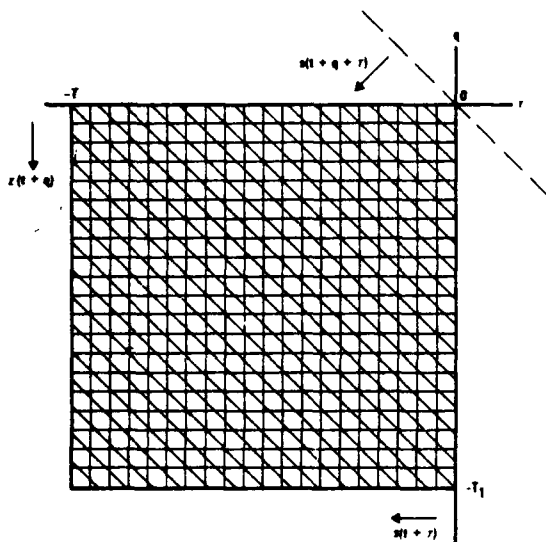


Fig. 2. Convolution of three signals necessary to produce estimate of received signal.

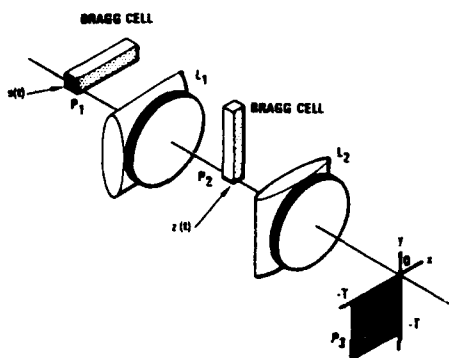


Fig. 3. Optical implementation to produce a spatial cross-correlation function.

appropriate Fourier transform of the product of the signals contained in the Bragg cells. Each Bragg cell has a time delay T and a length $L = vT$. The bandwidth of the Bragg cells is W , so that the number of independent time delays is $N = 2TW$. Both Bragg cells are positioned so that their transducers are located on the optical axis; this is done partly because it simplifies the mathematics and partly because it leads to some interesting physical interpretations of the results.

The first Bragg cell in plane P_1 is driven by the received signal $s(t)$, which has been translated to a suitable center frequency ω_c . The undiffracted light is removed, and the Bragg cell is imaged onto plane P_3 so that the light distribution is uniform in the y direction. In the x direction we have

$$a_1(x, t) = jm_1 \sqrt{\alpha P/L} s(t + x/v) \exp[j\omega_c(t + x/v)], \quad (18)$$

where m_1 is the modulation index of the first Bragg cell, P is the laser power, and α is that fraction of the laser power that reaches plane P_1 . This function is now multiplied by the transmittance of the second Bragg cell, which is

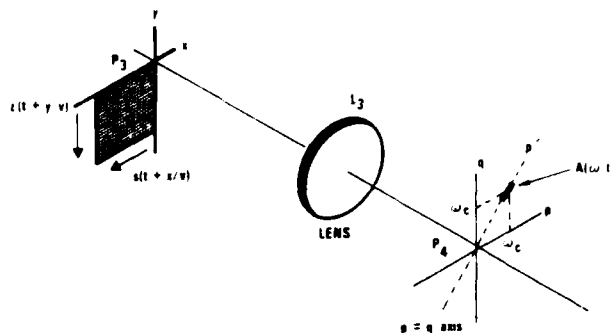


Fig. 4. Optical system to produce cross-spectrum of truncated time signals.

$$a_2(y, t) = jm_2 \sqrt{\alpha P \sigma_s^2/L} z(t + y/v) \exp[j\omega_c(t + y/v)], \quad (19)$$

where m_2 , the modulation index of the second Bragg cell, is generally different from m_1 , and σ_s^2 is the average signal power in the time interval T .

We now arrange to take the 2-D Fourier transform of $a_1(x, t)a_2(y, t)$ as shown in Fig. 4:

$$A(p, q, t) = \int_{-L}^0 \int_{-L}^0 a_1(x, t)a_2(y, t) \exp[-j(px + qy)] dx dy. \quad (20)$$

We want to show that $A(p, q, t)$ is equivalent to the Fourier transform of the cross-correlation of $z(t)$ and $s(t)$. As shown by Eq. (20), the integral is separable in x and y . We need to couple the time-delay arguments of $a_1(x, t)$ and $a_2(y, t)$ so that the cross-correlation is displayed as a function of space instead of time. One way to do this is to rotate the coordinate axes in plane P_3 followed by a 1-D Fourier transform.¹⁹ An alternative method is to perform the 2-D Fourier transform and to evaluate it along the line $p = q$. This is equivalent to a rotation of the axes in the Fourier plane and using a narrow slit oriented along the $q' = 0$ axis, where p' and q' are the new coordinates. We then have $p = q = p'/\sqrt{2}$, which we use in Eq. (20) along with the associations that $\tau_x = x/v$, $\tau_y = y/v$, and $\omega = v p'/\sqrt{2}$. Equation (20) can now be written as

$$A(\omega, t) = v^2 A_1 \int_{-T}^0 \int_{-T}^0 s(t + \tau_x) z(t + \tau_y) \exp[j\omega_c(t + \tau_x)] \times \exp[j\omega_c(t - \tau_y)] \exp[-j\omega(\tau_x + \tau_y)] d\tau_x d\tau_y, \quad (21)$$

where $A_1 = -m_1 m_2 \sqrt{\alpha P \sigma_s^2/L}$. We solve the integral on τ_x first. We have

$$A_1(\omega, t) = \int_{-T}^0 s(t + \tau_x) \exp[j\omega_c(t + \tau_x)] \exp(-j\omega \tau_x) d\tau_x.$$

Let $t + \tau_x = u$, so that

$$A_1(\omega, t) = \int_{t-T}^t s(u) \exp[j\omega_c u] \exp[-j\omega(u - t)] du. \quad (22)$$

Given the definition of the instantaneous Fourier transform of a time function as in Eq. (11), we recognize that Eq. (22) can be expressed as

$$A_1(\omega, t) = S_T(\omega - \omega_c, t) \exp(j\omega t). \quad (23)$$

In a similar fashion, we evaluate the integral on τ_y and combine all factors to get

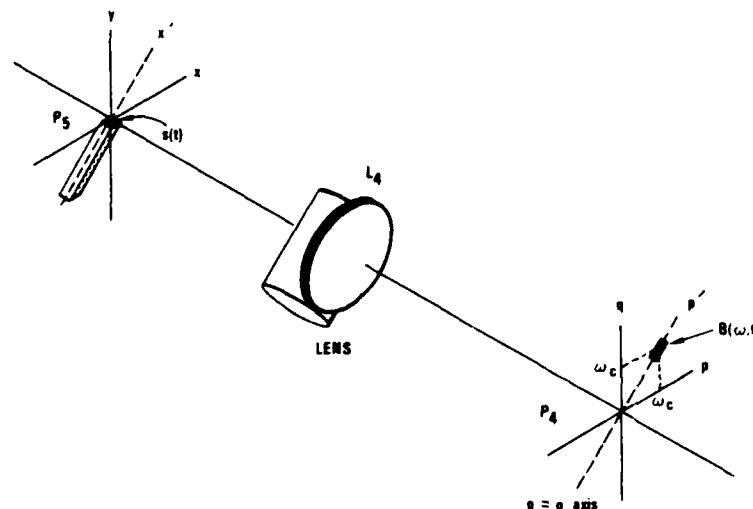


Fig. 5. Second leg of interferometric system.

$$A(\omega, t) = v^2 A_1 S_T(\omega - \omega_c, t) Z_T(\omega - \omega_c, t) \exp(j2\omega t). \quad (24)$$

This result shows that the complex valued light amplitude along the line $p = q$ in plane P_4 is the product of the Fourier transforms of $s(t)$ and $z(t)$. By the use of the convolution theorem, $A(\omega, t)$ is also the Fourier transform of the cross-correlation of $s(t)$ and $u(t)$ as desired.

We now want to multiply $A(\omega, t)$ by a third function associated with $s(t + q + \tau)$ and integrate the product over the frequency plane. This can be achieved interferometrically by using a third Bragg cell in a separate path of the interferometer. Consider the optical system shown in Fig. 5, which shows the second part of the interferometer. Since the important part of $A(p, q, t)$ lies along the line $p = q$ and is centered at $p' = \sqrt{2}\omega/v$, we orient the third Bragg cell at a 45° angle to the $x - y$ coordinate system of plane P_5 . To preserve the frequency scaling, the Fourier transform lens L_4 must have a focal length a factor of $\sqrt{2}$ longer than that of L_3 . In this path, we use a cylindrical lens to image the line illumination of the Bragg cell at plane P_4 to conserve the optical power.

The transducer of the Bragg cell is located at the optical axis and is driven by $s(t)$. If $(1 - \alpha)P$ is the fraction of the laser power available at plane P_5 , the effective amplitude of the signal at plane P_5 is

$$b(x', t) = jm_3 \sqrt{(1 - \alpha)P/L} s(t + x'/v) \exp[j\omega_c(t + x'/v)], \quad (25)$$

where x' is the coordinate axis in plane P_5 that contains the Bragg cell. The 1-D Fourier transform is now

$$B(\omega, t) = vB_1 \int_{-T}^0 s(t + \tau_x) \exp[j\omega_c(t + \tau_x)] \exp(-j\omega\tau_x) d\tau_x, \quad (26)$$

where $B_1 = jm_3 \sqrt{(1 - \alpha)P/L}$, $\tau_x = x'/v$ and $\omega = v p' / \sqrt{2}$. By following the same procedure as before, we find that

$$B(\omega, t) = vB_1 S_T(\omega - \omega_c, t) \exp(j\omega t). \quad (27)$$

Suppose that we now place a single photodetector at plane P_4 along the line $p = q$, located so that its center is at ω_c and its physical extent corresponds to the range $|\omega - \omega_c| \leq W/2$. The photodetector current will be proportional to the intensity at plane P_4 :

$$i(t) = C \int_{\omega_c - W/2}^{\omega_c + W/2} I(\omega, t) d\omega, \quad (28)$$

where C is a constant that includes the photodetector sensitivity S , expressed in amps/watt as well as the conversion factors necessary to cause Eq. (28) to be dimensionally correct. We have

$$I(\omega, t) = |A(\omega, t) + B(\omega, t)|^2 = |A(\omega, t)|^2 + |B(\omega, t)|^2 + 2\text{Re}[A(\omega, t)B^*(\omega, t)]. \quad (29)$$

The photodetector current can, therefore, be separated into three terms as given by Eqs. (28) and (29). From Eqs. (24) and (27), we note that the first two terms are not functions of time; they therefore contribute only to a bias current. This statement is not strictly true, because $S_T(\omega, t)$ and $Z_T(\omega, t)$ are functions of time through the definition of the instantaneous Fourier transform. These functions are slowly varying, however, relative to the variations in the third term and can be removed by a bandpass filter after detection.

The main term of interest is the third term of Eq. (29) which, when substituted into Eq. (28) with the results of Eqs. (24) and (27), leads to

$$i_3(t) = 2v^3 A_1 B_1 C \int_{\omega_c - W/2}^{\omega_c + W/2} Z_{T_1}(\omega - \omega_c, t) |S_T(\omega - \omega_c, t)|^2 \times \exp(j\omega t) d\omega. \quad (30)$$

By a change of variables, we can write Eq. (30) as

$$i_3(t) = 2v^2 A_1 B_1 C \exp(j\omega_c t) \int_{-W/2}^{W/2} Z_{T_1}(\omega, t) |S_T(\omega, t)|^2 \times \exp(j\omega t) d\omega. \quad (31)$$

We see that the integral in Eq. (31) is exactly the one we wanted to evaluate [compare Eq. (17)]. The output

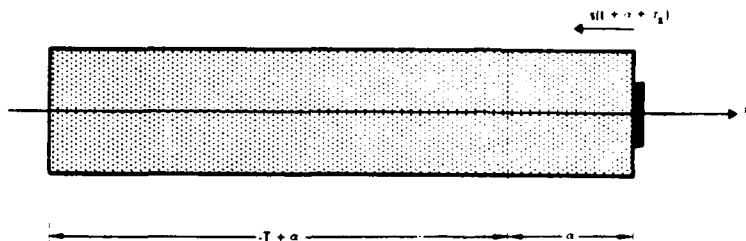


Fig. 6. Arrangement of Bragg cell to generate delayed estimate.

occupies bandwidth W and is centered at ω_c . By comparison, the first two terms of Eq. (28) have a bandwidth of $<1/T$ centered at $\omega = 0$. The third term can, therefore, be easily separated from the low-frequency terms. It turns out that $B(\omega, t)$ is in phase quadrature with $A(\omega, t)$ as can be seen by considering the values of A_1 and B_1 . The correct phase relationship can be obtained by introducing a $\pi/2$ phase shift in the carrier used to drive the third Bragg cell or by optically phase shifting the two beams in the interferometer.

The optical architecture described so far is characteristic of one in which we form an estimate $\hat{s}(t)$ at the present time t from some past history of $s(t)$. We may also wish to introduce an additional time delay α to arrive at an estimate $\hat{s}(t - \alpha)$ or to predict the received signal at some time $t + \alpha$.²⁰ Suppose that we geometrically move the third Bragg cell by an amount $x = v\alpha$ as shown in Fig. 6. The signal within the cell is now $s(t - \alpha + \tau_x) \exp[j\omega_c(t - \alpha + \tau_x)]$, and if we perform the Fourier transform as before, we arrive at the result

$$B(\omega, t) = vB_1S_T(\omega - \omega_c, t) \exp[j\omega(t - \alpha)], \quad (32)$$

which, in turn, leads to

$$i_3(t) = 2v^3A_1B_1C \exp[j\omega_c(t - \alpha)] \int_{-W/2}^{W/2} Z_{T_1}(\omega, t) |S_T(\omega, t)|^2 \times \exp[j\omega(t - \alpha)] d\omega. \quad (33)$$

The output of the photodetector then becomes the estimate $\hat{s}(t - \alpha)$. If the Bragg cell is moved in the opposite direction, the sign of α is reversed and we have the prediction $\hat{s}(t + \alpha)$. The interesting interpretation of this result is that the system processes the received signal in such a way that the estimate (or prediction) occurs at the time value corresponding to the physical position $x = 0$. Thus, if the Bragg cell is moved so that the signal $s(t - \alpha)$ occurs at $x = 0$ (or $\tau_x = 0$), the solution is one of estimation. If the Bragg cell is moved so that the entire cell is located in the negative x plane, there is no received signal at $x = 0$, and the system predicts a signal $\hat{s}(t + \alpha)$ located at $x = 0$.

In many applications it is implicitly assumed that the estimate is at some fairly large value of α relative to T . For example, in the transversal filtering literature, the center tap is often set at the time delay $T/2$. Some physical phenomena such as channel distortion or intersymbol interference have an asymmetrical response, so that better results can be achieved by selecting the tap position to weight the tails of the response. In

general, then, one Bragg cell may be more nearly centered on the optical axis; the mathematical analysis is thereby basically unaltered except for a residual time-delay factor in the output.

The frequency plane notation also provides a more direct insight to certain filtering operations. Let us consider, as an example, a filtering application in which we want to remove the effects of a strong narrowband signal that interferes with the information signal. From Fig. 1 we see that

$$z(t) = s(t) - \hat{s}(t), \quad (34)$$

so that, in the sense of the definition of the instantaneous Fourier transform, we also have

$$Z_T(\omega) = S_T(\omega) - \hat{S}_T(\omega). \quad (35)$$

From Eq. (17) we use the result that $\hat{S}_T(\omega) = GZ_T(\omega) - |S_T(\omega)|^2$, so that

$$Z_T(\omega) = \frac{S_T(\omega)}{1 + G|S_T(\omega)|^2}. \quad (36)$$

It is tempting to define the transfer function for the system as $H(\omega) = Z_T(\omega)/S_T(\omega)$. In general, this is not a valid procedure because the system behaves in a nonlinear fashion during adaptation. Suppose, however, that the system has reached its steady-state condition and that the input signal statistics are not changing. Then we can say that

$$H(\omega) = \frac{Z_T(\omega)}{S_T(\omega)} = \frac{1}{1 + G|S_T(\omega)|^2}. \quad (37)$$

We see that the overall transfer function is unity where the value of $G|S_T(\omega)|^2$ is small. The presence of strong signal components around, say, ω_o produces an inverse filter $H(\omega) \approx 1/G|S_T(\omega_o)|^2$, which suppresses the energy near ω_o . In a general sense, we see that the equivalent filter adapts to whiten the input signal spectrum.

The adaptation time is dependent on the specific application, although it appears that most systems cited in the literature adapt within a time interval corresponding to 500–2000 data samples. The adaptation time is determined, in part, by the required values of T and T_1 ; these values also influence noise in the tap weights and, therefore, the accuracy at convergence. The gain factor G also affects both the rate of adaptation and the accuracy. Finally, the dynamic range of the photodetector determines the minimum increment

by which the tap weights can be set. Generally, at least 10^3 distinct levels provide adequate performance. How these various factors interrelate is highly dependent on the specific application.

IV. Summary and Conclusions

The adaptive optical processing technique described here has several important features. First, since it is the optical equivalent of an adaptive digital transversal filter, it affords a high degree of flexibility and is applicable to solving a wide range of problems. Second, implementing the process in the Fourier domain allows the use of the full wide bandwidth of Bragg cells. We can envision, for example, the processing of data in the 100–1000-MHz range. Third, the processing is done on the amplitude and not the intensity of the light, so that we do not need to introduce bias terms to generate both positive and negative weights. Because the system is interferometric in the temporal sense, the dynamic range is high and the system is insensitive to scattered light. By virtue of having a single photodetector and no requirement for an intermediate storage medium, both phase and amplitude errors are reduced.

This work was supported by U.S. Army Research Office.

References

1. J. Makhoul, *Proc. IEEE* **63**, 561 (1975).
2. R. W. Lucky, *IEEE Trans. Inf. Theory* **IT-19**, 725 (1973).
3. R. W. Lucky, *Bell Syst. Tech. J.* **47**, 549 (1968).
4. R. W. Lucky, *Bell Syst. Tech. J.* **44**, 255 (1965).
5. R. W. Lucky and H. R. Rudin, *Bell Syst. Tech. J.* **46**, 2179 (1967).
6. D. Hirsch and W. J. Wolf, *IEEE Trans. Commun. Technol. COM-18*, 5 (1970).
7. C. W. Niessen and D. K. Willim, *IEEE Trans. Commun. Technol. COM-18*, 377 (1970).
8. A. Lender, *IEEE Trans. Commun. Technol. COM-18*, 625 (1970).
9. B. Widrow, P. Mantey, L. Griffiths, and B. Goode, *Proc. IEEE* **55**, 2143 (1967).
10. L. J. Griffiths, *Proc. IEEE* **57**, 1696 (1975).
11. See also the special issue on Adaptive Systems, *Proc. IEEE*, **64**, 1126 (August 1976).
12. B. Widrow *et al.*, *Proc. IEEE* **63**, 1692 (1975).
13. L. J. Griffiths, *IEEE Trans. Acoust. Speech Signal Process. ASSP-23*, 207 (1975).
14. D. R. Morgan and S. E. Craig, *IEEE Trans. Acoust. Speech Signal Process. ASSP-24*, 494 (1976).
15. R. W. Schaefer and J. D. Markel, *Speech Analysis* (IEEE, New York, 1979).
16. J. D. Gibson, *Proc. IEEE* **68**, 488 (1980).
17. J. G. Proakis and J. H. Miller, *IEEE Trans. Inf. Theory* **IT-15**, 484 (1969).
18. J. F. Rhodes, "An Optical Adaptive Filter," *Proc. Soc. Photo-Opt. Instrum. Eng. Symposium on Real Time Signal Processing*, **341**, in press (1982).
19. J. D. Cohen, *Proc. Soc. Photo-Opt. Instrum. Eng.* **180**, 134 (1979).
20. J. B. Thomas, *Statistical Communication Theory* (Wiley, New York, 1969), p. 218.

Reprinted from **Applied Optics**, Vol. 22, page 381, February 1, 1983
Copyright © 1983 by the Optical Society of America and reprinted by permission of the copyright owner.

Adaptive optical processor: errata

A. VanderLugt

Harris Corporation, Government Systems Group, Advanced Technology Department, P.O. Box 37, Melbourne, Florida 32901.

Received 12 November 1982.

0003-6935/83/030381-02\$01.00/0.

© 1983 Optical Society of America.

In my paper on adaptive optical processing,¹ I was not consistent in drawing the axes for the figures to accurately represent the mathematical functions. If we replace the variable τ by $-\tau$ and change the limits of integration in Eq. (10), the net effect is to reverse the orientation of the horizontal Bragg cell in Fig. 3. The final results are not affected by this change.

Also, in evaluating Eq. (14), it is better to integrate $s(t + q - \tau)$ over q and τ simultaneously instead of sequentially. This procedure produces the same results without the sometimes restrictive assumption that $S_T(-\xi, t + q) \approx S_T(-\xi, t)$.

Reference

1. A. VanderLugt, *Appl. Opt.* 21, 4005 (1982).

APPENDIX E

OPTICAL TRANSVERSAL PROCESSOR FOR NOTCH FILTERING

TO APPEAR IN OPTICAL ENGINEERING

VOLUME 23, MAY-JUNE, 1984

OPTICAL TRANSVERSAL PROCESSOR

FOR NOTCH FILTERING

By

A. VanderLugt
Advanced Technology Department
Government Systems Sector
Harris Corporation
Melbourne, Florida 32901

ABSTRACT

A frequency domain implementation of an optical transversal processor has been described previously. Since this system uses Bragg cells both as the delay line and as the accumulators which provide the tap weights, a key question is what effect the finite integration times have on the performance of the system. Computer programs were written to simulate an adaptive notch filtering application; the measure of performance is the correlation coefficient for the residual signal and the desired received signal. The correlation coefficient was increased significantly by tapering the accumulators so that the readaptation phenomena caused by large values leaving the accumulator are minimized. Several examples of the performance are given as a function of the number of taps, the length and degree of taper of the accumulator, the feedback gain and the number of iterations. The results show that a finite accumulator is not a serious drawback, particularly for those applications where the system must operate in a rapidly changing environment. The performance of the system then approaches that of one having an infinite accumulator with the gain adjusted to give equivalent tracking performance.

OPTICAL TRANSVERSAL PROCESSOR FOR NOTCH FILTERING

1. INTRODUCTION

Adaptive filtering, using transversal tapped delay lines with feedback, has been applied to problems such as redundancy removal in data, reducing intersymbol interference through equalization, noise cancellation, self-tuning and speech processing.¹⁻⁸ The data rate or the signal bandwidth is limited by the processing speeds of digital circuits; we wish to investigate the use of optical processing to extend the bandwidths of signals that can be processed.

An acousto-optic cell has a wide bandwidth and behaves as a delay line that can be tapped optically. Rhodes⁹⁻¹⁰ described an optical implementation of an adaptive linear prediction filter in the time-domain, using a combination of an electro-optic light modulator and an acousto-optic cell in a time-integrating architecture. VanderLugt¹¹⁻¹² described an implementation in the frequency-domain, using three Bragg cells in a space-integrating, interferometric architecture. The main purpose of this paper is to give the results of some computer simulations designed to study the effects of using an accumulator whose integration time is finite.

2. BACKGROUND

A general form of an adaptive linear predictor is shown in Figure 1. Let $s(t)$ be a sampled signal that drives a delay line. The delayed samples are multiplied by the weights c_j to form an estimate $\hat{s}(t)$ of the received signal. The optimum weights are determined by minimizing the mean square error in the residual signal $z(t)$ which leads to the relationship that

$$c(\tau) = G \int_{t-T_1}^{\tau} z(u)s(u-\tau)du, \quad (1)$$

where G is the gain in the feedback loop, T_1 is the integration time of the accumulator and τ represents the continuous-time equivalent of the discrete delay. If we let T_0 be the minimum discernible time delay in a Bragg cell, then NT_0 is the total delay time T of the cell. The estimate of the received signal is

$$\hat{s}(t) = \int_0^T c(\tau)s(t-\tau)d\tau. \quad (2)$$

so that, by substituting (2) into (1), we have

$$\hat{s}(t) = G \int_{t-T_1}^t \int_0^T z(u)s(u-\tau)s(t-\tau)dud\tau. \quad (3)$$

By a change of variables we can rewrite (3) as

$$\hat{s}(t) = G \int_0^T \int_T^t z(t+q)s(t+q-\tau)s(t-\tau)dq d\tau \quad (4)$$

which, in turn, can be used to get the frequency domain representation¹¹

$$\hat{s}(t) = G \int_{-\infty}^{\infty} Z_T(\omega, t) |S_T(\omega, t)| e^{j\omega t} d\omega, \quad (5)$$

where $S_T(\omega, t)$ and $Z_T(\omega, t)$ are the instantaneous Fourier transforms of the most recent T seconds of the received signal and the residual signal.

There are several ways to configure an optical system, using three Bragg cells, to implement (4) or (5); one of these is given in Figure 2. The functions $z(t)$ and $s(t)$ drive two Bragg cells in the directions shown. These two Bragg cells are mutually imaged onto plane P_1 , with the diffracted light from the first Bragg cell passing through the second Bragg cell.

At plane P_1 we have the light distribution necessary to provide the tap weights. This can be more clearly seen from Figure 3a in which the tap weight plane has been rotated by 45 degrees for convenience. The numbers in each delay cell represent the successive time indices for the two functions. If we integrate the light in the vertical direction, as shown by the dotted lines, we obtain the function $c(\tau)$. This function is then convolved with the received signal $s(t)$ which drives a third Bragg cell as we shall show shortly.

The number of tap weights available is equal to twice the time-bandwidth product of the Bragg cell (Figure 3a shows only a small number of taps). From the figure we see that the central tap weight is the sum of N products whereas the end tap weights contain only one product. The end tap weights are therefore likely to be noisy and reduce the performance of the system. The number of taps required depends on the application. To reduce intersymbol interference, the number of taps required is determined by the extent of the channel impulse response which may be of the order of 10-20 symbol periods. For adaptive notch filtering, the number of taps required is determined by the number of frequencies that need to be removed simultaneously; we require at least two taps per frequency. For the notch filtering simulations reported here, approximately 50 taps were used for most of the tests.

If the time-bandwidth product of the Bragg cells is of the order of 1000-2000, the use of only 50 taps means that the triangular weighting of $c(\tau)$ is less significant, and we can truncate the region of integration to the rectangular window as shown in Figure 3b. Each of the 50 taps will then contain approximately 2000-4000 samples which represent the finite length of the accumulators in each of the correlation cancellation loops.

Figure 4 shows that part of the optical system which simultaneously integrates the light in the vertical direction and creates the Fourier transform of the tap weights in the horizontal direction. Along the horizontal axis the light distribution is proportional to $Z_T(\omega, t)S_T(\omega, t)$. The third Bragg cell (not shown here), is arranged so that $S_T(\omega, t)$ is added to $A(\omega, t)$ in an interferometer. The sum is then square law detected to provide the integrand of (5), and the output of a single element photodetector provides the estimate $\hat{s}(t)$.

The advantage of implementing the adaptive transversal processor in the Fourier domain are that the system is linear in amplitude so that no bias terms are needed. As a result, both positive and negative tap weights are generated, and the dynamic range is high. The full bandwidth of the Bragg cells can also be used. A potential disadvantage is the finite accumulators that may reduce the performance of the system. Our major interest is, therefore, to simulate the operation of the system under the constraint of using finite accumulators.

3. THE SIMULATIONS

We wrote a computer program to calculate the performance of the adaptive system. The application we chose to study is that of notch filtering in which the received signal consists of a wideband signal $g(t)$ and one or more cosine jammers:

$$s(t) = g(t) + \sum_{j=1}^M A_j \cos \omega_j t. \quad (6)$$

The wideband signal is either a very long pseudo noise sequence or a Gaussian random signal; each signal has zero mean and unity variance σ_g^2 . The variance of the cosine jammer is $\sigma_c^2 = \sum_{j=1}^M A_j^2/2$. The input signal-to-jammer ratio is then $\text{SNR}_i = 10 \log(\sigma_g^2/\sigma_c^2) = -10 \log(\sigma_c^2)$.

Figure 5 shows the spectrum $|S(\omega)|^2$ of the input signal when $\text{SNR}_i = -18.5$ dB for a system having 50 taps and a fairly short 500 sample accumulator. The spectrum was obtained by letting the system iterate for 2000 input data samples and then calculating a 1024 point discrete Fourier transform of the most recent data samples. The magnitude squared of the system transfer function $|H(\omega)|^2$ is also shown; it is a notch that has formed adaptively to cancel the cosine jammer at a frequency ω_0 . If we let T_0 be the time delay between taps, the frequency of the jammer shown is $\omega_0 = 2\pi/9T_0$. The spectrum $|Z(\omega)|^2$ of the residual signal is also shown, multiplied by a factor of 0.05 for clarity. We see that the input and output spectra are similar except in the region ω_0 where we see some evidence of the cosine jammer in the residual signal.

The presence of some jammer energy in the residual points out a fundamental difference between the frequency plane implementation of adaptive processing and a digital system where the accumulator can be made arbitrarily long. In a digital system, the tap weights converge, after some number of iterations, to stable values so that extremely deep nulls can be formed. In the initial stages of adaptation, the tap weights change toward

their final values at a rate determined primarily by the feedback gain and the jammer amplitude. In the latter stages of adaptation, the new contributions to the tap weights are small in magnitude and tend to alternate in sign. After convergence, we find that $\hat{s}(t)$ is a good estimate of the amplitude and phase of the cosine jammer so that the null is very deep; the null remains deep until there is some change in the statistics of the received signal.

In the optical implementation, the tap weights rapidly assume values close to their final values and an increasingly deeper notch is formed at the jammer frequency. After the number of iterations corresponding to the accumulator length, however, the earliest values in the accumulator (which are large because they contribute most to initial adaptation) begin to leave the accumulator. The cosine component in the residual then increases momentarily because $\hat{s}(t)$ is not as good an estimate of the jammer signal. The system then goes into a "readaptation" phase where the new contributions to the tap weights must offset the older contributions that are leaving the accumulator. This process repeats every MT_0 seconds, where M is the number of samples in the accumulator, but with successively less impact on the residual signal. After enough iterations, the system converges to a steady state where the jammer signal level in the residual is just enough to maintain the tap weights at a (nearly) fixed value over time.

The adaptation and readptation can be seen from Figure 6, in which the upper trace is that of $z(t)$ for the first 2000 data samples. We note that adaptation is relatively rapid; after about 50 data samples the residual signal is primarily composed of the wideband signal $g(t)$. At the end of the 500th data sample, the earliest tap weights are leaving the accumulator and the system "readapts" to the new conditions. Similar readaptations occur at

multiples of 500 data samples and the system performance is not optimum. In an effort to reduce the effects of readaptation, we used a taper on the accumulator so that the values in the accumulator are attenuated exponentially as they flow through. When we used an exponential taper for which the oldest accumulator values are reduced by a factor of one-half relative to their initial values, the residual signal took on the values shown in the lower trace. There is now little evidence of readaptation except for a very slight perturbation after 500 data samples. Note that in both cases $z(t)$ has a zero mean; we have added and subtracted a value of 20 to separate the two traces.

The basic cause of the readaptation is shown in Figure 7, in which the upper trace represents the values within the accumulator associated with the first tap during the first 500 iterations, using no taper. As described before, the earliest contribution to the tap weights are large (those values from 450 to 500) which drive the first tap weight to nearly its final value. Subsequent contributions are small and oscillate about zero (a value of 0.025 was added to the value to separate the two traces). The lower trace shows the results when an exponential taper whose final value is 0.5 is used. The initial contributions to the accumulator are large when they enter the accumulator, leading to rapid adaptation. After they have propagated to the end of the accumulator, their values have been reduced by 0.5 so that when they leave, their impact on $s(t)$ is not so severe. There is, therefore, less evidence of readaptation when the taper is used.

An exponential taper can be implemented optically by placing a mask at the plane where $z(t)$ and $s(t)$ are mutually imaged. The transmittance of the mask would be unity for small signal delays and decay exponentially to a final value of 50% transmittance at the end of the accumulators. In the

discussion to follow, D represents the final value for the exponential taper. Other tapering functions such as a Gaussian weighting may be equally effective, or it may be possible to implement the taper through variable illumination of the Bragg cells so that a separate mask may be necessary.

One question relates to whether $D = 0.5$ is optimum. Other questions relate to the optimum gain as a function of D , the impact that the number of taps or the length of the accumulator have on the performance of the system, the depth of the notch and the output signal-to-noise ratio. To perform these tradeoffs we need a measure of performance. One measure is the degree of distortion between $z(t)$ and $g(t)$. Since the applications of adaptive notch filtering often require a subsequent correlation between $z(t)$ and $g(t)$ over some long time interval, a second measure is the correlation coefficient for the signals $z(t)$ and $g(t)$. As we now show, these two measures are related.

Consider the function

$$y(t) = z(t) - g(t) \quad (7)$$

having mean squared error

$$\sigma_y^2 = E\{(z - g)^2\} \quad (8)$$

This function can be expanded to give

$$\sigma_y^2 = \sigma_z^2 - 2\mu_{zg} + \sigma_g^2 \quad (9)$$

where μ_{zg} is the covariance of $z(t)$ and $g(t)$. We can normalize the covariance to get the correlation coefficient:

$$\rho_{zg} = \frac{\sigma_z^2 + \sigma_g^2 - \sigma_y^2}{2\sigma_z \sigma_g} \quad (10)$$

If the residual signal is identical to $g(t)$, the distortion is zero and the correlation coefficient is one. We shall use the correlation coefficient ρ as our measure of system performance.

The next result shows the sensitivity of the performance to the exponential taper parameter D . Figure 8 shows the correlation coefficient plotted as a function of D for several values of the accumulator length M (expressed as the number of samples stored in the accumulator). The number of taps in this example is 50, and we calculated ρ from (10) over the last 1024 points, having let the system operate for 2000 iterations. We note that the performance improves, as expected, as M increases and that the performance is not a sensitive function of D except for $D > 0.8$ or $D < 0.1$. If $D > 0.8$, we have the readaptation phenomena described before. For $D < 0.1$, the exponential taper reduces the effective length of the accumulator so that a longer accumulator with a high degree of taper may yield a performance inferior to that of a shorter accumulator with less taper. In all cases shown, the optimum value of D is about 0.5 and this value has been used in most of the subsequent tests. It should be noted that, for these preliminary tests, both the accumulator length and the number of iterations are fairly small to conserve computer run time. The performance of the system improves as these two parameters increase as we shall show later; these truncated tests are designed to show the trends in performance.

Figure 9 shows the value of the correlation coefficient as a function of gain with the number of taps as a parameter. In this example, the accumulator length was set at $M = 500$, $D = 0.5$ and the number of iterations was 2000. We would expect that the gain should be inversely proportional to the number of taps because the tap weights, for an ideal system, should be $c(\tau) = (2/T) \cos \omega_0 \tau$. The data from Figure 9 supports this result. The performance improves as the number of taps increases, but it should be noted that my simulations do not account for the triangular area of integration naturally imposed by the Bragg cells as shown in Figure 3a. In any event, the correlation loss for the case of $N = 50$ versus that of $N = 200$ is -0.59 dB versus -0.5 dB which is not a significant change. If the number of taps is at least 50, then, the system performance is quite good for notch filtering.

The depth of the notch cannot be accurately read from the graphs such as that given in Figure 5, partly because the period of the jammer is not a divisor of 1024 which is the sample index for the discrete Fourier transform used to calculate the steady state transfer function. The notch depth can be obtained by freezing the tap weights after adaptation and letting only the jammer signal continue. The notch depth is the ratio of the variance σ_z^2 of the residual, which is an attenuated replica of the jammer, to the variance σ_c^2 of the input jammer. For the example given in Figure 5, the notch depth by this method of calculation is -31.5 dB. In a similar fashion, the output signal-to-noise ratio can be estimated by the ratio of σ_g^2 to σ_z^2 after the weights are frozen. Table 1 gives the notch depth and output signal-to-noise ratio for a single jammer, with $N = 48$.

TABLE 1. Performance Parameters

<u>SNR_i</u>	<u>σ_z^2</u>	<u>σ_g^2</u>	<u>SNR_o</u>	<u>Notch Depth</u>
-19.9 dB	0.025	1	16.0 dB	-35.9 dB
-13.9 dB	0.003	1	25.6 dB	-39.5 dB
-7.9 dB	0.007	1	21.3 dB	-29.2 dB
-1.9 dB	0.008	1	20.8 dB	-22.7 dB

$M = 4000$, and $D = 0.5$. The gain was adjusted to produce the maximum correlation coefficient at the point where the tap weights were frozen for the strongest jammer. Since the tap weights were frozen after only 4000 iterations, the system has not yet reached its optimum steady state performance and the values given in Table 1 are understated somewhat. Since the residual must always contain a portion of the jammer energy, we see that the notch depth is a function of the input jammer power. As the input jammer level decreases, the notch depth decreases to allow the feedback loop to maintain the proper set of tap weights.

The results of the simulations can be compared with those obtained by digital systems having infinite accumulators. The most obvious difference is in the depth of the notch. Since the residual must contain some component of the jammer signal, the notch depth cannot exceed a given value. In passing, it is worth noting that if a separate noise signal were available, as in some of the applications noted by Widrow, et al⁶, this restriction is removed and deeper notches could be obtained. Let us assume, then, that the component of the jammer in the residual is of the form $B \cos[\omega_0 t + \phi]$ when the jammer is of the form $A \cos \omega_0 t$. If the jammer and wideband signal $g(t)$ are uncorrelated, the steady state transfer function for ω near ω_0 can be approximated by $H(\omega)$, where

$$|H(\omega)|^2 = 1 - 2R \cos[(\omega - \omega_0) NT_0(1 + 4/N)/2] \text{sinc}[(\omega - \omega_0) NT_0/2] + R^2 \text{Sinc}^2[(\omega - \omega_0) NT_0/2], \quad (11)$$

where

$$\left. \begin{aligned} R &= \frac{1}{2} K G A B N M \\ B &= A / (1 + K / A N M / 4) \end{aligned} \right\} \quad (12)$$

and where G is the feedback gain, N is the number of taps of delay T_0 , M is the number of samples stored in the accumulator and k is a factor which accounts for the taper along the accumulator. If the taper along the accumulator is severe, the output of the accumulator will be smaller ($k < 1$) than that for an untapered accumulator ($k = 1$). To achieve the same notch depth, the feedback gain needs to be increased somewhat to offset the effects of the taper.

If we use the value of B in (11) and calculate the notch depth at $\omega = \omega_0$, we have that

$$|H(\omega_0)|^2 = \left[1 - \frac{kGA^2NM}{4+kGA^2NM} \right]^2 \quad (13)$$

We note that the notch depth increases as the jammer amplitude A increases to the point where the value of the jammer component B in the residual have the value given by (12). From our simulations, however, we find that the length of the accumulator is the most important parameter for obtaining a very deep null. As the factor kGA^2NM becomes very large relative to the factor 4, the notch depth increases and we have that $B \approx 4/kGANM$. For an exponential taper in which $D = 0.5$, we find that $k = 0.49$; this value, along with the values of G , A , N and M from the simulation gives a calculated notch depth of -35.4 dB vs a depth of -35.0 dB as given by the data.

The half-power bandwidth can also be obtained from (11). If the value of Δf is small compared to f_0 , we can expand each term of (11) and arrive at the result that

$$\Delta f = \frac{2}{\pi NT_0} \left[\frac{2 - R - 1/2R}{4/3 - R/3 + 4/N} \right]^{1/2} \quad (14)$$

Although the bandwidth is a function of the notch depth through the parameter R , we can simplify (14) for values of $R > 0.9$ (i.e. for notch depths more than 20 dB down) so that

$$\Delta f \approx \frac{1}{NT_0 \sqrt{1+4/N}} \quad (15)$$

This result shows that the half-power bandwidth is primarily determined by the number of taps used. If N is large compared to 4, the bandwidth is given by $\Delta f \approx 1/2NT_0$. The bandwidths as determined by the simulations agree closely with the values calculated from (15). Figure 10 shows the transfer function for both a finite (4000 samples) and infinite accumulator for a $N = 48$ tap situation. The half-power bandwidth is very nearly the same for the two cases, but the notch depth is about 6 dB greater for the infinite accumulator. The data was taken after 10,000 iterations; the notch depth for the infinite accumulator should continue to grow as the number of iterations increase, if we assume that the jammer and the signal are uncorrelated.

The adaptation time constant for low values of the gain, an infinite accumulator and uncorrelated input signal and noise, is given by^{6,7}

$$\tau_p = -1/\ln(1 - G\lambda_p) \quad (16)$$

or

$$\tau_p \approx 1/G\lambda_p \quad (17)$$

where τ_p is the adaptation time constant for the p^{th} mode whose eigenvalue is λ_p . If the eigenvalues are not equal, the adaptation time constant does not have a unique value. A reasonable estimate can be made, however, by averaging the eigenvalues so that λ_p is replaced by λ_{ave} .

Widrow, et al,¹⁴ introduced the concept of the degree of misadjustment of an adaptive system and related it to the adaptive time constant. This misadjustment is a measure, expressed as a percentage, of the actual mean square error between the output signal and the desired response to the mean square error based on the optimum Wiener solution. The misadjustment can be related to the adaptation constant τ_{ave} and the number of taps through

$$\Delta = N/4 \tau_{\text{ave}}. \quad (18)$$

The misadjustment given by (18) originates from random noise in the tap weights due to the use of a noisy gradient instead of the true gradient in the adaptation process. The relationships in (16-18) are valid only when the adaptation process is slow; this generally implies that the gain is small. When the gain is small, a second type of misadjustment may arise due to nonstationary input statistics; this has been called the misadjustment due to lag. As noted by Widrow¹⁴, the best performance is achieved by setting the gain so that the misadjustments due to gradient noise and lag are equal.

In terms of the notation used here, the total misadjustment can be represented by $\Delta_T = (\sigma_z^2 - \sigma_g^2) / \sigma_g^2$ since the jammer power should be completely removed in the optimum Weiner solution. As we have noted before, the finite length of the accumulator in the optical implementation requires that some jammer signal be present in the residual. The total misadjustment is, therefore, the sum of that due to gradient noise, lag, and jammer power. Further, as we see from Figure 9, the performance does not improve monotonically as the gain decreases, since the accumulators have finite length. As a result, the optimum gain is generally higher than that used if the accumulator were infinite so that the misadjustment is principally due to gradient noise and jammer power.

Since the gain is a function of the accumulator length, the value of the adaptation time constant as calculated from (16) or (17) tends to lead to erroneous results. A better procedure is to calculate the jammer power in the residual from (12) and to then calculate the misadjustment due to gradient noise from

$$\Delta = \frac{\sigma_z^2 - B^2/2 - j_g^2}{\sigma_g^2} \quad (19)$$

The adaptation time constant can then be calculated from (18). As an example of this procedure, we use the results from the simulations given in Table 1. We found, at the end of 8000 iterations, that $\sigma_z^2 = 1.12$ and $\sigma_g^2 = 1$. The gain was $G = 1.25(10^{-5})$ so that, from (12), we find that $B = 0.234$. From (19), we find that the misadjustment due to gradient noise is then 0.0926 and, from (18), that the average time constant is $\tau_{ave} = 130$.

We now give an illustration of the adaptation time constant and determine how rapidly the system will readapt to a sudden change in jammer frequency. Figure 11 shows the values of $s(t)$ and $\hat{s}(t)$ in the region of an abrupt change in frequency from $\omega_0 = 2\pi/8T_0$ to $\omega_0 = 2\pi/12T_0$. The plot of $\hat{s}(t)$ is delayed by one sample value for clarity. The system was allowed to adapt to the first jammer for 8000 iterations so that $\hat{s}(t)$ is a good estimate of the jammer. At the 8001st iteration, we switched to the lower frequency, and we see that $\hat{s}(t)$ initially decays as the transient passes through the system. After 25 iterations it reaches its smallest amplitude; it then begins to increase in amplitude as well as adjusting its phase to the new jammer. Readaptation is nearly complete after about 130 iterations which is consistent with the calculation for the time constant.

Figure 12 shows how the notch changes its shape during the readaptation phase. Just before the frequency shift, we have a well formed notch at the initial frequency. Within five iterations of the change in frequency, we find that the notch depth is about -10 dB. The notch at the lower frequency has not yet begun to form because 5 iterations is less than one-half of a cycle of the new frequency. After 50 iterations, a notch is beginning to form at the new frequency; its depth is about the same as that at the initial frequency. After 125 iterations, a notch is reasonably well formed at the new frequency and, as the adaptation process continues, the notch depth will increase while the remnant notch at the initial frequency will continue to diminish.

The final example is that of suppressing two unequal jammers at different frequencies. In this case one jammer is at +20 dB relative to the signal and the second is at +10 dB. Figure 13 shows the two notches formed by a 48 tap, 4000 sample accumulator setup. The notch at the lower

frequency corresponds to the +10 dB jammer; we see that the notch is not as deep (≈ -20 dB) as is predicted by (13) and there is more evidence of jammer power in $|Z(\omega)|^2$ at this frequency. Examination of $z(t)$ shows that the adaptation constant ($\tau_{ave} \approx 175$) is primarily due to the strong jammer, with a secondary adaptation constant due to the weak jammer. The correlation coefficient is $\rho = 0.93$.

4. SUMMARY AND CONCLUSIONS

The purpose of the simulations was to determine the effects of using finite accumulators as dictated by the finite time-bandwidth product of the Bragg cells. The measure of performance used throughout has been the correlation coefficient between the output signal and the transmitted signal. The effect of using a finite length accumulator is to reduce the correlation coefficient by ≈ 0.5 to 1.0 dB depending on the system parameters. Some degree of taper is needed on the accumulator to reduce the effects of readaptation. The amount of taper required increases as the frequency of the jammer increases. The natural attenuation, the frequency response and the method of illumination of the Bragg cells are possible ways to implement the taper. These methods have the advantage of increasing the apparent time-bandwidth product of the Bragg cell which help to improve the overall performance of the system.

The number of taps available is probably greater than that needed in many applications. We found that increasing the number of taps improves the performance but also increases the time necessary for the system to adapt to changes in the jammer frequency or amplitude. In contrast to a conventional system where the feedback gain can be set at a low value (at the expense of slower adaptation), the gain in the optical system must not be set too high because then the system will not be stable, or set too low because then the

tap weights will not be large enough to remove the jammer energy. The notch depth is not as great as when using infinite accumulators because some of the jammer energy is needed in the residual signal to maintain the tap weights. The null is sufficient, however, to improve the signal-to-jammer ratio at the output so that a high value of the correlation coefficient is obtained.

I thank M.A. Epstein for writing the computer programs used for these simulation studies, and E.F. Smith and R.W. Boyd for their insights and suggestions. This work was supported by the U.S. Army Research office.

REFERENCES

1. R.W. Lucky, B.S.T.J., Vol. 47, 549 (1968)
2. R.W. Lucky, B.S.T.J., Vol. 44, 255 (1965)
3. D.Hirsch and W.J. Wolf, IEEE Trans. Comm. Tech.,
Vol. COM-18, 5 (1970)
4. C.W. Niessen and D.K. Willim, IEEE Trans. Comm. Tech.,
Vol. COM-18, 377 (1970)
5. A. Lender, IEEE Trans. Comm. Tech., Vol. COM-18, 625 (1970)
6. B. Widrow, J.R. Glover, Jr., J.M. McCool, J. Kauntiz,
C.S. Williams, R.H. Hearn, R.C. Goodlin, Proc. IEEE, Vol. 63,
1962 (1975)
7. L.J. Griffiths, IEEE Trans. Acous. Speech and Sig. Proc.,
Vol. ASSP-23, 207 (1975)
8. D.R. Morgan and S.E. Craig, IEEE Trans. Acoust. Speech and Sig.
Proc., Vol. ASSP-24, 494 (1976)
9. J.F. Rhodes and D.E. Brown, S.P.I.E. Symp. Real Time Sig. Proc.,
Vol. 341, 140 (1983)
10. J.F. Rhodes, Appl. Opt., Vol. 22, 282 (1983)
11. A. VanderLugt, Appl. Opt., Vol. 21, 4005 (1982)
12. A. VanderLugt, Appl. Opt., Vol. 22, 381 (1983)
13. J.R. Glover, Ph.D. Thesis, Stanford University, University
Microfilms (1975)
14. B. Widrow, J.M. McCool, M.G. Larimore, and C.R. Johnson, Jr.,
Proc. IEEE, Vol. 64, 1151 (1976)

FIGURE CAPTION LIST

- Figure 1: Discrete Transversal Filtering System with Feedback.
- Figure 2: Bragg Cell System for Producing Tap Weights.
- Figure 3: Space-Plane Representation of Tap Weights.
- Figure 4: Optical System to Produce Fourier Transform of Tap Weights.
- Figure 5: Input/Output Spectra and Filter Response.
- Figure 6: Effect of Accumulator Taper on Readaptation.
- Figure 7: Contents of Accumulator during Adaptation.
- Figure 8: Performance as a Function of Taper.
- Figure 9: Performance as a Function of Gain.
- Figure 10: Filter Response for Finite and Infinite Accumulator.
- Figure 11: Signals During Frequency Shift.
- Figure 12: System Response During Frequency Shift.
- Figure 13: Output Spectra and Filter Response for 10-dB and 20-dB Jammers.

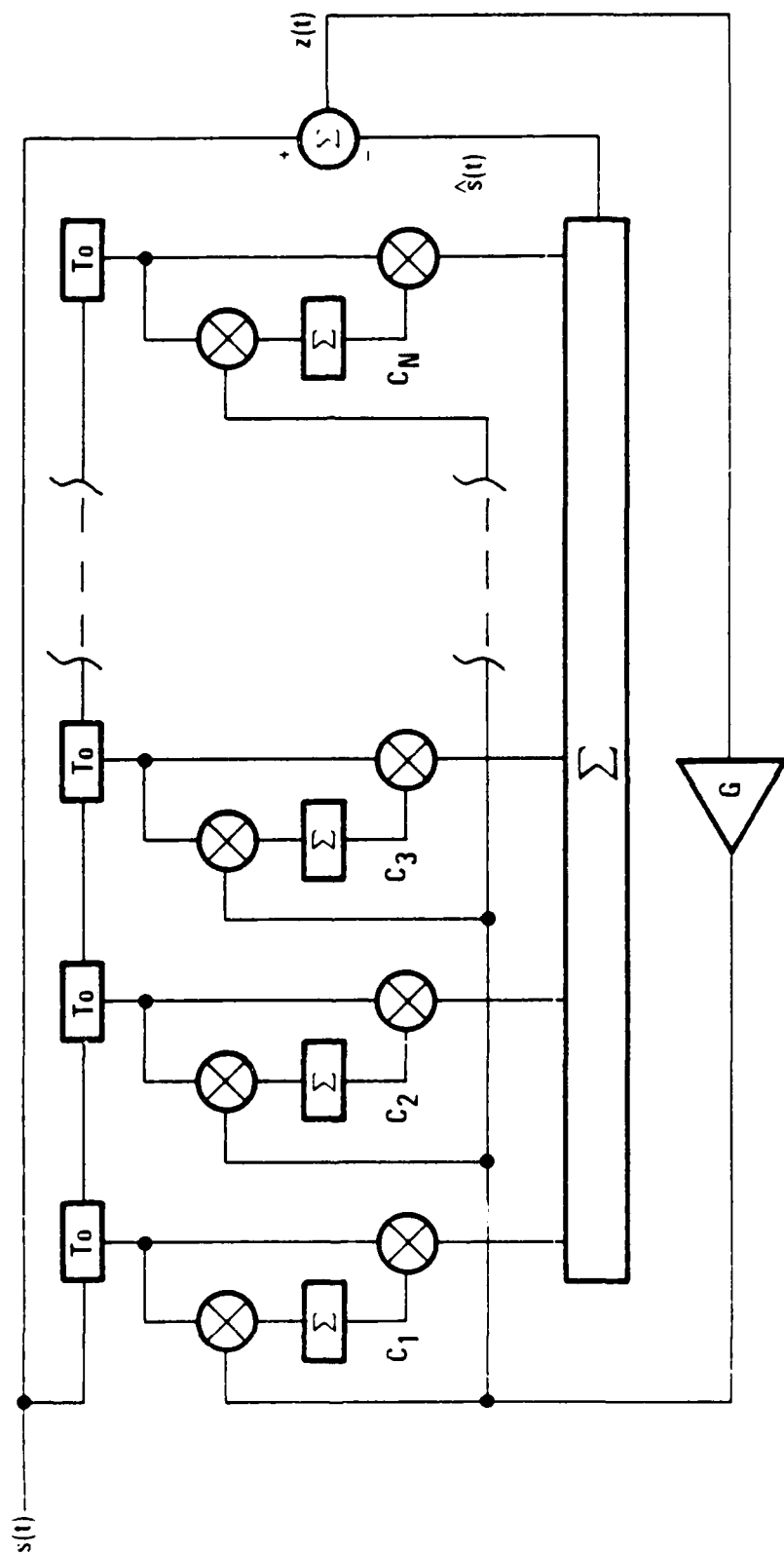


Figure 1

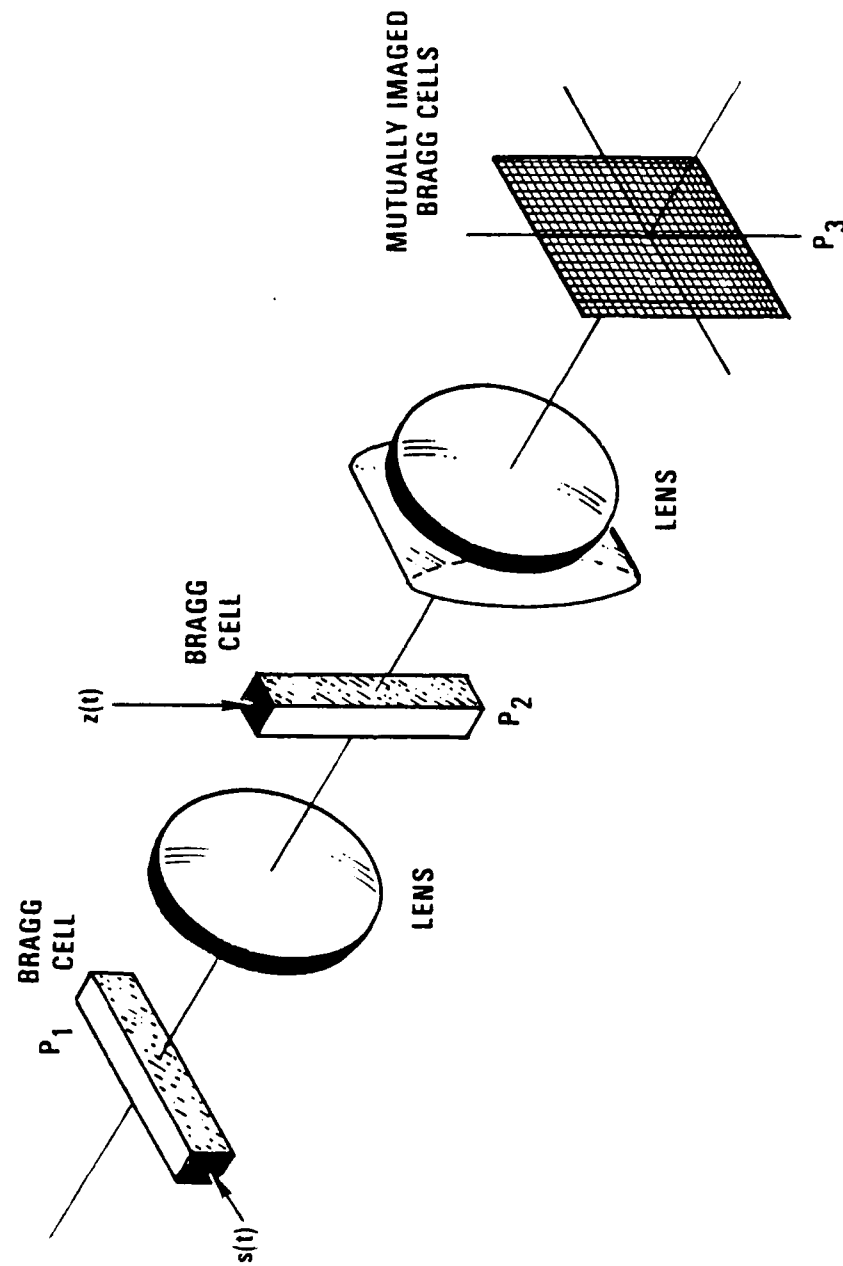


Figure 2

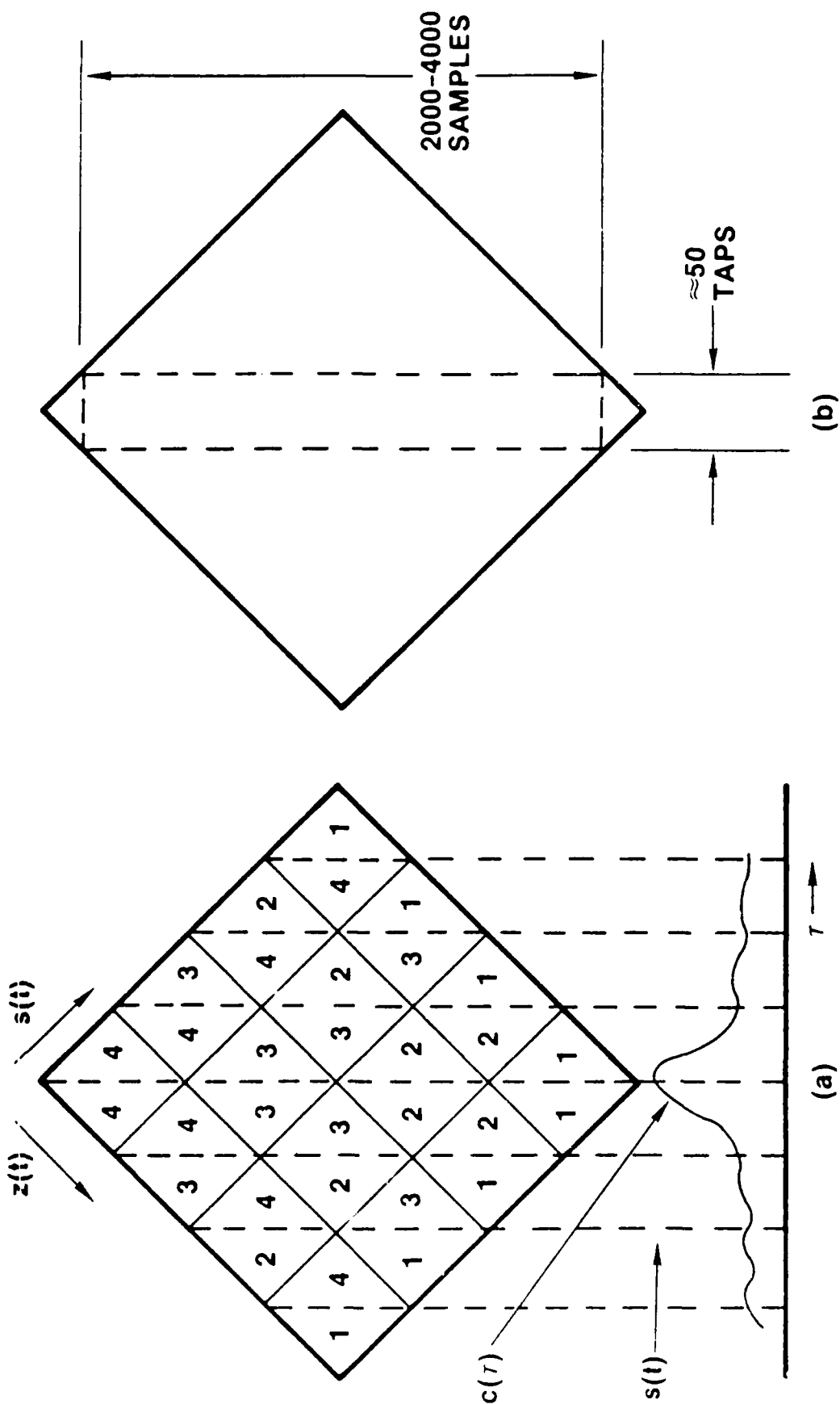


Figure 3

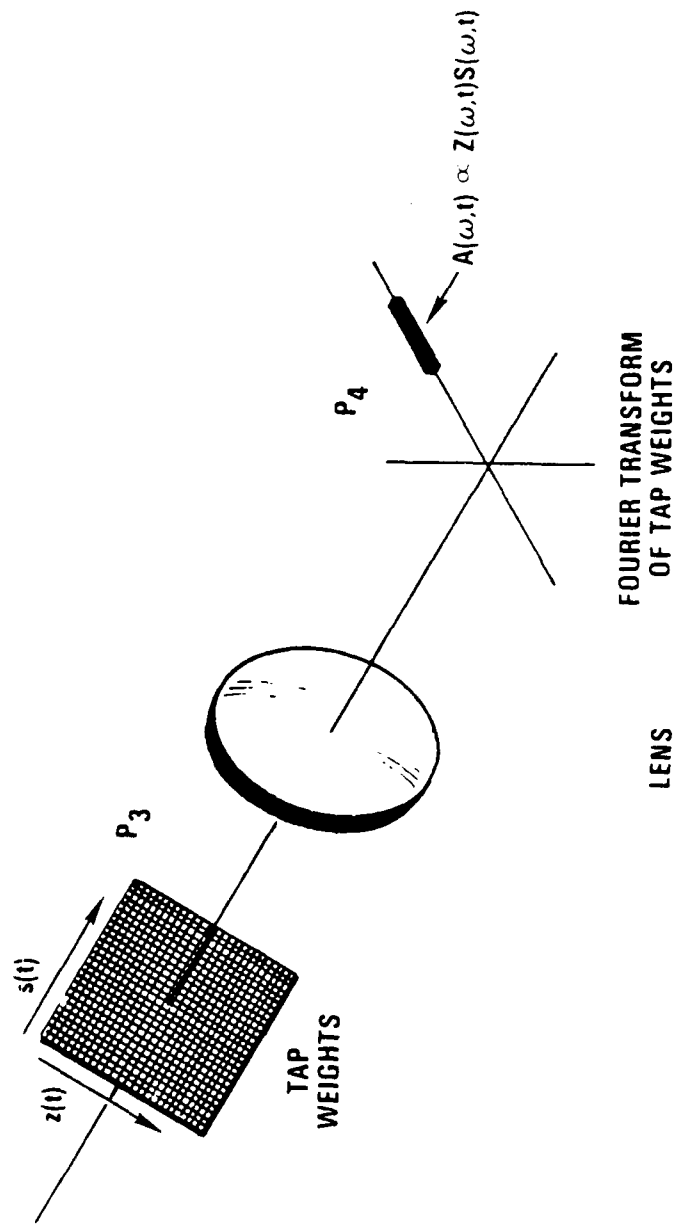


Figure 4

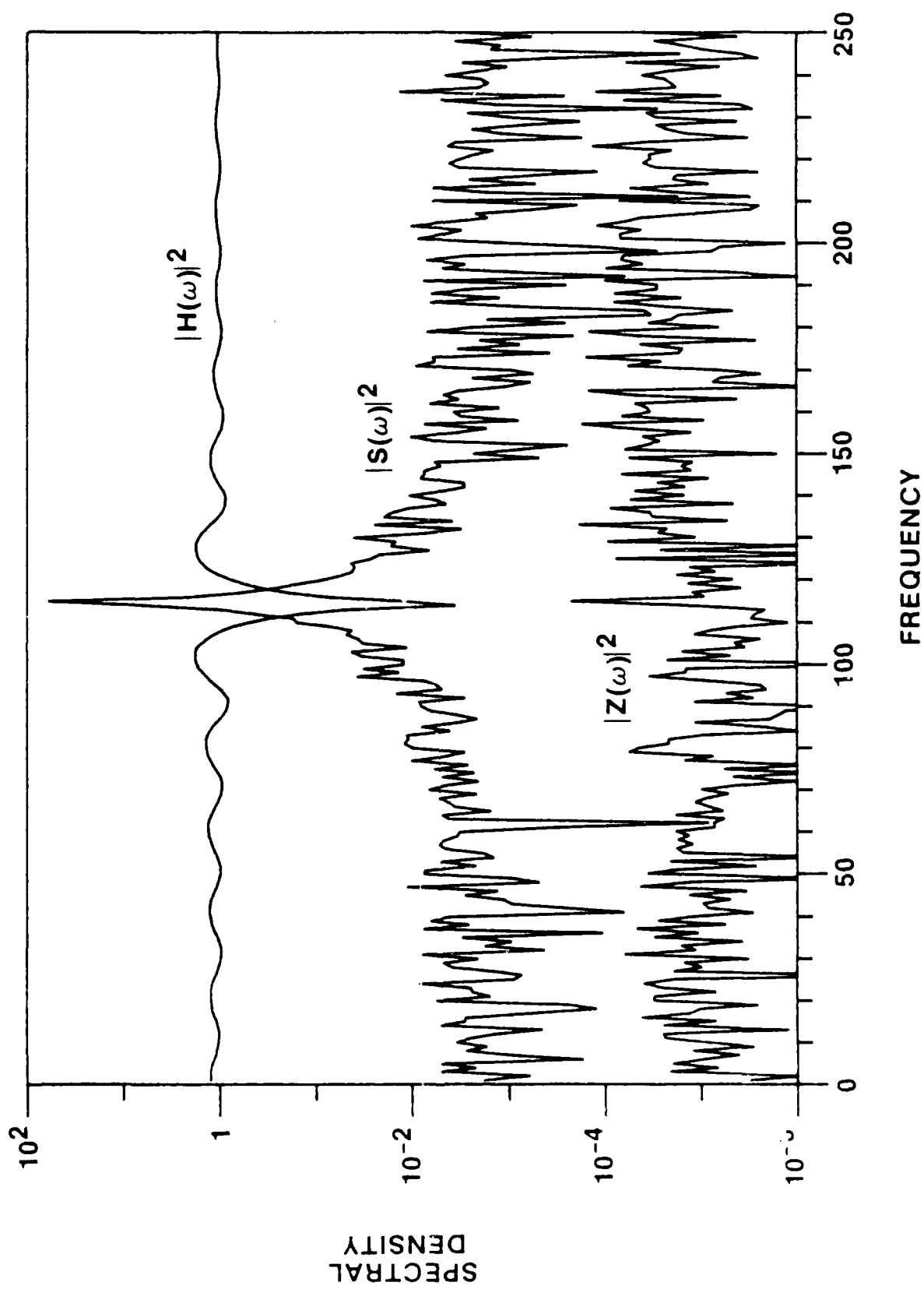
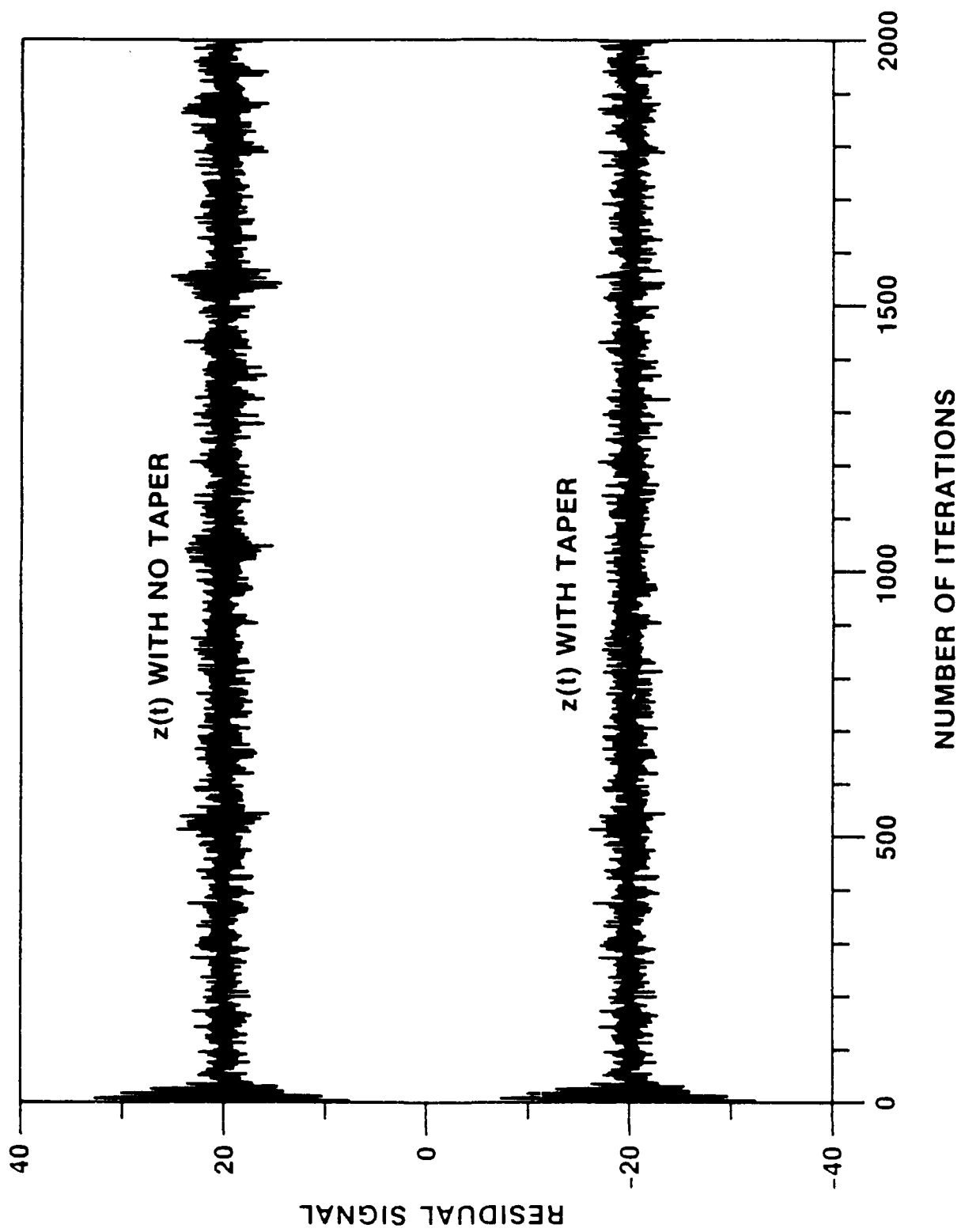


Figure 5



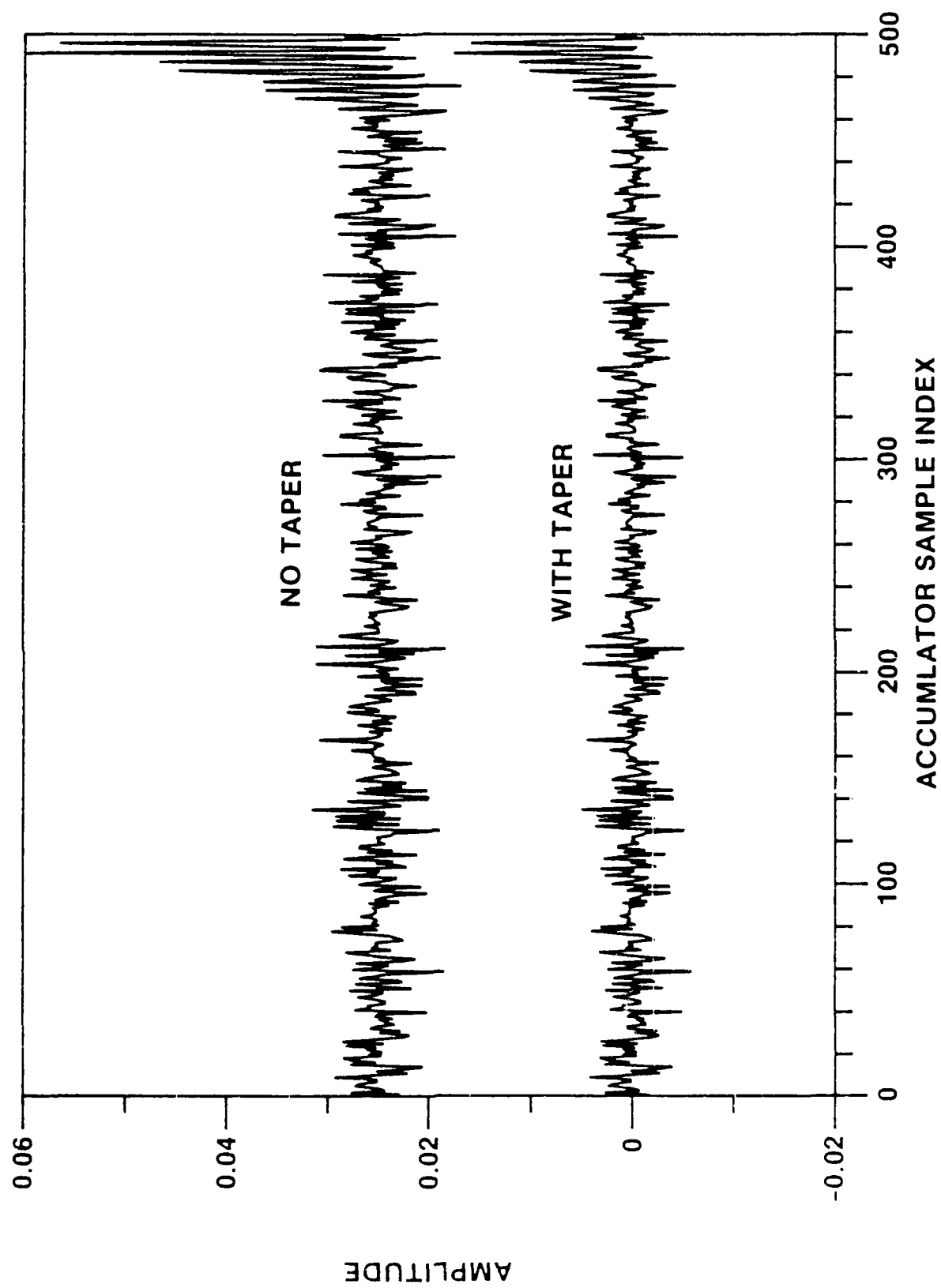


Figure 7

AD-A135 988

OPTICAL SIGNAL PROCESSING(U) HARRIS CORP MELBOURNE FL
GOVERNMENT SYSTEMS SECTOR A VANDERLUGT 30 NOV 83
ARO-17614.7-PH DAAG29-80-C-0149

2/2

UNCLASSIFIED

F/G 20/6

NL



END

FILMED

1-44

DTIC

10

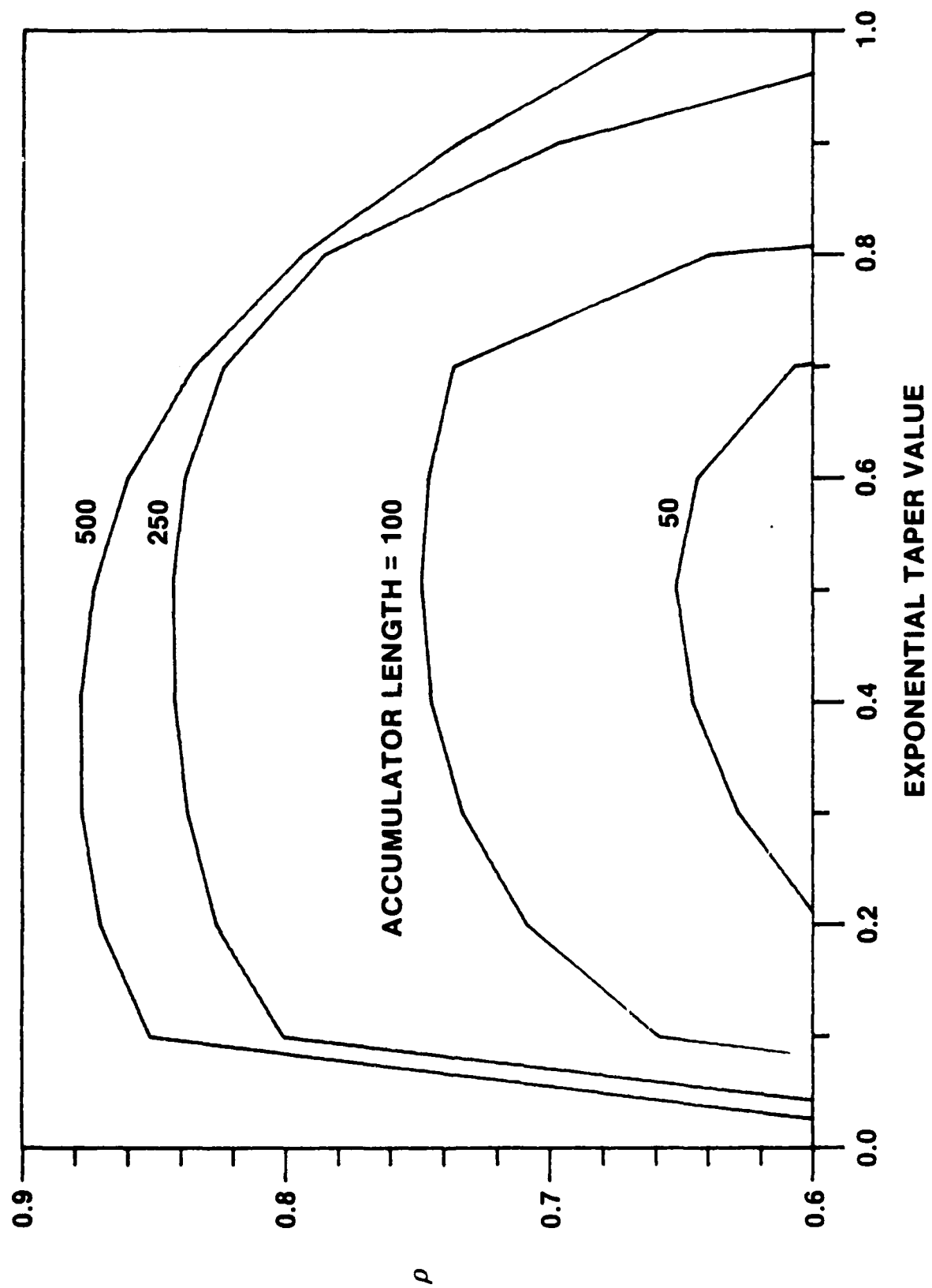


Figure 8

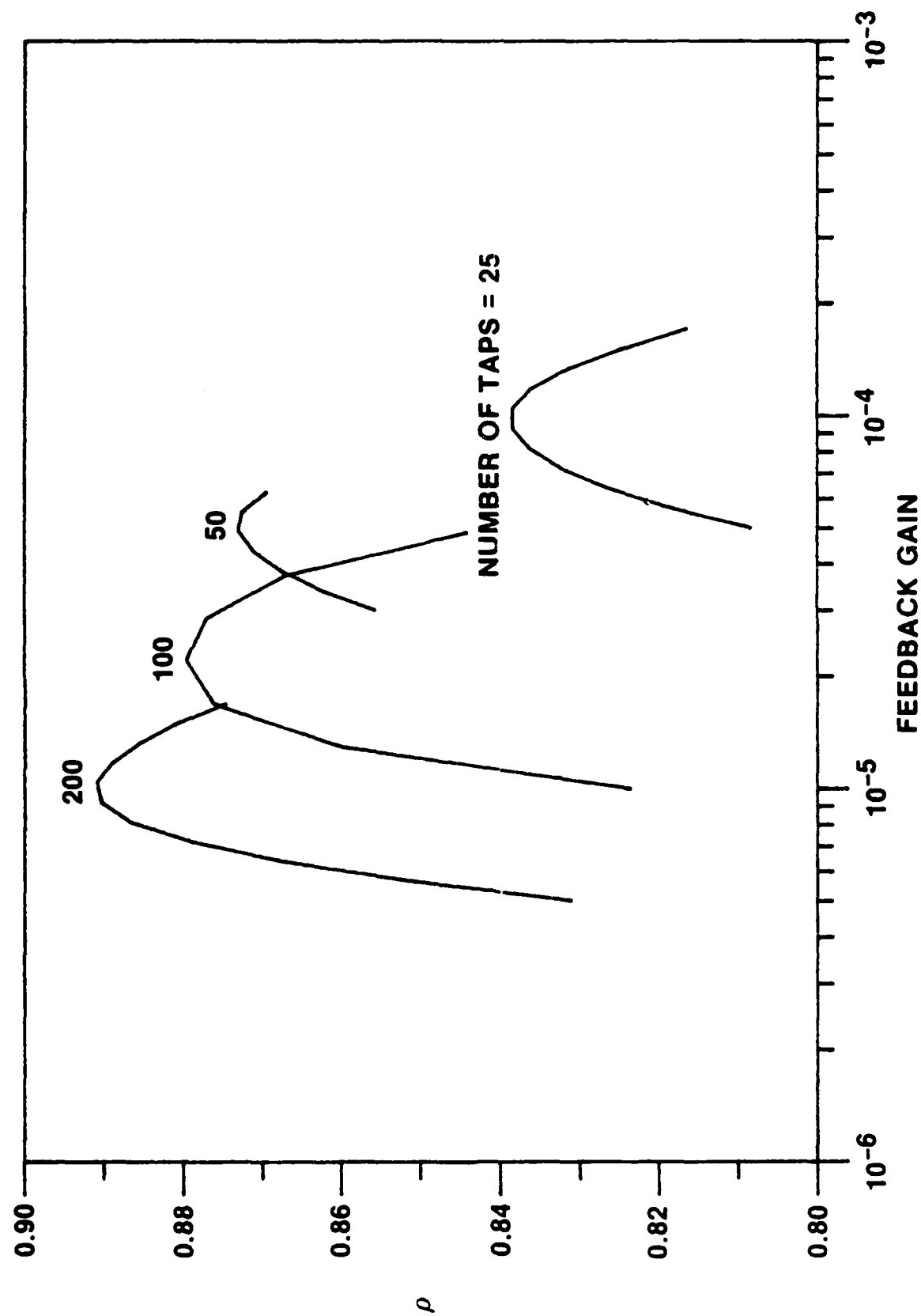


Figure 9

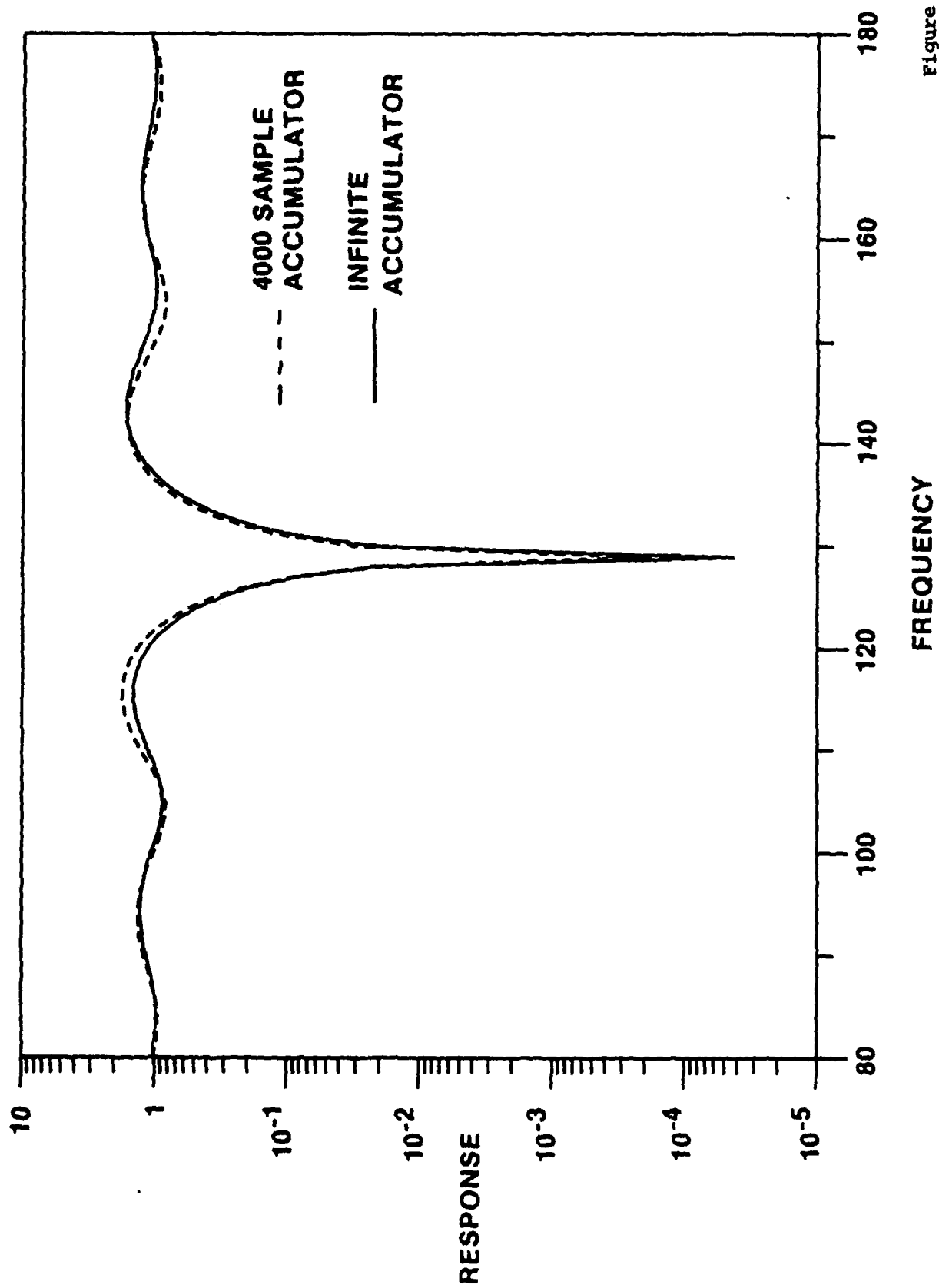


Figure 10

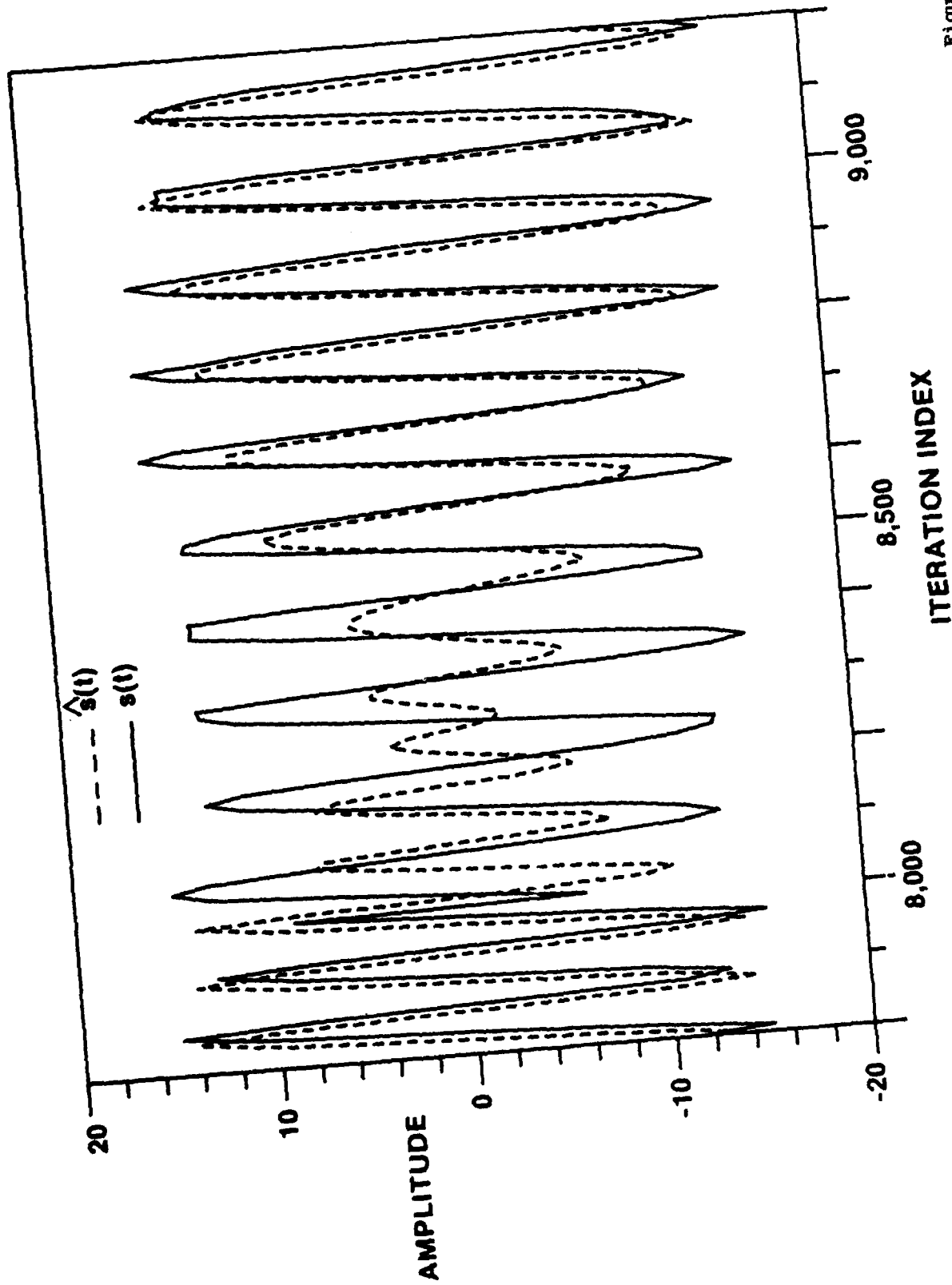


Figure 11

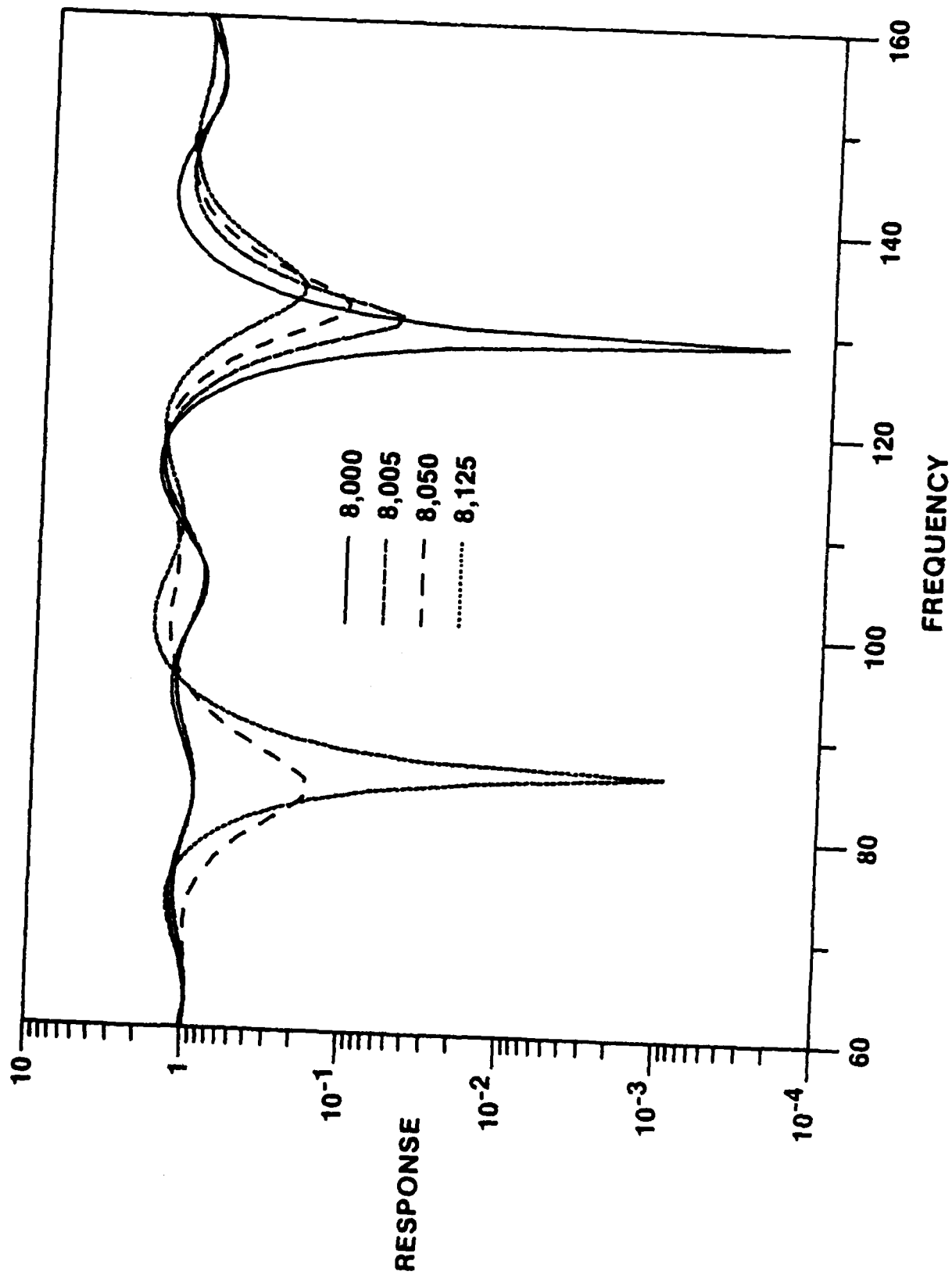
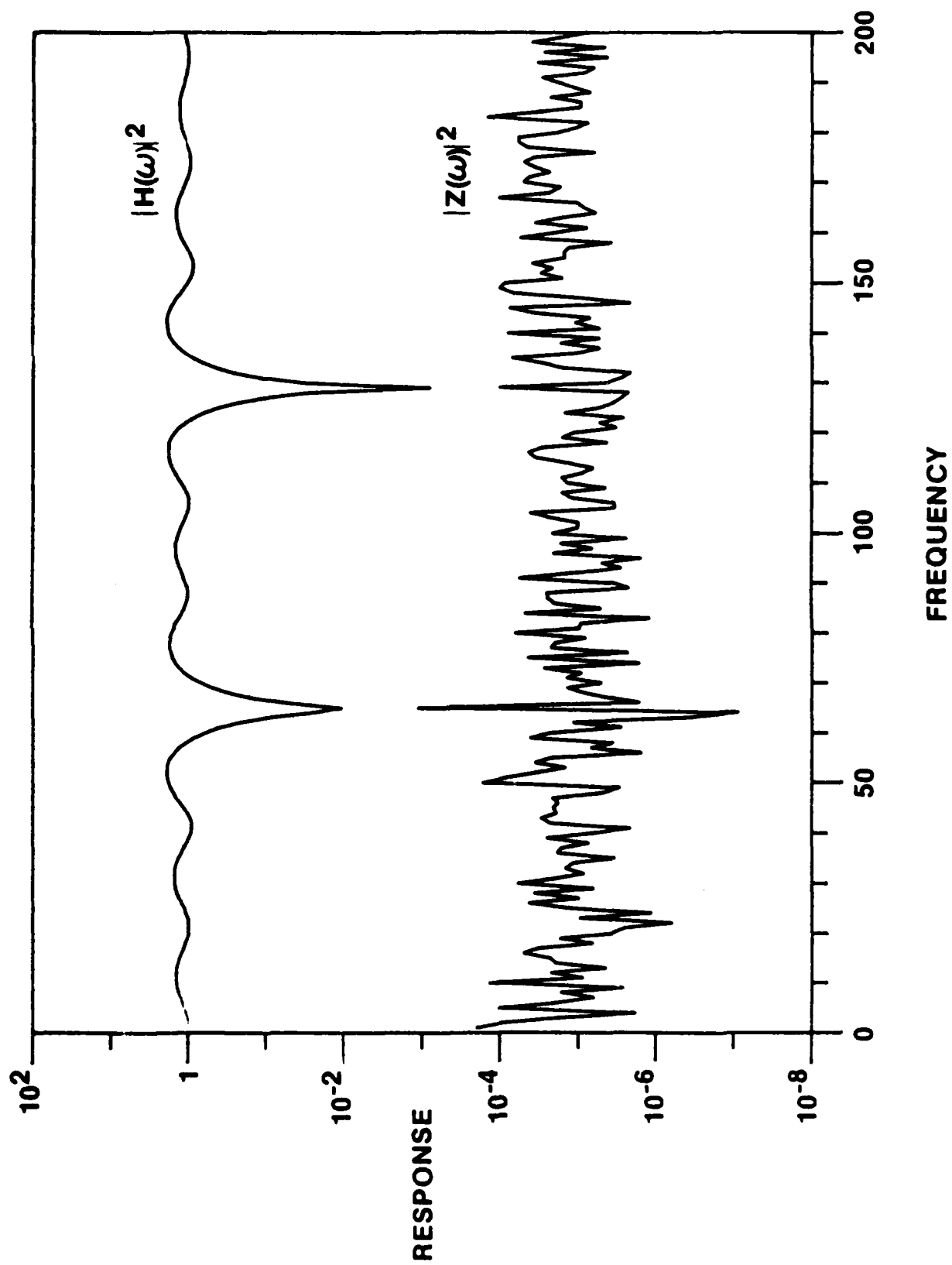


Figure 12



FILM
1-8